Numerical Simulation of Complex Wetting

Vom Fachbereich Maschinenbau
an der Technischen Universität Darmstadt
zur
Erlangung des Grades eines Doktor-Ingenieurs (Dr.-Ing.)
genehmigte

D i s s e r t a t i o n

vorgelegt von

Nicklas Wolf Linder, M. Sc.

aus Heidelberg, Deutschland

Berichterstatter:	Prof. Dr.-Ing. C. Tropea
Mitberichterstatter:	Prof. Dr.-Ing. D. Bothe
	PD. Dr.-Ing. I. Roisman
Tag der Einreichung:	20.10.2014
Tag der mündlichen Prüfung:	20.01.2015

Darmstadt 2015
D17 (Diss. Darmstadt)

Abstract

Many multiphase-flows are governed by capillarity and wettability such as spray painting and ink-jet printing applications, cooling devices of small scaled microchips and inside internal combustion engines referring to the fuel injection. The contact angle is a decisive parameter when such a system is analyzed. If the contact angle is in the bounds of the hysteresis, the contact line is pinned (immobile). An accurate numerical simulation is not trivial because of the contact line singularity, a good measure of the contact line velocity as well as the realization of pinning.

In this study, the implementation of the dynamic contact angle is extended, accounting for contact line pinning as well as the dynamic behavior in the advancing and receding phase. In short, the whole contact angle hysteresis is realized. The implementation has been validated by considering the cases of a drop impact on a horizontal surface, the simulation of drops on inclined surfaces and drops exposed to a shear flow. Moreover, the wetting of geometrically complex surfaces has been investigated and an approach for the modeling of the geometrical influence on a flat wall by a boundary condition is presented.

Kurzfassung

Viele Mehrphasenströmungen mit einer Phasengrenzfläche werden durch die Kapillarkräfte und die Benetzbarkeit beschrieben. Beispiele dafür finden sich in der Tintenstrahldruckertechnolgie, der Kühlung von kleinskaligen Bauteilen wie Mikroprozessoren und in Verbrennungskraftmaschinen beim Aufprall des Treibstoffs auf die Zylinderwände. Für die Analyse solcher Systeme ist der Kontaktwinkel ein entscheidender Parameter. Ist dieser innerhalb der Hysterese, bleibt die Kontaktlinie immobil (*gepinnt*). Wird die Hysterese überschritten, ändert sich der Kontaktwinkel dynamisch in Abhängigkeit der Kontaktliniengeschwindigkeit. Die genaue numerische Simulation solcher Fälle ist nicht trivial, da unter anderem die Kontaktliniensingularität berücksichtigt, eine gute Beschreibung der Kontaktliniengeschwindigkeit gefunden sowie der Effekt des Pinnings realisiert werden muss.

In dieser Arbeit wird die bisherige dynamische Kontaktwinkelmodellierung erweitert um zusätzlich zur dynamischen Änderung des Kontaktwinkels auch das Pinning der Kontaktlinie zu berücksichtigen. Somit ist die komplette Kontaktwinkelhysterese beschrieben. Die Implementierung wurde für verschiedene Fälle validiert: Tropfenaufprall auf horizontale trockene Oberflächen, Tropfen auf einer schiefen Ebene und Tropfen unter dem Einfluss einer Querströmung. Darüber hinaus wurde die Benetzbarkeit geometrisch komplexer Oberflächen untersucht und ein Ansatz zur Modellierung des geometrischen Einflusses allein durch eine Randbedingung auf einer glatten Wand vorgeschlagen.

Acknowledgements

I would like to express my deep gratitude to following persons who contributed in different ways to this work.

I would like to thank Professor **Cameron Tropea** for giving me the opportunity to join his Institute for Aerodynamics and Fluid Mechanics (SLA) as well as supporting me at the Graduate School of Computational Engineering. I am very happy that I have been a part of his Institute.

I am deeply grateful to Professor **Suad Jakirlić**, who helped in various concerns in the beginning of the thesis and made it possible for me to join the NUMAP-Foam Summer School in Zagreb.

I owe my deepest gratitude PD. Dr.-Ing. **Ilia Roisman** for various fruitful discussions about the specific topics of my thesis. Even more important was the personal relationship we developed over the years.

Moreover, I would like to thank Professor **Dieter Bothe** and Dr.-Ing. **Holger Marschall** for the second perspective on my work and the deep insight into OpenFOAM.

Of course I would like to thank my wife Meike, my family and friends for the support beyond the academic life. It was a pleasure to have you around me.

Last but not least, I want to acknowledge the many friends, colleagues and students for the time we spent together. Thank you Laura, Björn, Toni, Samuel, Daniel and everyone from the Dolivostraße.

This research was financially supported by the German Scientific Foundation (DFG) in the framework of the Graduate School of Computational Engineering.

Contents

Abstract i

Kurzfassung iii

Acknowledgements v

1 Introduction and Background 1
- 1.1 Motivation . . . 1
- 1.2 Nature of Surface Tension . . . 3
- 1.3 The Contact Line and Contact Angle . . . 5
- 1.4 Wenzel and Cassie-Baxter Models . . . 6
  - 1.4.1 Slip at the Contact Line . . . 7
- 1.5 Dynamic Contact Angle . . . 9
- 1.6 Hysteresis . . . 11
- 1.7 Summary . . . 15
- 1.8 Numerical Realizations . . . 15
- 1.9 Organization of the Thesis . . . 17

2 Computational Methodology 19
- 2.1 Governing Equations . . . 19
- 2.2 Description of the utilized Software . . . 20
- 2.3 Finite Volume Discretization . . . 20
  - 2.3.1 Discretization of the Solution Domain . . . 20
  - 2.3.2 Discretization of the Transport Equation . . . 22
  - 2.3.3 Temporal Discretization . . . 28
  - 2.3.4 Initial and Boundary Conditions . . . 29
  - 2.3.5 Solution Procedure . . . 30
- 2.4 Two-Phase Flow . . . 32
  - 2.4.1 Governing Equations for a Two-Phase System . . . 32
  - 2.4.2 Boundary Conditions for the Two-Phase System . . . 33
- 2.5 Summary . . . 40

3 Wetting of a Smooth Wall **43**
3.1 Droplet Wetting . . . 43
3.1.1 Numerical Setup . . . 44
3.1.2 Results . . . 45
3.1.3 Summary . . . 47
3.2 Drop on an Inclined Wall . . . 47
3.2.1 Introduction . . . 47
3.2.2 Numerical Setup . . . 49
3.2.3 Results . . . 50
3.3 Conclusion . . . 55

4 Drop exposed to shear flow **57**
4.1 Experimental Method . . . 57
4.2 Numerical Setup . . . 58
4.3 Results . . . 60
4.4 Conclusion . . . 62

5 Wetting of Complex Structures **65**
5.1 Introduction . . . 65
5.2 Experimental Studies of pyramidal structures . . . 66
5.3 Numerical Setup . . . 67
5.3.1 Hex-dominated meshes with snappyHexMesh . . . 70
5.3.2 General polyhedral mesh with gmsh and polyDualMesh . . . 72
5.3.3 Comparison of the Meshes . . . 72
5.4 Results and Discussion . . . 75
5.4.1 Rise Height and Contact Angles . . . 75
5.5 Summary for the Three Dimensional Resolved Simulations 86
5.6 Modeled Complex Surface . . . 88
5.6.1 Fictitious Contact Angle of a meniscus at a given distance to the wall . . . 88
5.6.2 Groove in a Plate . . . 90
5.6.3 Modeled Single Pyramid . . . 95
5.6.4 Modeled Array of Pyramids . . . 97
5.6.5 Comparison of the Two Dimensional Structures to the Three Dimensional . . . 98
5.7 Summary and Conclusion . . . 100

6 Conclusion **103**

A Appendix **107**
A.1 Capillary Rise for Polyhedral and Hexaedral Meshes . . . 107
A.1.1 Numerical Setup 107
A.1.2 Results for the Rise Height on a Flat Wall 109

Bibliography **111**

List of Figures **119**

List of Tables **125**

What we know is a drop, what we don't know is an ocean.
Sir Isaac Newton

Really?

1 Introduction and Background

1.1 Motivation

The ability of a fluid to be in contact with a solid substrate is known as *wetting*. Depending on the nature of the substrate and liquids as well as the surface morphology, it can attract or repel the water. The specific behavior is very important for a great variety of applications ranging from environmental system like pesticide spraying, soil erosion and dispersal of seed and microorganisms, construction engineering applications of sprinkler systems for fire suppression, cooling devices for small scaled microchips, ink-jet printing and spray painting industry up to internal combustion engines with direct fuel injections. In all these applications, the focus is on droplets impinging onto a substrate.

Additionally, a droplet on a solid substrate can be exposed to external forces like gravity or aerodynamic forces. This can be a drop on an inclined surface often observed in spray systems or drops exposed to shear flow as for example in air-dry applications. Both are also well known from everyday life thinking of a raindrop on the windshield of a car. For the industry, it is of great importance to know and understand, which conditions (e. g. an inclination angle or an inflow velocity) force a droplet to move.

A third area in this respect is forced wetting applied in coating technologies. This can either be dip-coating, where a substrate is immersed into (or drawn out of) a liquid pool or spin coating, where the solid substrate is rotating in order to spread the liquid over its surface due to centripetal effects.

In all these scenarios, the behavior of the contact line, where solid, liquid and vapor meet, is of interest. It is governed by the molecular interactions at the interface and the surface tension of the liquid. As an outcome of this interplay, a certain contact angle (the angle between the tangent of the interface at the contact line and the solid substrate) is formed. Its value depends on the liquid-solid-vapor combination and

characterizes hydrophilic substrates with a small contact angle and hydrophobic substrates with a large contact angle. The contact angle also determines the contact line velocity during the propagation. Moreover, if real substrates are considered, the roughness of a surface influences the behavior of the contact line. Peaks and gaps that cannot be observed macroscopically tend to pin a contact line. The result is already described above: the contact line remains stationary although external forces act on it known in literature as the hysteresis.

Besides the small scaled roughness of a substrate it can be geometrically complex in scales of the capillary length of the fluid. A fluid on such surfaces can experience different wetting behavior due to the geometry. This can be a rise of the contact line when dipped into a liquid pool which is higher than on flat surfaces, due to capillary effects. It can also prevent the liquid from complete wetting if the structures are very small and the liquid cannot entrain the gaps between the obstacles. Thus, the structure of the surface can influence the effective macroscopic contact angle which can be exploited to develop materials with a desired wetting behavior.

The study of the contact line dynamics is still ongoing. The physics of wetting of complex liquids or complex substrates is not completely understood. The macroscopic description of these cases lacks important phenomena on molecular scales resulting in stress singularities at the interface. Nevertheless, several models for both, the contact angle and the moving contact line, have been developed and applied in theoretical and numerical studies showing good results.

The numerical realization of the aforementioned phenomena is the focus of this thesis. The main difficulties in the correct implementation of the dynamic contact angle in a computational code are caused by

- The singularity of the stresses at the contact line which leads to the mesh-dependence of the results, if the physics are not correctly accounted for by the code,
- The dependence of the apparent contact angle on the velocity of propagation of the contact line. The estimation of this velocity, especially in a three dimensional case is not a trivial task.
- The implementation of a contact angle hysteresis requires a special treatment of the boundary condition for the flow at the solid substrate.

This study is focused thus on the development if the numerical model for

the control of the motion of the contact line. Besides the dynamic contact angle, special attention is paid on the hysteresis and the pinned contact line. Different cases of wetting are considered pointing out the abilities of the numerical simulations for flat and geometrically complex surfaces.

1.2 Nature of Surface Tension

The surface tension is a well known fundamental property of liquids we observe on a daily basis in every day life. It is the reason for the spherical shape of drops and allows water striders to *walk* on the water. It is the central property of two-phase systems with an interface.

In this chapter the physics of wetting is explained. Starting with the general phenomenon of surface tension, the focus is set on the contact line and the wetting behavior.

To introduce the surface tension and the associated contact angle the derivation of Bruus [14], based on the Gibbs free energy is followed.

The Gibbs free energy $\mathcal{G}$ of a system is the thermodynamic potential of a system with temperature T, pressure p and the particle number N. In equilibrium, this energy is per definition at a minimum. If the system consists of two sub-system with an interface, ξ shall be a general variable describing the interface (by means of position or geometrical shape etc.). Small deviations of ξ from the equilibrium state ξ_0 should lead to vanishing variation of the Gibbs free energy. Thus, the variation of the global Gibbs free energy $\delta\mathcal{G}$ for all sub-systems $\mathcal{G}_i$ is zero and can be formulated as

$$\delta\mathcal{G} = \delta_\xi \mathcal{G} \delta\xi = \left(\sum_i \delta_\xi \mathcal{G}_i \right) \delta\xi = 0. \tag{1.1}$$

The Gibbs free energy of an area for fixed pressure and temperature is the determined by the surface tension σ

$$\sigma \equiv \frac{\partial \mathcal{G}}{\partial \mathcal{A}} \tag{1.2}$$

and exists for any two different components of the system.

Consider the expansion of a curved interface as depicted in Fig. 1.1. A small area of an interface A is displaced in the direction of its normal vector by the distance δz. Thus, the radii $\mathrm{R}_{1,2}$ changed to$\mathrm{R}_{1,2}+\delta$z. The x

and y axis are oriented along the two principal curvature direction. The area after the displacement is now $\mathrm{A}+\delta\mathrm{A} = (1+\delta\mathrm{z}/\mathrm{R}_1)\,(1+\delta\mathrm{z}/\mathrm{R}_2)\,\delta x\delta y$.

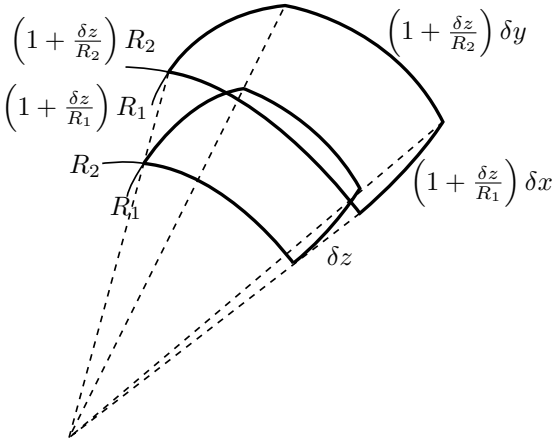

Figure 1.1: Displacement of a small area of the interface. Redrawn from [14].

Disregarding second-order terms $(\delta\mathrm{z})^2$ the change of surface area reads

$$\delta\mathrm{A} \approx \left(\frac{\delta\mathrm{z}}{\mathrm{R}_1}+\frac{\delta\mathrm{z}}{\mathrm{R}_2}\right)\mathrm{A} \tag{1.3}$$

The Gibbs free energy in the system after this infinitesimal change still needs to be zero. The expansion results in an increase of the surface energy ($\sigma\delta A$) and an increase of the volume which causes a decrease of the pressure drop over the interface to account for thermodynamic equilibrium. This can be written as

$$\delta\mathcal{G} = \sigma\delta A - (A\delta z)\,\Delta p = 0. \tag{1.4}$$

Inserting Eq. (1.3) yields to the Young-Laplace equation for the pressure drop Δp

$$\Delta p = \left(\frac{1}{\mathrm{R}_1}+\frac{1}{\mathrm{R}_2}\right)\sigma \tag{1.5}$$

where $\left(\frac{1}{\mathrm{R}_1}+\frac{1}{\mathrm{R}_2}\right)$ is the local mean curvature κ of the interface.

Thus, we can introduce several dimensionless numbers. d is a characteristic length for which the dimensionless number should be valid (e.g. a drop diameter, a channel height,..) and $\mathbf{U}$ a corresponding characteristic velocity (e.g. flow velocity, impact velocity of a drop, contact line velocity).

The Reynolds number relates the inertial effects to viscous effects and is defined as

$$\mathrm{Re} = \frac{\mathrm{d}\mathbf{U}}{\nu} \tag{1.6}$$

with the viscosity μ. The Weber number relates inertial to the surface tension forces as

$$\mathrm{We} = \frac{\rho \mathbf{U}^2 \mathrm{d}}{\sigma} \tag{1.7}$$

with the density ρ. The Capillary number describes the ratio between the viscous effects relative to the surface tension and and reads

$$\mathrm{Ca} = \frac{\mathbf{U}\mu}{\sigma}. \tag{1.8}$$

1.3 The Contact Line and Contact Angle

Considering a system where a fluid is in contact with a solid and surrounded by a gas, a *triple* or *contact line* can be defined where all three phases merge. If a drop is placed on a solid surface, this contact line is the circular edge of the drop at the wall and in the 2D-sideview (Fig. 1.2) it reduces to two points. In an equilibrium state, the tangent of the liquid interface and the solid surface enclose a *contact angle* θ_e. This contact angle can range from $0°$ for complete wetting up to $180°$ for non-wetting surfaces. Sometimes, substrates with a contact angle below $90°$ are called *hydrophilic*, and above $90°$ *hydrophobic*. This definition will be revised later, when the mobility of a drop is introduced. The term *complete* wetting is used if the surface is highly hydrophilic and the fluid spreads over the surface until a very small film remains. If the fluid does not spread infinitely and retains a macroscopic height (e. g. a water drop on a glass surface), the term *partial* wetting is applied.

At the contact line, two more surface tensions can be found: σ_{sg}, between solid and gas and σ_{sl} between solid and liquid. The surface tension between liquid and gas from before will consequently be defined as σ_{lg}. In

the equilibrium state on a perfectly horizontal surface, they are in balance resulting in Young's equation (Fig. 1.2)

$$\sigma_{sg} = \sigma_{lg} \cos\theta_e + \sigma_{sl}. \tag{1.9}$$

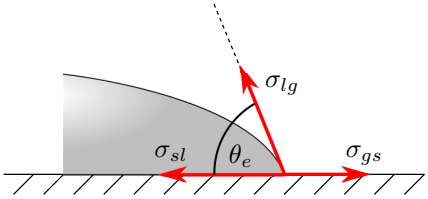

Figure 1.2: Illustration of Young's equation for the contact angle in equilibrium state.

This can also be derived from the energy balance at the equilibrium state. Assume a small displacement δl of the contact line on the solid substrate with a constant contact angle. This results in a change of the interface area near the contact line such that the area related to the solid-liquid interface increases by δl, the liquid-gas interface increases by $\delta l \cos\theta_e$ and the solid-gas interfaces decreases by δl. The change of the Gibbs free energy per unit length can thus be written as

$$\frac{1}{w}\delta\mathcal{G} = \delta l\sigma_{sl} + \delta l\sigma_{lg}\cos\theta_e - \delta l\sigma_{gs} = 0 \tag{1.10}$$

After rearranging, Eq. (1.10) is equal to Eq. (1.9).

For an equilibrium state, a uniquely defined contact angle is found. But this definition is insufficient if the surface is not ideally smooth or dynamics are involved.

1.4 Wenzel and Cassie-Baxter Models

Wenzel [99] suggested to modify Young's equation (Eq. (1.9)) to account for surface roughness. For a rough surface, the true contact area of a sessile drop differs from the projected contact area of the drop giving a measure of the surface roughness r. He thus suggested

$$\cos\theta_{\text{Wenzel}} = r\cos\theta_{\text{Young}}. \tag{1.11}$$

He based this modification on the assumption, that an increase of the contact area should affect the contact angle.

In a similar manner, Cassie [15] introduced a modified equation for the contact angle, taking heterogeneity of the substrate into account. If the substrate has two chemically different components covered by a drop with contact angles of θ_1 and θ_2 and the corresponding area fractions f_1 and f_2, he proposed

$$\cos\theta_{\text{Cassie}} = f_1 \cos\theta_1 + f_2 \cos\theta_2 \quad \text{with} \quad f_1 + f_2 = 1. \tag{1.12}$$

Finally, the Cassie-Baxter equation was formulated to describe the equilibrium state of a droplet on a chemically heterogeneous physically rough surface as

$$\cos\theta_{\text{CB}} = r f \cos\theta_e + f - 1. \tag{1.13}$$

Both models are often used and cited in several publications [38]. Nevertheless, inconsistencies have been reported [35, 59] and recently, Gao et al. [38] showed *with simple experiments that the Wenzel and Cassie equations are not directly relevant to water repellency and that events at the contact line, not over the liquid-solid interfacial area, control contact angle.* Topological changes and heterogeneity away from the contact line have no influence on the local contact line behavior. However, the morphology of the surface at the contact line has a strong influence on the local wetting behavior as discussed later. A reliable model and an accurate description is still a challenging problem.

1.4.1 Slip at the Contact Line

The movement of the contact line is not straight forward. Dussan and Davis [31] showed, that a fluid which is moving over a solid substrate is actually *rolling*. However, most mathematical an numerical descriptions of the contact line movement do not account for material points of the interface and thus neglect the rolling behavior. The lack of the physical phenomena lead to difficulties in the description of the contact line movement. Huh and Scriven [51] showed, that a moving contact line is not compatible with the application of a no-slip boundary condition at a solid wall and leads to a stress singularity at the contact line. The movement of the contact line is a result of molecular interactions and is not captured by the continuum fluid mechanics. This can be shown by assuming a small capillary number, a perfectly smooth surface (no hysteresis)

and neglecting inertial effects. We follow the lubrication approximation, meaning that the velocity profile is parabolic. The interface is moving with a constant velocity $\mathbf{U}$ along the solid substrate, or by changing the reference frame, the substrate moves with constant velocity whereas the interface is at rest.

Let z be the normal direction of the solid substrate and x the distance to the interface along the solid substrate. The velocity gradient normal to the interface at distance x is

$$\frac{\partial u_x}{\partial z} = \frac{\mathbf{U}}{h(x)} \tag{1.14}$$

and the viscous dissipation per unit volume reads

$$\epsilon \approx \eta \left(\frac{\partial u_x}{\partial z} \right)^2 \tag{1.15}$$

for a fluid with viscosity η. For small contact angles, the height $h(x)$ is approximately θx. Inserting (1.14) into (1.15) and integrating to get an estimate of the dissipation per unit time and length of the contact line:

$$\mathrm{D}_{visc} \simeq \eta \int_L^{L_{out}} \left(\frac{\mathbf{U}}{h(x)} \right)^2 h(x) dx = \eta \frac{\mathbf{U}^2}{\theta} \ln \left(L_{out}/L \right). \tag{1.16}$$

L_{out} corresponds to the outer length scales, like the radius of a drop. The typical no-slip boundary condition at the wall would assume $L = 0$ which would yield an infinite viscous dissipation. Thus, a cutoff length L is introduced to make the integral finite.

Several mechanisms have been considered to relax the singularity, such as Navier-slip models [51], mesoscopic precursor films [44], molecular films [34], surface roughness [46], shear thinning [97], evaporation and condensation [96], diffuse interface [80] and normal stress models [10, 11].

The Navier-slip model is used in the present study where the component of fluid velocity tangent to the surface (the *slip* velocity v) should be proportional to the strain rate at the surface:

$$v|_{z=0} - \mathbf{U} = \lambda \frac{\partial v}{\partial z}|_{z=0} \tag{1.17}$$

where $\mathbf{U}$ is the wall velocity, λ is the *slip length* and z the normal direction of the boundary (Fig. 1.3).

For $\lambda = 0$, the Navier-slip reduces to a no-slip condition. For $\lambda \to \infty$, we have a perfect slip without influence of the wall. The slip length is expected to be of molecular distances in the near region of the contact line [19].

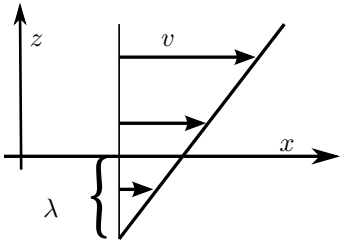

Figure 1.3: Navier-slip model with *slip length* λ

1.5 Dynamic Contact Angle

In dynamic situations, the definitions of a equilibrium contact angle do not hold anymore. In this case, the contact angle is dependent on the distance to the contact line it is measured (see Fig. 1.4) and the contact line velocity.

The existing models for dynamic contact angles can be subdivided into two main approaches depending on the framework they have been developed [9]: models are either based on the hydrodynamic theory or the molecular-kinetic theory. The former relates the equilibrium (microscopic) contact angle θ_m to a macroscopic apparent contact angle θ_d and is formulated under the consideration of viscous dissipation in the vicinity of the contact line. Cox [19] postulates three different regions, a microscopic region where short-range intermolecular forces are dominant, a macroscopic region of scales observed in the experiments and an intermediate region below the scale of observation used for general matching of the two regions (Fig. 1.4). The microscopic contact angle is either assumed to hold its static value or to be dependent on the capillary number. Such models are often expressed in a general form

$$g(\theta_d, V) - g(\theta_m, V) = Ca \ln \frac{x}{L_m} \tag{1.18}$$

where V is the ratio of viscosity in the inner and outer fluid, L_m is a

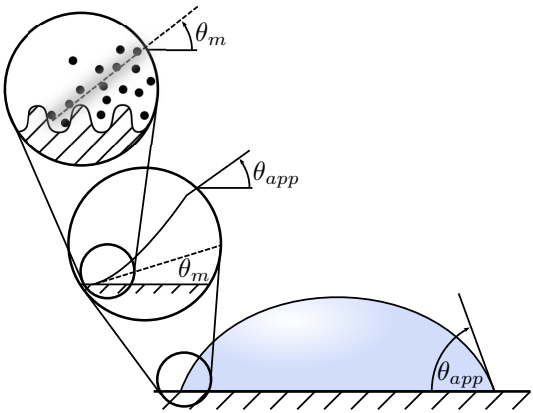

Figure 1.4: Contact angles on different scales (redrawn from [10])

microscopic length scale, and x the distance to the wall where the model is applied. If the outer fluid is treated as inviscid (the gas-viscosity is negligible small), $g(\theta, 0)$ is defined by

$$g(\theta) = \int_0^\theta \frac{x - \sin x \cos x}{2 \sin x} dx. \tag{1.19}$$

Models of this form are often referred to as Cox-Voinov laws with a common formulation for $Ca \ll 1$ given as

$$\theta_d^3 - \theta_m^3 = 9Ca \ln \frac{x}{L_m}. \tag{1.20}$$

Voinov [94] discussed the velocity-dependence of θ_m and Dussan [32] and Cox [19] revisited this model. The parameter L_m is discussed by Cox and Voinov and is typically in the range of 10 µm.

An additional model has been proposed by Shikhmurzaev [82–84], accounting for the rolling behavior of the interfaceas shortly outlined in Sec. 1.4.1.

The molecular-kinetic theory focuses on the dissipation in the immediate vicinity of the contact line governed by molecular exchange of the fluid molecules through the interface. Therein, the microscopic contact angle is velocity dependent and also the angle observed in the experiments. This theory relies only on two length scales, the molecular scales

and the macroscopic scales. In principle, "*the motion of the contact line is determined by the statistical dynamics of the molecules within a three-phase zone where the solid, liquid and gas phase meet*" [9]. In this model, the frequency of these displacements κ^0, as well as the distance between the adsorption sites λ, determine the propagation of the contact line. The resulting contact angle model based on these quantities can be written as

$$u_{cl} = 2\kappa^0 \lambda \sinh \frac{\sigma \left[\cos\theta_e - \cos\theta_d\right] \lambda^2}{2\kappa_B T}. \tag{1.21}$$

κ_B is the Boltzmann constant and T the temperature. Thus, the equation is of the form

$$u_{cl} = A \sinh \left[B \cos\theta_e - \cos\theta_d\right]. \tag{1.22}$$

Additionally, combined models have been formulated by Petrov and Petrov [70], Brochard-Wyart and de Gennes [13] and Ruijter et al. [24].

An empirical correlation is the Hoffman-Voinov-Tanner [49, 90, 94] law, which relates the dynamic contact angle to the contact line velocity at low capillary numbers $Ca \ll 1$ and is thus a simplified version of a general hydrodynamic model:

$$\theta_d^3 - \theta_e^3 = c_T Ca^{1/3} \tag{1.23}$$

with a numerical constant c_T depending on the solid-liquid-vapor combination. Several other empirical models were developed [77] and one well validated is that of Kistler [55]:

$$\theta_\mathrm{d} = f_\mathrm{H}\left(\mathrm{Ca} + f_\mathrm{H}^{-1}\left(\theta_\mathrm{e}\right)\right) \tag{1.24}$$

with the Hoffmann function

$$f_\mathrm{H} = \arccos\left\{1 - 2\tanh\left[5.16\left[\frac{x}{1+1.31x^{0.99}}\right]^{0.706}\right]\right\}. \tag{1.25}$$

For small capillary numbers it reduces to the Hofmann-Voinov-Tanner law. An extensive overview of the models can be found in [9, 10, 88]

1.6 Hysteresis

The previously defined equilibrium contact angle is based on the thermodynamic equilibrium which is correct for the equilibrium state on a

perfectly flat surface. Nevertheless, when analyzing the contact angle of a drop on a solid substrate, one will observe different angles depending on how they are measured, how they are defined, or on the history of the contact angle formation. Thus, in this section, a common basis of contact angle definitions shall be provided.

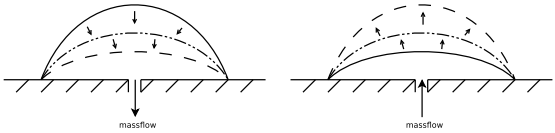

Figure 1.5: Experiment to determine the advancing and receding contact angle

Following the definitions of Cox [19] as previously described, three different regions are defined. A macroscopic region, in scales of the geometry, where we observe an apparent contact angle θ_{app}, a microscopic region, with molecular length scales microscopic or actual contact angle θ_m. In order to match the two (different) contact angles, a third intermediate region is introduced with a length scale $\propto \mathrm{Ca} \ln R$ where the interface changes sharply.

The apparent contact angle can be different for the same three components, as this angle is influenced by surface roughness, chemical contamination and solutes [23]. If a drop is placed on a solid and further mass is injected or sucked out, the drop rests at its position and compensates the change of volume by adjusting the contact angle (see Fig. 1.5). This effect can be explained by surface roughness, when considering, that the contact line has to overcome a kink as depicted in Fig. 1.6: Assuming the contact angle θ_e remains constant, the apparent contact angle measured against the macroscopic horizontal surface indicated by the dashed line changes by the amount of the angle at the kink, while the movement of the contact line over this very short distance would not be visible. Thus, the contact line would remain *immobile* and only adjust the contact angle (from a macroscopic point of view).

This phenomenon is often referred to as contact angle hysteresis. Within a band of two contact angles (the advancing contact angle θ_a and the receding contact angle θ_r) the contact line does not move and compensates any change in the volume or resists to external forces by adjusting the contact angle. If these values are exceeded, the contact angle

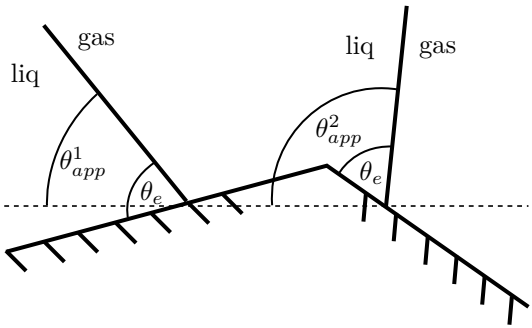

Figure 1.6: The apparent contact angle of a solid, liquid and gas system can differ due to surface roughness. The dashed line represent a macroscopic horizontal surface against which the apparent contact angles are measured. The *real* surface is not resolved.

changes dynamically as described above. All this can be summarized in a generic plot of the capillary number against the contact angle as shown in Fig. 1.7.

This hysteresis can be used to concretize the definition of hydrophobic or hydrophilic substrates. A hydrophobic substrate can be more *attractive* to water than a hydrophilic one, if the hysteresis is larger. For example, if the hysteresis of a liquid-water combination is $\theta_a = 170°$ and $\theta_r = 100°$, the critical inclination angle at which the drop would slide of a solid substrate would be larger that for a hydrophilic substrate with a hysteresis of $\theta_r = 20°$ and $\theta_a = 25°$. This is also often referred to as *mobility* of a drop.

The hysteresis effect is also well known from every day life, when we see rain drops on a window, that do not slide down, or drops an the windshield that are exposed to crossflow while driving and also remain at their position. In order to predict the wetting behavior of a liquid on a solid, the effect of the hysteresis cannot be neglected. Only in the case of high Weber numbers as they appear for drop impacts with high velocities for example, the hysteresis effects are minor.

The term *hysteresis* in literature of wetting flows is typically used to describe the relation of the immobile contact line and contact angle as described above. *Hysteresis* in general refers to a system, that does not

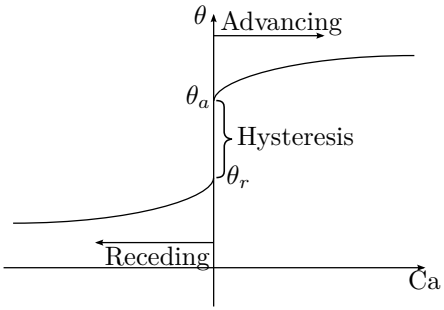

Figure 1.7: The contact angle hysteresis: The contact angle θ changes dynamically depending on the capillary number in advancing and receding phase. The hysteresis, where the contact line is immobile, is bounded by the advancing and receding contact angle θ_a and θ_r.

only dependent on the current input, but also on the history of previous inputs. This is also true for a wetting flow: Considering a drop on a solid surface, the initial radius and the initial contact angle dependent on how it has been placed on the solid substrate (e.g. impact velocity, placement technique). Thus, the output of the system for an immobile contact line and a given liquid solid combination is not unique. Considering the experiment given in Fig. 1.5, one could relate the radius of the drop to its volume as shown in Fig. 1.8. During the inflow from state 1 to 2, the contact line is pinned and the droplet does not change its radius while liquid is injected. At point 2, the advancing contact angle θ_a is exceeded and the drop expands to state 3. If now liquid is withdrawn, the volume change will first be compensated by the change of the contact angle between stage 3 and 4. If contact angle is fallen below the receding contact angle, the drop will contract continuously back to the center. Fig. 1.8 is just a sketch and for further investigation into this relation, experiments should be carried out focusing on the mentioned parameters. The area in between the 4 stages can typically be associated to an energy dissipation. If this is also true for the presented case is not known but it could be associated to viscous dissipation at the contact line. At this stage, this is just a gedankenexperiment and could be further investigated.

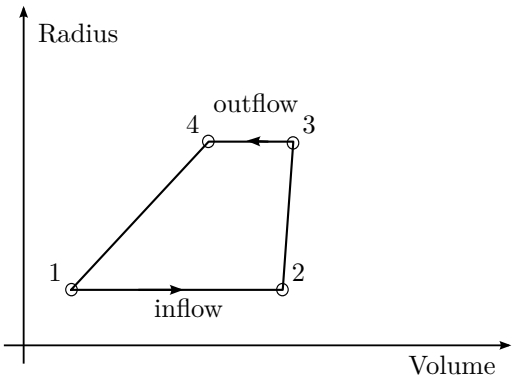

Figure 1.8: Sketch of a possible relation of the drop volume and its radius for the experiment given in Fig. 1.5 to describe the hysteresis behavior.

1.7 Summary

The description of contact line dynamics comprises three central challenges:

1. Contact line singularity
2. Dynamic contact angle
3. Hysteresis effects.

Each of the challenges has been described and the typical models introduced. In the following, the numerical realizations are presented and in Section 2.4.2 the modified numerical boundary condition applied in this study is introduced, that accounts for the listed challenges, focusing on the hysteresis effects.

1.8 Numerical Realizations

To numerically describe multiphase flows several methods have been developed over the last years. The Finite-Volume-Method (FVM) [36] and Finite-Element-Method (FEM) [5] are most commonly used. Both methods have the advantage to be applicable to complex geometries and large

problem domains compared to Molecular Dynamic (MD) simulations [2] which reveal deep insight into the physics, but are still only suitable for very small domains. Additionally, the Lattice-Boltzmann method [16] has been developed, in which the Boltzmann equations are solved instead of the Navier-Stokes equations. This method is well suited for simulations around complex geometries [17], but is limited to low Mach number flows.

In the FVM approach two main approaches have been developed to account for multiple phases: Eulerian methods such as the Volume-of-Fluid method (VOF) [45] and the Level-Set method (LS) [68], and the Arbitrary Langrangian Eulerian (ALE) methods [37]. Eulerian methods reconstruct the interface whereas ALE methods explicitly track the interface by a phase-fitting grid.

A large number of numerical studies dealing with an interface at a solid substrate can be cited, using different empirical contact angle models [77]. Examples using the VOF Method [1, 7, 74] or LS Method [86, 89] are numerous. Additionally, coupled approaches have been used to reap the benefits of both methods [100], the mass conservation of the VOF approach and the more accurate description of the interface normal and the curvature of a LS approach. Explicit methods using FEM also exhibit reasonable results. However, breakup and coalescence are not straightforward realizable [8, 37].

Several studies focus on the modeling of the hysteresis, including pinning [30, 86, 95]. Wang et al. [95] proposed a geometric formulation of the interface, where pinning is accounted for if the contact angle is within the hysteresis using the LB-Method. Spelt [86] considered a pinned interface in the the redistance step of the Level-Set function. Duquennoy et al. [30] modified the front-tracking-algorithm for the first marker at the wall to account for an imposed contact angle or contact line velocity. Dupont et al. [29] proposed a method similar to the one applied in this study and will be described later. Ding [28] considered hysteresis in a diffuse-interface method in three dimensions.

An extensive overview of recent developments and applications in different fields is given by Sui et al. [88].

The Navier-slip model (Eq. (1.17)) is often applied to deal with the contact line singularity [19, 47, 51, 86]. The slip model is *automatically* utilized in codes where face normal velocities are considered for the transportation of the phase fraction [1].

Besides the mentioned difficulties of a good estimate of the contact line velocity and a suitable contact angle model, the mesh dependency of numerical simulations of wetting flows has to be addressed. When simulating a drop impact onto a horizontal dry surface with a Cartesian grid, it can be observed, that in the receding phase the drop gets a quadratic shape aligning to the numerical grid. This can be solved by using polyhedral mesh cells with a better spatial stencil due to the increase in neighboring cells for interpolation. Additionally, a possible mesh dependency of the contact angle model to the cell size has been reported by Afkhami et al. [1].

1.9 Organization of the Thesis

The thesis so far introduced the physics of wetting and an overview of applied numerical simulations. The numerical procedure applied in the study will be described in Sec 2. Next, three wetting scenarios are investigated: Wetting of flat surfaces in Sec. 3, aerodynamic effects in Sec. 4 and wetting of complex surfaces in Sec. 5. Each of these chapters comprises an introduction into the topic, the numerical setup and presents the results.

The main subject of the present study is a numerical simulation of liquid flow governed by the propagation and pinning of a contact line. Perfect flat surfaces, as they are modeled in numerical simulations, do not account for the surface roughness of real surfaces. This shortcoming of the numerical simulations can be neglected for high Weber number flows. For low Weber number flows, the numerical contact line treatment has to be extended to account for pinning on a rough surface. A Robin-type boundary condition, i.e. a combination of the Neumann and Dirichlet boundary conditions, is introduced for the contact angle boundary condition in the present study. This gives the possibility to model the immobility of the contact line within the hysteresis using a Dirichlet boundary condition and a dynamic contact angle model for the propagating contact line using a Neumann BC. The code is applied to the estimation of the critical inclination for incipient motion of a single liquid drop on a solid substrate and the critical air inflow velocity for incipient motion of a single drop in air cross flow in a wind channel. The calculations for the critical inclination angle and air velocities corresponding to the incipient motion of a drop and are in a rather good agreement with the experimental data.

Additionally, the numerical simulation of wetting of geometrically complex structures is studied. Manukyan [61] experimentally analyzed various dip coating scenarios with pyramidal structures on the solid substrate. The thesis discusses the requirements to the computational mesh and addresses difficulties and possibilities for further examination. Moreover, an approach to model influence of the surface geometry to the propagating contact line is given. An analytic model is proposed to calculate the contact angle at a desired distance from the wall. This contact angle can be applied as a boundary condition on a flat wall. The comparison between the modeled and resolved cases are excellent.

2 Computational Methodology

This chapter introduces the computational methodology used in the present thesis. After presenting the governing equations, the numerical discretization following the Finite Volume Method (FVM) is described. Sec. 2.4 focuses on two phase systems and introduces the necessary boundary condition for the contact line.

2.1 Governing Equations

The numerical analysis is based on the continuum mechanics assumption, where the physical properties are described macroscopically as continuous quantities in space and time. The generic transport equation of the conservation law of such a physical quantity $\mathbf{\Phi}(\mathbf{x}, t)$ can be written in differential form as

$$\frac{\partial(\rho\mathbf{\Phi})}{\partial t} + \nabla\cdot(\rho\mathbf{U}\mathbf{\Phi}) = \nabla\cdot(\Gamma\nabla\mathbf{\Phi}) + S_{\mathbf{\Phi}}(\mathbf{\Phi}). \tag{2.1}$$

Therein, the first and second term represent the total rate of change of $\mathbf{\Phi}$ composed of the local temporal and the convective change due to the flux of $\mathbf{\Phi}$, respectively. They are balanced by the diffusive transport and any sources on the right hand side. Γ is the diffusion coefficient and S_ϕ represent either productive or destructive sources. As the physical quantities can be either scalars, vectors or tensors, $\mathbf{\Phi}$ is used instead of the common notation ϕ [62].

This general transport equation can be formulated as the well known governing equations of continuum mechanics as the

- conservation of mass

$$\frac{\partial\rho}{\partial t} + \nabla\cdot(\rho\mathbf{U}) = 0 \tag{2.2}$$

- and conservation of linear momentum

$$\frac{\partial\rho\mathbf{U}}{\partial t} + \nabla\cdot(\rho\mathbf{U}\mathbf{U}) - \nabla\cdot(\mu\nabla\mathbf{U}) = \rho\mathbf{g} - \nabla p. \tag{2.3}$$

In case of an incompressible fluid where $\rho = const.$, Eq. (2.2) reduces to

$$\nabla \cdot \mathbf{U} = 0. \tag{2.4}$$

Assuming additionally a Newtonian fluid and reformulating the diffusive term, the momentum equation Eq. (2.3) can be reformulated as

$$\frac{\partial \rho \mathbf{U}}{\partial t} + \nabla \cdot (\rho \mathbf{U}\mathbf{U}) = \rho \mathbf{g} - \nabla \cdot \mathbf{T} \tag{2.5}$$

with the total stress tensor $\mathbf{T}$ [62].

2.2 Description of the utilized Software

In order to numerically solve the set of partial differential equations, the OpenFOAM toolbox is used. This CFD toolbox offers a wide range of solvers to account for various different problems for example in the field of (complex) fluid flows involving chemical reactions, turbulence and heat transfer as well as solid dynamics and electromagnetics. It uses the Finite Volume numerics on unstructured meshes of polyhedral cells and is written in the programming language C++. It is available as open source, licensed under the GNU General Public License. Besides the solvers, OpenFOAM comes along with a set of utilities for pre- and postprocessing such as meshing and sampling tools.

2.3 Finite Volume Discretization

The Finite Volume Discretization is one of several discretization methods which is applied to the considered system and comprises three discretization steps: The spatial transformation of the solution domain into a discrete set of control volumes, the temporal division of time between the beginning and the end of a considered problem into discrete time-steps and the discretization of the transport equations into a set of algebraic equations. Each of these steps will be analyzed in the following.

2.3.1 Discretization of the Solution Domain

The computational mesh, which covers the whole solution domain, consists of a finite number of non-overlapping cells bounded by a finite number

of faces f. The variables of interest are computed in the cell centroids P such that

$$\int_{\mathrm{V_P}} (\mathbf{x} - \mathbf{x}_\mathrm{P})\, dV = \mathbf{0}. \tag{2.6}$$

A cell, or control volume (CV), shares each face with exactly one neighbor N (internal face), except boundary faces which coincide with the boundary of the solution domain. The *face area vector* $\mathbf{S}_f$ is normal to the face f with the magnitude of the area of the face itself. The face area vector points outwards of cells if its label is lower than the neighboring cell. A cell with a lower label is called *owner*, the other one *neighbor*. A boundary face area vector points outwards of the computational domain and is owned by the adjacent cell. This is summarized in Fig. (2.1) where the illustrated cell P owns the shaded face and therefore, the face area vector $\mathbf{S}_f$ points towards the neighboring cell N. In the remainder, all faces are called f.

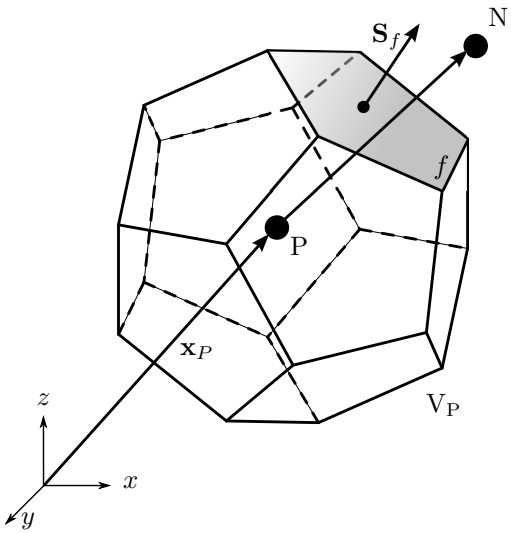

Figure 2.1: Polyhedral Control Volume

No restrictions in the amount of faces of a cell or the amount of edges of a face are given. Thus, the whole discretization technique is formulated for unstructured meshes with general polyhedrons giving freedom in the mesh creation.

2.3.2 Discretization of the Transport Equation

The general transport equation of a scalar or vector quantity $\mathbf{\Phi}$ has been introduced in Sec. 2.1 and is repeated for clarity.

$$\frac{\partial(\rho\mathbf{\Phi})}{\partial t} + \nabla\cdot(\rho\mathbf{U}\mathbf{\Phi}) = \nabla\cdot(\Gamma\nabla\mathbf{\Phi}) + S_{\mathbf{\Phi}}(\mathbf{\Phi}). \tag{2.7}$$

Eq. (2.7) is integrated over the control volume V_P around the point P and over time:

$$\begin{aligned}&\int_t^{t+\Delta t}\left[\frac{\partial}{\partial t}\int_{V_P}(\rho\mathbf{\Phi}) + \int_{V_P}\nabla\cdot(\rho\mathbf{U}\mathbf{\Phi})\right]\\ =&\int_t^{t+\Delta t}\left[\int_{V_P}\nabla\cdot(\Gamma\nabla\mathbf{\Phi}) + \int_{V_P}S_{\mathbf{\Phi}}(\mathbf{\Phi})\right].\end{aligned} \tag{2.8}$$

It is then discretized using the Finite Volume Discretization. First, the spatial derivatives of Eq. (2.8) are analyzed.

2.3.2.1 Discretization of Spatial Derivatives

In order to discretize the spatial derivatives in Eq. (2.8), Gauss' theorem is applied to transform the volume integrals into surface integrals. For a vectorial quantity $\mathbf{a}$ or a scalar quantity ϕ it states:

$$\int_V \nabla\cdot\mathbf{a}dV = \oint_{\partial V} d\mathbf{S}\cdot\mathbf{a} \tag{2.9}$$

$$\int_V \nabla\phi dV = \oint_{\partial V} d\mathbf{S}\phi \tag{2.10}$$

$$\int_V \nabla\mathbf{a}dV = \oint_{\partial V} d\mathbf{S}\mathbf{a}. \tag{2.11}$$

∂V is the bondary surface of the Volume V, $d\mathbf{S}$ is the differential of the cell-face surface normal vector.

In the follwoing, several volume and surface integral will be evaluated. Assuming linear variation in space, the variation of a function $\phi(\mathbf{x},t)$ can be written as

$$\phi(\mathbf{x}) = \phi_P + (\mathbf{x}-\mathbf{x}_P)\cdot(\nabla\phi)_P, \tag{2.12}$$

where $\phi_P = \phi(\mathbf{x}_P)$. For a volume integral, it follows

$$\begin{aligned}\int_{V_P} \phi dV &= \int_{V_P} \left[\phi_P + (\mathbf{x} - \mathbf{x}_P) \cdot (\nabla\phi)_P\right] dV \\ &= \phi_P \int_{V_P} dV + \left[\int_{V_P} (\mathbf{x} - \mathbf{x}_P)\, dV\right] \cdot (\nabla\phi)_P \\ &= \phi_P V_P \end{aligned} \tag{2.13}$$

from Eq. (2.6).

A surface integral over the boundary of a cell can be transformed into the sum over all faces, e.g.

$$\begin{aligned}\int_{V_P} \nabla \cdot \mathbf{a} dV &= \oint_{\partial V_P} d\mathbf{S} \cdot \mathbf{a} \\ &= \sum_f \left(\int_f d\mathbf{S} \cdot \mathbf{a}\right) \end{aligned} \tag{2.14}$$

The face integral of Eq. (2.14) can be expressed by

$$\int_f d\mathbf{S} \cdot \mathbf{a} = \left(\int_f d\mathbf{S}\right) \mathbf{a}_f + \left[\int_f d\mathbf{S}\,(\mathbf{x} - \mathbf{x}_f)\right] : (\nabla\mathbf{a})_f = \mathbf{S}_f \cdot \mathbf{a}_f \tag{2.15}$$

Now, Eq. (2.9) and (2.11) can be written in a discretized form as

$$\int_{V_P} \nabla \cdot \mathbf{a} dV = \int_S d\mathbf{S} \cdot \mathbf{a} = \sum_f \int_{S_f} d\mathbf{S} \cdot \mathbf{a} = \sum_f \mathbf{S}_f \cdot \mathbf{a} \tag{2.16}$$

$$\int_{V_P} \nabla\mathbf{a} dV = \int_S d\mathbf{S}\mathbf{a} = \sum_f \int_{S_f} d\mathbf{S}\mathbf{a} = \sum_f \mathbf{S}_f \mathbf{a} \tag{2.17}$$

With this methodology, Eq. (2.8) can be analyzed term by term. The convection term will be analyzed next.

2.3.2.2 Convection Term

Analyzing the convective term, it is first converted into a sum over the faces by the use of Gauss' theorem and then approximated numerically. This reads

$$\int_{V_P} \nabla\cdot(\rho\phi\mathbf{U})\, dV = \sum_f \mathbf{S}_f \cdot (\rho\phi\mathbf{U})_f \approx \sum_f \mathbf{S}_f \cdot (\rho\mathbf{U})_f \phi_f = \sum_f F\phi_f \tag{2.18}$$

where $F := \mathbf{S}_f \cdot (\rho \mathbf{U})_f$ denotes the face mass flux.

It is obviously necessary to calculate face averaged quantities (ϕ_f), which are approximated by the cell centered values from two neighboring cells.

Differencing Schemes The differencing scheme is used to obtain approximated face centered values of a given variable. Its choice depends on the restrictions each scheme poses. Especially for bounded variables, it is on the one hand important to guarantee its boundedness, on the other hand, numerical diffusion should be avoided. Moreover, stability and robustness of the scheme has to be considered. An extensive overview of possible schemes are given in [53]. Here, a brief overview of the popular schemes is given.

Central Differencing Scheme (CDS) The CDS interpolates linearly between the cell-centroids of two neihboring cells P and N. It is second-order accurate in space, but does not guarantee boundedness. The interpolated face-centered value ϕ_f is obtained by

$$\phi_f = \mathbf{f}_x \phi_P + (1 - \mathbf{f}_x)\, \phi_N. \tag{2.19}$$

$\mathbf{f}_x$ gives the distance between the face-center and the cell-centers by linear interpolation as

$$\mathbf{f}_x \equiv \frac{|\mathbf{x}_f - \mathbf{x}_N|}{|\mathbf{d}|} = \frac{\overline{fN}}{\overline{PN}}. \tag{2.20}$$

Upwind Differencing Schmes (UDS) The UDS extracts the face-centered value from the cell value in *upwind* direction. That means, if the flux through a face of cell P points outwards, the value of ϕ_P is chosen. If it points inwards, the cell value of the neighboring cell ϕ_N is chosen. The scheme is first-order accurate in space and guarantees boundedness of the solution. The drawback is the introduction of numerical diffusion. It is formulated as

$$\phi_f = \max(F, 0)\, \phi_P + \min(F, 0)\, \phi_N. \tag{2.21}$$

Combined UD and CD schemes In order to benefit from the advantages of the methods and to reduce the disadvantages, the upwind and differencing schemes can be combined to preserve boundedness with acceptable

accuracy. In general, the methods are combined as

$$\phi_f = \psi \phi_{f,CD} + (1 - \psi)\, \phi_{f,UD} \tag{2.22}$$

with the blending factor ψ which can vary between 1 and 0. If $\psi = 1$, a pure CDS is obtained whereas $\psi = 0$ gives a pure UDS. The choice of ψ can be based on the *Normalised Variable Diagram* (NVD) of Leonard [58] and be set equally for all faces of the domain or individually face-by-face. For the NVD, normalized variables are introduced as

$$\widetilde{\phi_P} = \frac{\phi_P - \phi_U}{\phi_D - \phi_U} \quad \text{and} \quad \widetilde{\phi_f} = \frac{\phi_f - \phi_U}{\phi_D - \phi_U} \tag{2.23}$$

The subscripts U and D are illustrated in Fig. 2.2. As unphysical oscil-

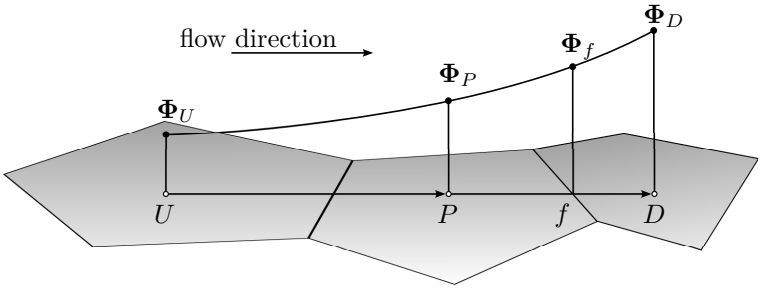

Figure 2.2: Combined UD and CD schemes

lations are to be avoided, ϕ_P needs to be bounded by its neighbors ϕ_U and ϕ_D ($\phi_U \leq \phi_P \leq \phi_D$ or $\phi_U \geq \phi_P \geq \phi_D$). Expressed in the normalized variable $\widetilde{\phi_P}$, known as the *convective boundedness criterion* (CBC) by Gaskell and Lau [39] it reads:

$$0 \leq \widetilde{\phi_P} \leq 1. \tag{2.24}$$

For unstructured meshes with general polyhedrons $\widetilde{\phi_P}$ has to be modified as

$$\widetilde{\phi_P} = 1 - \frac{(\nabla\phi)_f \cdot \mathbf{d}}{(2\nabla\phi)_P \cdot \mathbf{d}} \tag{2.25}$$

with P being the upwind cell to face $\mathbf{f}$ and $\mathbf{d} = \mathbf{x}_D - \mathbf{x}_P$ [53].

The NVD diagram is used to illustrate the region where boundedness is guaranteed [53]. It illustrates $\widetilde{\phi_f}$ as a function of $\widetilde{\phi_P}$.

2.3.2.3 Diffusion Term

The diffusion term is discretized analogously to the convective term, applying Gauss' theorem:

$$\int_{V_P} \nabla \cdot (\rho \Gamma_\phi \nabla \phi)\, dV = \sum_f \mathbf{S}_f \cdot (\rho \Gamma_\phi \nabla \phi)_f \approx \sum_f (\rho \Gamma_\phi)_f\, \mathbf{S}_f \cdot (\nabla \phi)_f \quad (2.26)$$

$(\Gamma_\phi)_f$ can be interpolated assuming linear variation as outlined before (Eq. 2.12). In two-phase flows, Patankar [69] and Kothe [56] suggested to take the interface / cell-face orientation into account as it represents the viscosity in the momentum equation and therefore may differ in the two phases:

$$(\Gamma_\phi)_f = \eta_f\, (\Gamma_\phi)_f^p + (1 - \eta_f)\, (\Gamma_\phi)_f^s\,, \quad (2.27)$$

where p and s denote the parallel (harmonic) and the serial (geometric) average, respectively. η_f is a weighting factor defined as

$$\eta_f \equiv \left| \left(\frac{(\nabla \alpha)_f}{\left| (\nabla \alpha)_f \right|} \right) \cdot \frac{\mathbf{S}_f}{|\mathbf{S}_f|} \right| \quad (2.28)$$

to account for the harmonic or geometric contribution according to the orientation of the interface to the the cell-face. If the interface normal is parallel to the face-area vector, η_f approaches unity, for the two vectors being perpendicular η_f is zero and η_f varies smoothly in between the two extremes.

Next, the face normal gradient $\mathbf{S}_f \cdot (\nabla \phi)_f$ is analyzed. If $\mathbf{S}_f \parallel \mathbf{d}$, the mesh is called *orthogonal* where the face normal gradient can be expressed as

$$\mathbf{S}_f \cdot (\nabla \phi)_f = |\mathbf{S}_f|\, \frac{\phi_N - \phi_P}{|\mathbf{d}|}. \quad (2.29)$$

In this form, the computation of the face normal gradient is expressed by only two cell-centered variables. Alternatively, it can be obtained from the cell centered gradients of the two cells which then can be interpolated to the shared face and multiplied by the face area vector:

$$\mathbf{S}_f \cdot (\nabla \phi)_f = \mathbf{S}_f \cdot [\mathbf{f}_x\, (\nabla \phi)_P + (1 - \mathbf{f}_x)\, (\nabla \phi)_N] \quad (2.30)$$

$$\text{and} \quad (\nabla \phi)_P = \frac{1}{V_P} \sum_f \mathbf{S}_f \phi_f.$$

If $\mathbf{S}_f \nparallel \mathbf{d}$, the mesh is *non-orthogonal* and Eq. (2.29) is not valid. The computation is therefore split into two parts:

$$\mathbf{S}_f \cdot (\nabla\phi)_f = \underbrace{\boldsymbol{\Delta} \cdot (\nabla\phi)_f}_{\text{orthogonal contribution}} + \underbrace{\mathbf{k} \cdot (\nabla\phi)_f}_{\text{non-orthogonal correction}} \tag{2.31}$$

using the compact expression Eq. (2.29) for the orthogonal contribution ($\boldsymbol{\Delta} \parallel \mathbf{d}$) and correct it by Eq. (2.30) which also valid for non-orthogonal cases. Eq. (2.31) introduces two new vectors, $\boldsymbol{\Delta}$ and $\mathbf{k}$ (Fig. 2.3) which have to satisfy

$$\mathbf{S}_f = \boldsymbol{\Delta} + \mathbf{k}. \tag{2.32}$$

Several possible decompositions are given in [53].

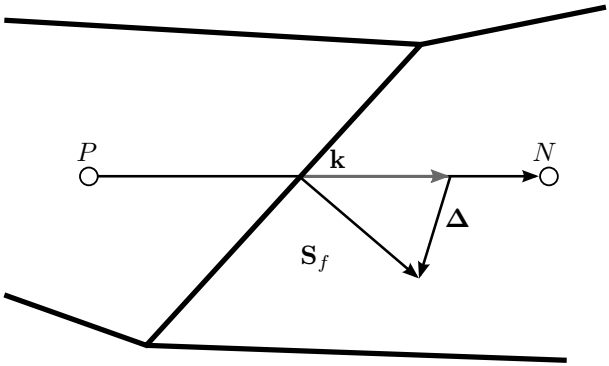

Figure 2.3: Correction of the non-orthogonal contribution

2.3.2.4 Source Terms

Source terms $S_\phi(\phi)$ comprise all terms that are not formulated as convective, diffusive or temporal quantities. It can be a general function of ϕ which is linearized and integrated over the cell volume:

$$\int_{V_P} S_\phi(\phi)\, dV \approx S_{\phi_1} V_P + S_{\phi_2} \phi_P V_P, \tag{2.33}$$

where S_{ϕ_1} and S_{ϕ_2} can be a function of ϕ and

$$S_{\phi_2} = \frac{\partial S_\phi(\phi)}{\partial \phi}. \tag{2.34}$$

It is advisable to treat source terms as implicit as possible [53].

2.3.3 Temporal Discretization

Besides the spatial discretization, the integration over time of the terms in Eq. (2.8) has to be discretized. In this study the Euler implicit time differencing scheme is applied which is first-order accurate in time, guarantees boundedness and is unconditionally stable. The time derivative of the volume integral reads

$$\frac{\partial}{\partial t}\int_{V_P}(\rho\phi)\,dV \approx \frac{(\rho_P\phi_P V_P)_{(t+\Delta t)} - (\rho_P\phi_P V_P)_t}{\Delta t}. \tag{2.35}$$

If for the set of terms in Eq. (2.8) linear variation in time is assumed the terms are discretized as

$$\int_t^{t+\Delta t}\left[\frac{\partial}{\partial t}\int_{V_P}(\rho\phi)\,dV\right]\mathrm{d}t \approx (\rho_P\phi_P V_P)_{(t+\Delta t)} - (\rho_P\phi_P V_P)_t\,, \tag{2.36}$$

$$\int_t^{t+\Delta t}\left[\int_{V_P}\mathcal{L}\phi dV\right]\mathrm{d}t \approx \mathcal{L}^\star\left(\phi_P\right)_{(t+\Delta t)}\Delta t, \tag{2.37}$$

$$\int_t^{t+\Delta t}\left[\int_{V_P}S_\phi\left(\phi\right)dV\right]\mathrm{d}t \approx \left(S_{\phi_1}V_P + S_{\phi_2}\phi_P V_P\right)_{(t+\Delta t)}\Delta t, \tag{2.38}$$

where the convective and diffusive terms are summarized the symbolic differential operator $\mathcal{L}$ and $\mathcal{L}^\star$ being the discretized form of it.

Adaptive timestepping Although stated above, that the Euler implicit scheme is unconditionally stable, due to the segregated solution of pressure and velocity, the Curant number should be limited at least by 1. Thus, the size of the time step is decisive for both, to obtain stable and correct solutions and to keep the computational time reasonable. In transient calculations with high velocities, the time step needs to be small to not violate the Courant number limit. In (nearly) stationary problems, the time step can be large to reduce the computational effort. An adaptive time step control is therefore beneficial, to get the largest possible time step without violating the Courant number limit by prescribing

$$\Delta t = \min\left\{\min\left[\min\left(\frac{\mathrm{Co}_{max}}{\mathrm{Co}_0}\Delta t_0, \left(1+\lambda_1\frac{\mathrm{Co}_{max}}{\mathrm{Co}_0}\right)\Delta t_0\right), \lambda_2\Delta t_0\right], \Delta t_{max}\right\}, \tag{2.39}$$

where the Courant number is defines as

$$\mathrm{Co} = \frac{|\mathbf{U}_f \cdot \mathbf{S}_f|}{\mathbf{d} \cdot \mathbf{S}_f} \Delta t. \tag{2.40}$$

λ_1 and λ_2 are damping factors to avoid oscillations of the time step. [6] states that $\mathrm{Co}_{max} \approx 0.2$ is an upper limit to obtain reasonable results, although for several preliminary studies it was chosen up to $\mathrm{Co}_{max} \approx 0.7$ without significant influence of the results.

2.3.4 Initial and Boundary Conditions

To numerically represent a given physical scenario, the variables of consideration have to be initialized. In case of a drop impact for example, one typically does not simulate the whole apparatus with the detachment of the drop from a needle and its acceleration. Instead, only the area close to the surface is respected. The cells inside the drop are set to the measured impact velocity. This is the same for the phase indicator function, which will be introduced later and indicate the distribution of the considered phases. Thus, the initial conditions provide the set up at which the calculation will start.

Moreover, boundary conditions are necessary for faces that coincide with the boundary and have no neighboring cells for the calculation of face values. The two basic boundary conditions are Dirichlet and Neumann boundary conditions which prescribe a fixed value ϕ_b or a gradient $(\mathbf{S}_f / |\mathbf{S}_f|) \cdot (\nabla\phi)_b$ at the boundary face, respectively. From these basic boundary conditions different derived boundary conditions can be formulated to account for a certain physical behavior.

Typically, at an impermeable wall, the no-slip condition holds, which means, that the velocity vector at the boundary face is set to the wall velocity. A stationary wall would therefore be represented by a zero-vector. An impermeable wall also requires the gradient of the pressure to be zero, such that there is no flux through the wall. The special treatment of the boundary condition at a wall for the phase fraction in a two fluid formulation will be provided in Sec. 2.4.2.

Open boundaries can be accounted for, if either the velocity is prescribed and the pressure gradient is set to zero (inlet), or the other way round, such that the pressure distribution is prescribed and the gradient of the velocity is zero (outlet). They can also be combined to a single

boundary condition that *switches* between both, depending on the direction of the volumetric flux (into or out of the cell).

To account for a symmetry in the calculation, the pressure gradient needs to be zero to make sure no flux goes through that face as it would be compensated be the symmetric counterpart coming from the symmetry. The velocity of the face is equal to that of the cell center, also resulting in a zero-gradient.

An axisymmetric case can be simplified by calculating a slice of the spherical domain. The mesh is one cell thick, whereas the edges at the axis of the first cell collapse resulting in a cell with six vertices. The opening angle of the slice should be less than 5°. To account for the axisymmetry, the vectorial quantities are rotated between the front and back patches preserving their magnitude. Scalar quantities are directly transferred.

2.3.5 Solution Procedure

The present study deals with Newtonian and incompressible fluids. In this case, no explicit equation for pressure is available. Therefore, de-coupling of velocity and pressure must be avoided. The semi-discretized momentum equation is used to derive a discretized pressure equation from the continuity restriction of the divergence-free velocity field. The *Pressure Implicit with Splitting operators* algorithm by Issa [52] is used. The algorithm will be briefly outlined and for further details, the reader is referred to [52, 53, 75].

2.3.5.1 PISO-Algorithm

The PISO-Algorithm comprises three basic steps:

- **Predictor Step**: The latest available pressure field is used in the solution of the implicit momentum equation giving an intermediate velocity field. In general, this field will not satisfy the zero-divergence condition.
- **Pressure Solution**: Using the intermediate velocity field, a new pressure field is calculated.
- **Explicit Velocity Correction**: With the new pressure field, the velocity field is updated to be consistent with the pressure field

The last two steps have to be repeated as the updates of the velocity fields in the neighborhood influences the solution (not only the pressure equation).

2.3.5.2 Solution of the Linear Algebraic Equations

After discretization, for each cell a set of linear algebraic equations have to be solved. Although each of the equations is different, they can be written in a general form as

$$a_P \phi_{P(t+\delta t)} + \sum_N a_N \phi_{N(t+\delta t)} = b. \tag{2.41}$$

In matrix notation it reads

$$\mathbf{A} \cdot \mathbf{\Phi} = \mathbf{b}, \tag{2.42}$$

where $\mathbf{A}$ is a sparse matrix representing the connection of the cells in the mesh. The diagonal of the matrix comprises the coefficient a_P and the off-diagonals the neighbor-coefficient a_N. $\mathbf{\Phi}$ is the vector of the unknowns ϕ and $\mathbf{b}$ comprises the source terms.

If Eq. (2.42) is multiplied by $\mathbf{A}^{-1}$, $\mathbf{\Phi}$ can be obtained. Inverting $\mathbf{A}$ is typically not possible in a direct manner, as $\mathbf{A}$ is sparse.

Therefore, an iterative solver to obtain an approximate solution of $\mathbf{\Phi}$ is applied. Starting with an initial guess, the solution is iteratively improved until a prescribed difference between two consecutive solutions is reached. Additionally, the matrix can be preconditioned to have a better convergence rate. Such techniques can be the multiplication with a suitable preconditioning matrix. The present study applies the Preconditioned Conjugate Gradient (PCG) solver for symmetric matrices and the Preconditioned Bi-Conjugate Gradient (PBiCG) method with a Diagonal-based Incomplete Lower-Upper (DILU) preconditioner. This solver is suitable to problems up to 100 000 unknowns as reported by Damián [21]. Beyond, the Gauss-Seidel smoother with a Geometric-Algebraic Multi-Grid (GAMG) is used. Details about these methods can be found in [76].

In two-phase flows as it will be introduced in the next chapter, an additional equation for the phase fraction field has to be solved. For this variable, it is important to preserve boundedness. The Multidimensional Universal Limiter of Explicit Solution (MULES) is used to solve the equation. In the analogy to flux corrected transport, the fluxes obtained using

a higher-order, limited scheme and a first order-upwind scheme are used to calculate an antidiffusive flux by their difference. This flux is then limited by the extrema determined by the neighboring cells. A very detailed description is given by Damian [21].

2.4 Two-Phase Flow

Up to now, the focus was an the general description of the finite volume method for a general transport equation. The present thesis deals with the computation of two-phase system, thus, the governing equations and additional boundary treatment will be presented next.

2.4.1 Governing Equations for a Two-Phase System

To account for two incompressible and immiscible fluids in the framework of the VOF-Method [45] an additional variable, the *volumetric phase fraction* α_φ is introduced. It denotes, how much volume is occupied by phase φ in a given volume: If it values one, it is completely covered by phase φ, if it is zero, no phase φ is present and values in between indicate the interface of the two phases.

The governing equations then consist of the continuity equation and momentum equation and additionally the transport equation for the phase indicator in conservative form

$$\nabla \cdot (\mathbf{U}) = 0, \tag{2.43}$$

$$\frac{\partial}{\partial t}(\rho_\varphi \mathbf{U}) + \nabla \cdot (\rho_\varphi \mathbf{U}\mathbf{U}) = -\nabla p + \nabla \cdot \boldsymbol{\tau} + \rho_\varphi \mathbf{g} + \mathbf{f}_\sigma, \tag{2.44}$$

$$\frac{\partial \alpha_\varphi}{\partial t} + \nabla \cdot (\alpha_\varphi \mathbf{U}) = 0, \tag{2.45}$$

for each phase, respectively. Therein, ρ is the density, $\mathbf{U}$ the velocity field, p the pressure, τ the stress tensor, $\mathbf{g}$ the gravity, $\mathbf{f}_\sigma$ the body force per unit mass representing the surface tension effects at the interface between two phases. Since we consider a two-phase situation, we will denote the phase fraction simply by α, dropping the subscript φ.

The viscous stress tensor τ is given as

$$\boldsymbol{\tau} = \mu \left[\nabla \mathbf{U} + (\nabla \mathbf{U})^T \right] - \frac{2}{3} \mu \mathbf{I} (\nabla \cdot \mathbf{U}), \tag{2.46}$$

with the identity tensor $\mathbf{I} \equiv \delta_{ij}$. For incompressible, Newtonian fluids, the divergence of the stress tensor reduces to $\nabla \cdot \boldsymbol{\tau} = \nabla \cdot \left[\mu \left(\nabla \mathbf{U} + (\nabla \mathbf{U})^T\right)\right]$ which can be rearranged for discretization as

$$\nabla \cdot \boldsymbol{\tau} = \nabla \cdot (\mu \nabla \mathbf{U}) + (\nabla \mathbf{U}) \cdot \nabla \mu. \tag{2.47}$$

The two fluids are treated as one effective fluid throughout the computational domain, discriminated by the value of the phase fraction. Thus, the corresponding fluid properties (density and viscosity μ) are calculated as weighted averages based on the volume fraction:

$$\rho = \rho_{\mathrm{l}} \alpha + (1 - \alpha)\, \rho_{\mathrm{g}} \tag{2.48}$$

$$\mu = \mu_{\mathrm{l}} \alpha + (1 - \alpha)\, \mu_{\mathrm{g}}, \tag{2.49}$$

where the subscripts l and g denote the belonging to the liquid and gas respectively.

Typically, if the VOF-method is applied, some technique is used to *compress* the interface and counteract the inevitable numerical diffusion. Most of them combine upwind and downwind schemes such as the CICSAM [93] or HRIC [67]. The present solver applies an additional compression term in the transport equation, that preserves boundedness and compresses the interface based on the concept of "counter-gradient" [7, 26, 98].

The surface tension can be written as

$$\mathbf{f}_\sigma = -\sigma \kappa \mathbf{n}_\Sigma \tag{2.50}$$

with the (constant) surface tension coefficient σ, the cell averaged curvature over the interface κ and the interface normal vector $\mathbf{n}_\Sigma$. σ and $\mathbf{n}_\Sigma$ are only in weak form defined as the volumetric gradient and divergence are not defined. The Continuum Suface Force (CSF) model [12] is used to model the surface force $\mathbf{f}_\sigma$ as a body force $\mathbf{f}_\sigma^b$. The phase indicator is spread over several cells and the surface tension force can be reformulated as

$$\mathbf{f}_\sigma^b = -\sigma \nabla \cdot (-\mathbf{n}_{\mathrm{I}})\, \nabla \alpha = -\sigma \nabla \cdot \left(\frac{\nabla \alpha}{\|\nabla \alpha\|}\right) \nabla \alpha. \tag{2.51}$$

$\mathbf{n}_{\mathrm{I}}$ is the averaged normal vector of the interface.

2.4.2 Boundary Conditions for the Two-Phase System

The numerical realization of a (dynamic) contact angle model is shown next. The idea is to rotate the gradient of the phase fraction at the

boundary to align the interface to a given contact angle by the boundary condition. Using a Neumann BC, the inner product of the outward pointing unit normal vector and the gradient of a variable ϕ (e.g. α) at a boundary face

$$\mathbf{n}_\mathrm{b} \cdot \nabla (\alpha)_\mathrm{b} = g_b \tag{2.52}$$

is prescribed.

As shown in Eq. (2.51), the gradient of the phase fraction has to be calculated to evaluate the surface tension term in a cell. In the discretized form, the gradient is evaluated as a weighted sum of the values of the phase fraction at the faces. At a boundary, the face-values are prescribed as boundary condition. To fulfill a given contact angle θ at the wall, the normal vector of the interface $\mathbf{n}_\mathrm{I}$ can be prescribed relative to the normal of the boundary $\mathbf{n}_\mathrm{b}$ as

$$\mathbf{n}_\mathrm{I} \cdot \mathbf{n}_\mathrm{b} = \cos\theta. \tag{2.53}$$

As $\mathbf{n}_\mathrm{I}$ can be expressed by gradients of α (Eq. (2.51)), the influence of a given contact angle is respected in the calculation of the surface tension term, if $g_\mathrm{b} = \cos\theta$ in Eq. (2.52).

As shortly outlined in Sec. 1.8, no special modifications to allow movement of the phase fraction is necessary as the advection of the phase fraction uses the face centred, non-zero velocities half a cell above the wall. However, the influence of the mesh-size cannot be neglected in dynamic situations. The contact angle boundary condition needs to take the mesh-size into account [1].

In dynamic situations, the contact angle depends on the contact line velocity. Therefore, the boundary value g_b is calculated for each time step, dependent on the contact line velocity (the calculation of the contact line velocity is provided in Chap. 2.4.2.1). Thus, depending on the contact line velocity, and the given contact angle model, the dynamic contact angle for the advancing and receding phase can be employed. The specific choice of the contact angle model did not show a significant influence on the results as also reported by [77].

A dynamic contact angle model alone is not enough to account for pinning due to hysteresis. A contact line can only be immobile if the value of the phase fraction at the boundary face does not change in time. A Neumann BC does not fix the value at the boundary face, only its gradient. Therefore, within the hysteresis, a Dirichlet boundary condition has to be satisfied, which directly provides the value of the phase fraction

at the boundary.

The main idea used in this study is the use of a Neumann BC for the dynamic situation of a moving contact line and a Dirichlet BC for the static case. The combination of both boundary conditions is known as a Robin BC which combines a Neumann and Dirichlet BC for the boundary value of a quantity ϕ_b as

$$\phi_\mathrm{b} = \beta \cdot \phi_\mathrm{b} + (1-\beta)\left(\phi_\mathrm{P} + \nabla\phi_\mathrm{b} \cdot \mathbf{d}_b\right), \tag{2.54}$$

where β is a local switching factor between the two boundary conditions.

To decide which boundary condition should be applied, the current contact angle θ_cur is extracted (Eq. (2.53)) and compared to the given values of the hysteresis. If θ_cur is within the hysteresis (between the receding and advancing static contact angles), a Dirichlet condition is applied with the same value of the phase fraction as in the current timestep – the contact line is fixed. If θ_cur is beyond the hysteresis, the capillary number and the corresponding contact angle is calculated from a contact angle model. Additionally, the current cell is identified as part of the advancing or receding front of the contact line to ensure that pinning is not mistakenly applied. Therefore, the direction of cell centered velocity $\mathbf{u}_\mathrm{P}$ is compared to the gradient of the phase fraction

$$\mathbf{u}_\mathrm{P} \cdot \mathbf{n}_\mathrm{I} > 0 \quad \rightarrow \quad \text{advancing front} \tag{2.55}$$

$$\mathbf{u}_\mathrm{P} \cdot \mathbf{n}_\mathrm{I} < 0 \quad \rightarrow \quad \text{receding front.} \tag{2.56}$$

The whole algorithm is summarized in **Algorithm 1**.

Dupont et al. [29] presented a similar method for their code JADIM. Therein, the momentum balance equations are discretized on a staggered orthogonal grid using the finite volume method, accounting for two phases using the Volume-of-Fluid approach. The imposition of a given contact angle is realized by use of an additional layer of ghost cells at the interface. The value of the ghost cell is determined by the information from the first and second cell above the wall as well as the gradient of the ghost value normal to the wall.

Their solution procedure consists of four steps: first, they update the phase fraction by solving the advection equation. Second, they perform a semi-implicit viscous solve for an intermediate velocity field $\mathbf{U}^\star$. In the third step, they calculate the capillary contribution for a second interme-

Algorithm 1 Apply Robin BC to phase fraction

```
for all Boundary Cells do
    Calculate the current contact angle from Eq. (2.53)
    Calculate local Capillary number from Eq. (1.8) and Eq. (2.66)
    if θ_R < θ_cur < θ_A then
        β ← 1 (Dirichlet BC)
        α at the boundary face is kept constant
    else if θ_cur < θ_R  and  u_P · n_I > 0 then
        β ← 0 (Neumann BC)
        Dynamic contact angle model is applied.
    else if θ_cur > θ_A  and  u_P · n_I < 0 then
        β ← 0 (Neumann BC)
        Dynamic contact angle model is applied.
    end if
end for
```

diate velocity field $\mathbf{U}^{\star\star}$ by

$$\frac{\mathbf{U}^{\star\star} - \mathbf{U}^{\star}}{\Delta t} = \frac{1}{\rho^{n+1/2}} \mathbf{F}_v^{n+1/2} \tag{2.57}$$

where $\mathbf{F}_v^{n+1/2}$ is the surface tension force. The fourth step is a projection step for the new velocity field $\mathbf{U}^{n+1}$. They account for pinning in the hysteresis by *calculating the angle $\theta^{\star}$ that cancels the local momentum balance Eq. (2.57) in the cells in contact with the wall and cut by the interface*. If this angle is within the hysteresis, the contact angle for the new time step is set as $\theta^{\star}$. Thus, the local momentum balance equations are solved and the interface is immobile. If $\theta^{\star}$ is beyond the hysteresis the new contact angle is calculated by a contact angle model and the new capillary contribution is calculated from Eq. (2.57).

In our opinion, the method of estimation of the contact angle based on the momentum balance should not lead to any increase of the precision in calculations since, as a shortcoming of the sharp interface model, the stresses near the contact line associated to its motion or change of the contact angle are singular and cannot be accurately predicted with the available models. This is why the singular region is "cut-off" from the computational domain and the contact angle is replaced by its modeled dynamic value.

This method showed very good results for the cases of two-dimensional

drops on an inclined wall and two-dimensional drops subjected to a shear flow. They state that their method can be extended to three-dimensional configurations, but no such computations have been found in literature. As the method is described for structured, orthogonal meshes, it is limited to geometries that can be meshed under this restriction.

The advantage of our method is that it is based on unstructured meshes of general topology and thus applicable to complex geometries. Moreover, we show its applicability to three-dimensional cases as well.

2.4.2.1 Contact Line Velocity

One of the most important issues in the numerical simulations of the flows which are influenced by wettability and involve moving contact angle is associated to the shortcoming of the model in handling the singularity. This manifests itself in mesh-dependent results of numerical calculations of such problems. One of the reasons of this mesh dependence is in the variation of the apparent contact angle with the distance from the contact angle [1, 29] and the second is in the difficulties to accurately predict the propagation velocity u_{cl} of the contact line, which is then used in the modeling of the apparent dynamic contact angle, using existing empirical or semi-empirical models ((1.20), (1.22)-(1.24)).

a) Conventional Approach A common approach to estimate the contact line velocity u_{cl} from the calculations is to take an interface normal component of a material point velocity $\mathbf{u}_P$ in the vicinity of the contact line and take its wall parallel projection [29]:

$$u_{\mathrm{cl}} = \frac{\mathbf{n}_{\mathrm{I}} - (\mathbf{n}_{\mathrm{b}} \cdot \mathbf{n}_{\mathrm{I}})\mathbf{n}_{\mathrm{b}}}{|\mathbf{n}_{\mathrm{I}} - (\mathbf{n}_{\mathrm{b}} \cdot \mathbf{n}_{\mathrm{I}})\mathbf{n}_{\mathrm{b}}|} \cdot \mathbf{u}_{\mathrm{P}}, \tag{2.58}$$

where $\mathbf{n}_{\mathrm{I}}$ is the normal vector of the interface and $\mathbf{n}_{\mathrm{b}}$ the normal vector of the boundary as illustrated in Fig. 2.4. $\mathbf{u}_{\mathrm{P}}$ is the cell centred velocity of the cell where the propagation velocity is calculated.

The main problem with this formulation is that it is in fact not physical since the velocity of the contact line propagation is not equal to a material point velocity. Section 2.4.2.1 b) illustrates this issue.

Let us consider for simplicity a creeping flow in a two-dimensional corner near the contact line, propagating with the velocity u_{cl}. The two-dimensional creeping velocity field in a corner has been analyzed in [66]

for various boundary conditions. The velocity field $\mathbf{u}$ is determined using a stream function ψ in the form

$$\mathbf{u} = u_{\mathrm{cl}} \left[\frac{1}{r} \frac{\partial \psi}{\partial \phi} \mathbf{e}_r - \frac{\partial \psi}{\partial r} \mathbf{e}_\phi - \cos(\phi + \theta) \mathbf{e}_r + \sin(\phi + \theta) \mathbf{e}_\phi \right], \tag{2.59}$$

where $\{r, \phi\}$ is a polar coordinate system with the base vectors $\{\mathbf{e}_r, \mathbf{e}_\phi\}$, fixed at the corner vertex.

A particular solution for the stream function ψ of the velocity field in the corner bounded by a moving wall and a straight free surface associated with the moving contact line problem [20] is

$$\psi = r \, \frac{\phi \cos\phi \sin\theta - \theta \cos\theta \sin\phi}{\sin\theta \cos\theta - \theta}. \tag{2.60}$$

It satisfies the Stokes equation, $\nabla^4 \psi = 0$, and the boundary conditions at the wall ($\phi = -\theta$) and the free surface ($\phi = 0$):

$$\phi = -\theta : \qquad \frac{\partial \psi}{\partial \phi} = r, \quad \frac{\partial \psi}{\partial r} = 0, \tag{2.61}$$

$$\phi = 0 : \qquad \frac{\partial \psi}{\partial r} = 0, \quad \frac{\partial^2 \psi}{\partial \phi^2} = 0. \tag{2.62}$$

In this coordinate system, the unit normal to the substrate and the unit normal to the liquid interface vectors $\mathbf{n}_b$ and $\mathbf{n}_I$, respectively, are expressed as

$$\mathbf{n}_{\mathrm{I}} = \mathbf{e}_\phi, \quad \mathbf{n}_{\mathrm{b}} = \sin(\phi + \theta) \mathbf{e}_r + \cos(\phi + \theta) \mathbf{e}_\phi. \tag{2.63}$$

Let us apply Eq. (2.58) to the velocity at the liquid interface, using $\phi = 0$ and Eq. (2.60) in Eq. (2.59). We obtain

$$u_{\mathrm{cl,\ calculated}} = u_{\mathrm{cl}} \frac{\theta \sin^2 \theta}{\theta - \cos\theta \sin\theta}. \tag{2.64}$$

The dependence of the expression $u_{\mathrm{cl,\ calculated}}/u_{\mathrm{cl}}$, predicted by Eq. (2.64) on the apparent contact angle is shown in Fig. 2.5. The contact line velocity predicted using Eq. (2.58) agrees well with the physical value only near $\theta \approx \pi/2$ where $u_{\mathrm{cl,\ calculated}}/u_{\mathrm{cl}} \approx 1$, since Eq. (2.58) does not account for the radial velocity in the corner generated by the motion of the contact line.

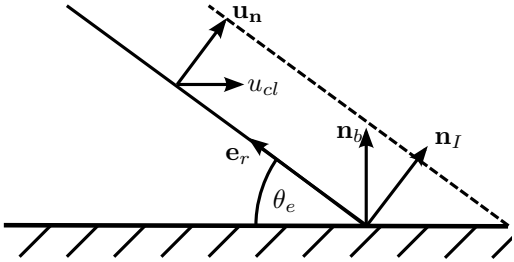

Figure 2.4: Sketch of the velocity vectors at the liquid interface and the propagation velocity of the contact line.

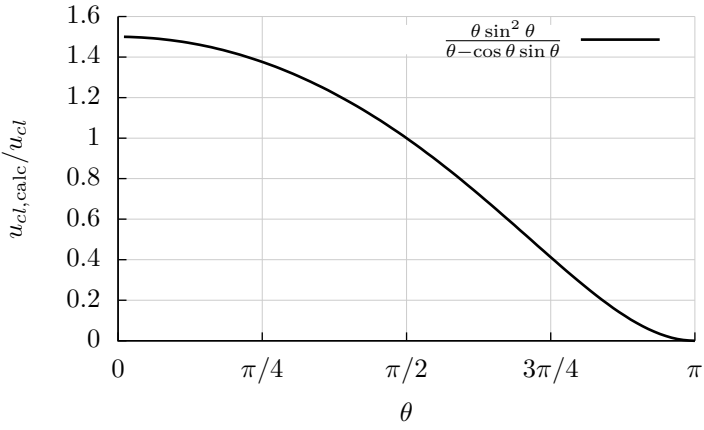

Figure 2.5: Right-hand-side of Eq. (2.64). The correct contact line velocity is only predicted near $\theta \approx \pi/2$.

b) Calculation of the propagation velocity of the contact line The approach used in the present study for calculation of the value of u_{cl} is illustrated in Fig. 2.4. From geometrical considerations, assuming that the surface of the liquid interface is planar,

$$u_{\mathrm{I}} - r\dot{\theta} \approx u_{\mathrm{cl}} \sin\theta, \tag{2.65}$$

where $\dot{\theta}$ is the rate of change of the contact angle, r is the distance from the point at the interface to the contact line. A similar approach has been used in [74] for an axisymmetric case. It was shown that the approach for the calculation of the contact line velocity based on Eq. (2.65) predicts its magnitude with high level of accuracy. It should be noted that expression Eq. (2.65) does not require the assumption of the creeping flow in the corner since it is based exclusively on geometrical considerations.

In a general three-dimensional case if the value $r\dot{\theta}$ is much smaller than u_{cl} the expression for the velocity of the contact line is

$$u_{\mathrm{cl}} = \frac{\mathbf{u}_{\mathrm{P}} \cdot \mathbf{n}_{\mathrm{I}}}{\sqrt{1 - \mathbf{n}_{\mathrm{b}} \cdot \mathbf{n}_{\mathrm{I}}}}, \tag{2.66}$$

where the velocity $\mathbf{u}_{\mathrm{P}}$ is obtained by cell centred value at the liquid interface in the vicinity of the contact line. Eq. (2.66) is used in the present study for computing the instantaneous local velocity of propagation of the contact line.

2.5 Summary

The present study applies the *conventional* Volume of Fluid approach to the simulation of various two-phase flows. The solver has been verified extensively in [6] and its performance has been tested in [26]. Additionally, a new boundary condition (BC) has been implemented which is based on the Robin BC to account for pinning in the hysteresis and applies a dynamic contact angle model in the dynamic phase. The implementation allows a simple usage (and extension) of different contact angle models for the dynamic advancing and receding phase. The choice of the specific model is not of great importance in this study, as long as it is a dynamic model. For preliminary tests, a *linear* dynamic contact angle model was often applied which linearly increases the contact angle dependent on the capillary number until a defined maximum contact angle is reached. The

results are comparable to the one using Kistler's model. Nevertheless, most simulations presented here used Kistler's model, if not stated differently.

For the cases in Sec. 5, a constant contact angle model was chosen and modified such, that the contact angle at the wall is prescribed for each cell individually with a constant value calculated from analytical considerations. This allows to mimic geometrical changes of the solid without resolving them, as it will be shown.

3 Wetting of a Smooth Wall

This chapter presents a numerical simulation of a wetting scenario. In the first section, a drop impact on a dry, solid surface is investigated. Next, drops on inclined surfaces are analyzed and compared to analytical results. The present simulations focus on the contact line pinning. The advantages of the numerical boundary condition respecting hysteresis effects is shown.

3.1 Droplet Wetting

If a drop impacts onto a solid substrate, it is not in its equilibrium state. Thus it will start to spread and wet the substrate. The specific dynamics depend on several parameters like liquid properties, surface roughness and droplet diameter [73].

In the following section, the drop spreading after its normal impact onto a dry rigid smooth substrate is investigated. The spreading diameter d is made dimensionless by division with the initial drop diameter D before impact as $d' = d/D$. The time t is multiplied by the impact velocity $\mathbf{U}$ and divided by initial diameter D: $t' = t \cdot \mathbf{U}/D$.

The phenomena of high-velocity impact can be subdivided into four different stages: A first *kinematic phase* in which the dimensionless drop diameter increases approximately with ${t'}^{0.5}$, independently of the mentioned parameters. Afterwards, in the *spreading phase*, the propagation of the contact line is determined by the fluid and substrate properties. A small advancing contact angle results in a fast and large spread, whereas a large hysteresis can influence the dynamics, resulting in smaller spread factors. This is followed by the *relaxation phase*, which is governed mainly by the hysteresis. If the receding contact angle is small and the hysteresis large, the contact line will remain stationary at the maximum spread. The dynamics generated during the spreading phase are compensated by a change in the contact angle. If the hysteresis band is small and the receding contact angle large, a receding phase, where the contact line contracts back to the center, can be observed. It can even lead to a (par-

Table 3.1: Experimental setup taken from [73].

Material	smooth PVC
Hysteresis (θ_A, θ_R)	100°, 12°
Roughness (µm)	6.2
Roughness characteristic wavelength (µm)	300
Drop diameter (mm)	2.65
Impact velocity ($\mathrm{m\,s^{-1}}$)	1.22
Weber number	54

tial) rebound of the drop. Moreover, if the surface is highly wettable, the contact line continues to spread slowly over the surface.

The numerical studies of drop impact onto dry surfaces are numerous and have already been mentioned in Sec. 1.8, but typically focus on the dynamic phases during spreading and receding to show the effects of a dynamic contact angle. In this study, the relaxation phase, where the contact line remains stationary, is of interest. Thus, the drop impact onto smooth PVC is investigated and compared to the experimental observations of Rioboo et al. [73]. The roughness of the substrate results in a contact angle hysteresis which was measured as $\theta_A = 100°$ and $\theta_R = 12°$. Rioboo et al. reported that *a receding motion is found only for the wax surface*. On the PVC surface, the contact line remains stationary after the maximum spread is reached.

3.1.1 Numerical Setup

In order to keep the computational effort reasonable, the axisymmetry of the impact scenario is exploited. Thus, only a slice of the domain is simulated whereas the influence of the circular domain is represented by a *wedge* boundary condition, as outline in Sec. 2.3.4. This simplification is not capable to account for the three-dimensional effects known as *fingering*, which occur due to instabilities at high impact velocities. Therefore only the cases with $We < 60$ are considered. The boundary and initial conditions are given in Tab. 3.1.

The computational mesh comprises 480 x 800 hexaedral cells in a bounding box of 6 mm x 10 mm. Thus, the cell size is 1.25×10^{-5} m which gives about 124 cells per radius. The Courant number limit is 0.2.

Two comparative simulations are performed, one using the pinning boundary condition, the other one with a dynamic contact angle boundary condition using Kistler's model. The pinning BC uses as well Kistler's model for the dynamic part.

3.1.2 Results

Fig. 3.1 show the dimensionless diameter over the dimensionless time for a drop impact onto smooth PVC. The focus of the analysis is on the behavior after the maximum spread at about $t' \approx 4$. In the experiments, the drop diameter remains constant until $t' \approx 10$. This behavior is correctly reproduced by the numerical results using the pinning boundary condition. Using the *conventional* dynamic contact angle boundary condition, the drop diameter does not remain constant at any time. Instead, after its maximum spread at $t' \approx 5.5$ it starts to recede and the drop diameter shrinks.

For a deeper insight, further investigations are made in Fig. 3.2. It shows the dimensionless drop diameter, the contact angle and the contact line velocity over the dimensionless time on smooth PVC using the newly developed pinning BC as well as the conventional dynamic contact angle BC. The horizontal lines in the plot of the contact angle indicate the advancing and receding contact angles, respectively. As reported by Rioboo [73], the initial phase is universal, thus the propagation and contact angle look similar in both cases: *the drop resembles a truncated sphere* [73] which also explains the initial contact angle to be around 90°. The contact line propagates until $t' = 4$, along the way, the contact angle is partly beyond, partly within the hysteresis. Nevertheless, the motion is inertia driven, thus, the contact angle has only minor influence on the evolution in this phase. Afterwards, the contact angle remains in the hysteresis band, fixing the contact line, which is also confirmed by the plot of the contact line velocity. As outlined before, this is agreement with the experimental observations by Rioboo et al. [73] stating, that no receding phase was observed for the impact on smooth PVC. Nevertheless, the drop diameters are not comparing very good in Fig. 3.1. The differences can be associated the uncertainties of the input parameters like impact velocity and drop diameter. Especially the initialization of the spherical drop on a Cartesian grid introduces differences in the final drop volume. As the focus on the present study was only on the receding phase and whether the contact angle will contract for the given contact angle

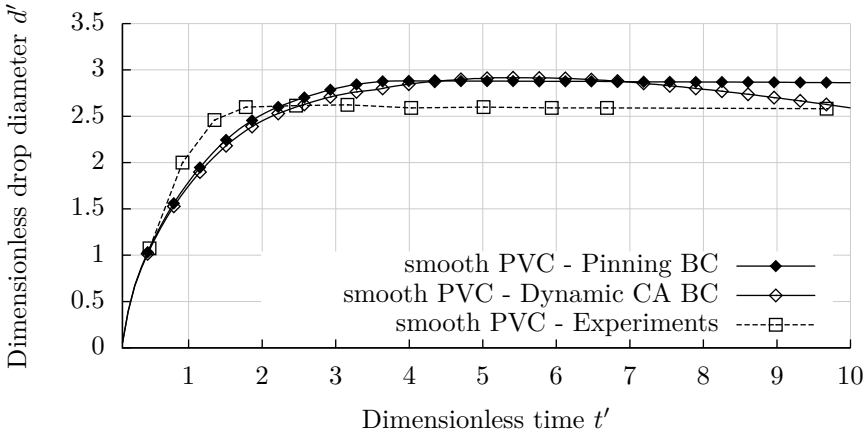

Figure 3.1: Results of the numerical simulation of a drop impact onto smooth PVC. As in the experimental results, using the pinning boundary condition, the drop diameter remains constant after the maximum spread. The pure dynamic contact angle boundary condition does not show any pinning of the contact line.

hysteresis, this difference was neglected. The important phenomena of the pinned contact line at maximum spread for the newly developed BC compared to the immediate contraction of the drop with the conventional approach showed the improvement by the BC as expected.

The conventional dynamic contact angle boundary condition is not able to capture the effects of pinning within the hysteresis, which can be clearly seen as the contact angle is within the hysteresis band, but the contact line velocity is non-zero for all time.

3.1.3 Summary

This section presented numerical results of droplet impact situations with $We \approx 50$ on smooth PVC. The hysteresis of the substrate determines the behavior in the receding phase. For surfaces with a large hysteresis, the contact line remains pinned at maximum spread. This is correctly predicted by the numerical simulations using the pinning boundary condition, whereas the pure dynamic contact angle boundary condition fails in pinning the contact line. Thus, for low Weber number cases it is necessary to account for surface roughness in the numerical simulations by taking the effect of the hysteresis into account.

3.2 Drop on an Inclined Wall

In order to validate the code, the described boundary condition has been applied to the numerical simulation of the incipient motion of a drop an an inclined surface and the predictions of computations are compared to the existing theoretical models and experimental data. A drop is placed on an initially horizontal surface which is inclined constantly until a critical inclination angle γ_{crit} at which the drop starts to move is found.

3.2.1 Introduction

Drops on inclined surfaces have been studied analytically [33], experimentally [71] and numerically [29] by several researchers.

The analytical prediction of γ_{crit} of a two-dimensional drop is a result of the advancing and receding contact angles, as well as the fluid properties.

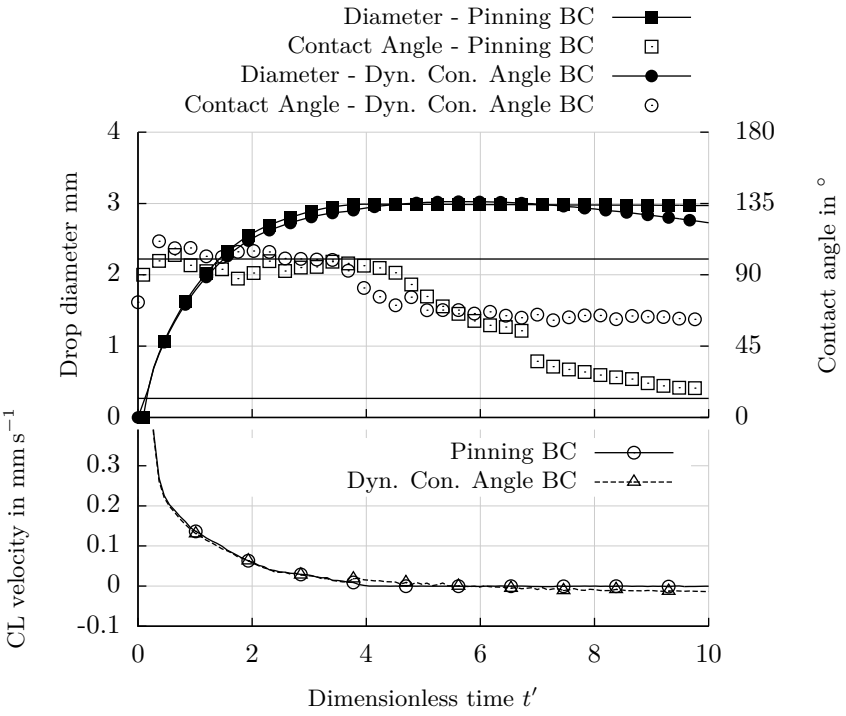

Figure 3.2: Results of the numerical simulation of drop wetting on smooth PVC using the pinning BC and the *conventional* dynamic contact angle BC. The upper plot shows the contact angle and the drop diameter. The hysteresis band is indicated with the solid horizontal line. The lower plot shows the contact line velocity being zero, while the contact angle is within the hysteresis if the pinning BC is applied. The contact line velocity for the case of the conventional dyn. contact angle BC is non-zero all the time. Additionally, the contact angle does not tend to the receding contact angle.

Table 3.2: Overview of the numerical setup and the theoretical critical inclination angle given by Eq. (3.1).

Hysteresis		Critical Inclination angle γ_{crit}		
θ_A	θ_R	$\sigma_1 = 0.036$	$\sigma_2 = 0.072$	$\sigma_3 = 0.144$
100°	80°	6.35°	12.77°	26.24°
120°	60°	18.56°	39.54°	
140°	40°	29.19°	77.2°	

Dussan [33] showed that the critical inclination angle can be estimated as

$$\sin \gamma_{crit} = -\frac{\sigma}{(\rho_L - \rho_g)\,\mathbf{g} V_D} \left(\cos \theta_A - \cos \theta_R\right) \tag{3.1}$$

where ρ_L and ρ_G are the densities of the liquid and the gas, $\mathbf{g}$ the gravity, V_D the *volume* (which in the two-dimensional case is the area) of the drop with a contact angle of 90°, respectively. In our simulations, the axis of gravitational acceleration is rotated, instead of rotating the computational domain to simulate the inclination of the substrate. We use the same numerical parameters as [29] which considers three different surface tensions and three different values of the hysteresis and an initial drop radius of 2.7×10^{-3} m. The critical inclination angles predicted by Eq. (3.1) are summarized in Table 3.2.

3.2.2 Numerical Setup

The following numerical simulations are performed on a two-dimensional hexaedral mesh. As an inclination of the substrate shall be simulated, instead of rotating the mesh, the direction of the gravitational acceleration is modified over time. In order to differentiate between stick-slip phenomena, where the contact line pins again after it was propagating and *real* contact line movement, the gravitational acceleration is modified each third written timestep. Thus, if the contact line moves over several consecutive timesteps, the contact line is identified as moving. The drop is initialized just above the wall and spreads towards its equilibrium state before 0.5° inclination angle is reached. In the case of the influence of different initial droplet shapes, the droplets were initialized before the inclination started by a prescribed constant contact angle. The distribution

of the calculated droplet shape was then used for the simulations.

3.2.3 Results

Next, the results for the simulations of drops in inclined walls are presented. The considered cases show an independence to mesh resolution, angular velocity and droplet shape followed by a final comparison to analytical results.

3.2.3.1 Independence to Mesh Resolution

First, the independence of our numerical method to the grid resolution is shown. The mesh is varied from 22 cells per radius (CPR) up to 132 CPR. Fig. 3.3 shows the position of the contact line of the front ($\mathbf{x}_f$) and backmost ($\mathbf{x}_b$) edge of the drop over the angle of inclination on different mesh resolutions for the case of $\theta_A = 100°$ and $\theta_R = 80°$ and a surface tension of $\sigma = 0.036$. Therein, the effect of pinning can be clearly seen, as both contact lines remain constant from the initial horizontal surface up to an inclination angle of about 4.5°. Then both contact lines start to propagate. The theoretical critical inclination angle is indicated by the vertical line at 6.35°. The inclination angle of incipient motion is predicted identically for all resolutions, even though the slope in the moving phase is slightly different on the coarsest mesh. Thus, for the following studies we use 43 cells per radius.

3.2.3.2 Independence to Angular Velocity

The angular velocity of the inclination of the substrate should be slow enough that it does not influence the moment of incipient motion. Thus, three different velocities are applied and compared in Fig. 3.4 for the case of $\theta_A = 100°$ and $\theta_R = 80°$ and a surface tension of $\sigma = 0.036$. The contact lines at both ends remain pinned until an inclination angle of 4.5° is reached as in the previous study. Obviously, as the angular velocities of the inclination of the plate are different in the three cases, their slope in the phase of propagation is not identical. However, the moment of incipient motion is the same for the three angular velocities. For the following studies, the angular velocity is set to $5.625\,° \,\mathrm{s}^{-1}$ in order to keep the computational time reasonable low.

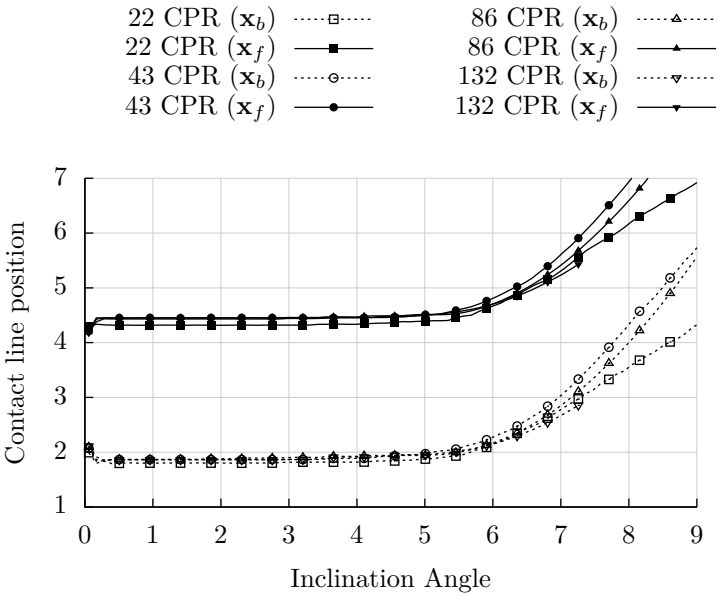

Figure 3.3: Simulation of a 2D drop on solid substrate which is inclined over time on different mesh resolutions. The plot shows the position of the contact line of the front ($\mathbf{x}_f$) and back ($\mathbf{x}_b$) against the inclination angle of the substrate. The rotation velocity is $5.625\,^\circ\,\mathrm{s}^{-1}$, $\theta_A = 100^\circ$, $\theta_R = 80^\circ$ and $\sigma = 0.036$.

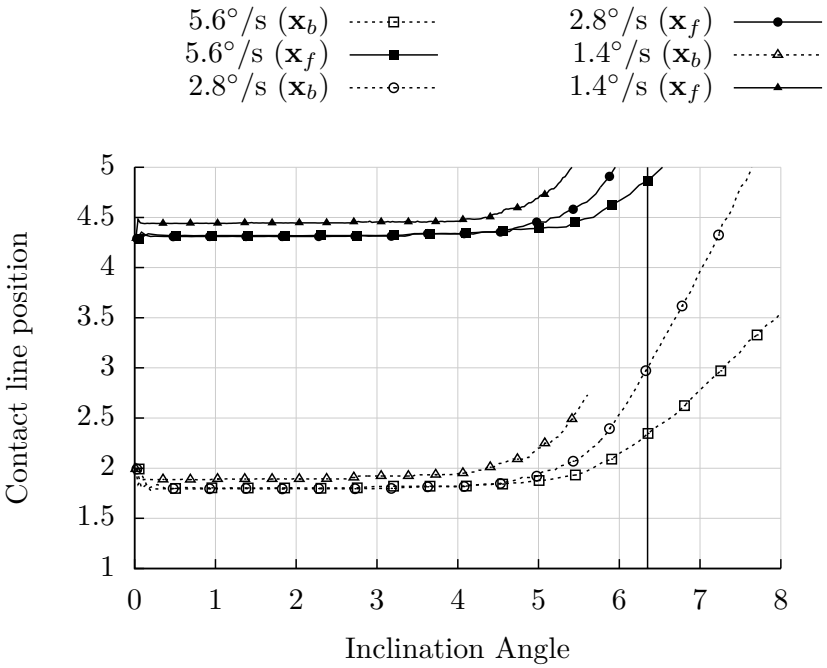

Figure 3.4: Simulation of a drop in a plate which is inclined with different angular velocities. The plot shows the position of the front ($\mathbf{x}_f$) and rear ($\mathbf{x}_b$) contact line against the inclination angle. The angular velocity does not influence the point of incipient motion.

3.2.3.3 Independence to the Initial Drop Shape

The shape of a drop in equilibrium is a result of the *history* of how the drop has been placed. Especially for a large hysteresis, the initial static shape of the pinned drop can be flat, taking the static contact angle near the receding contact angle, as well as a very spherical shape close to the advancing contact angle. Two possible initial shapes for a hysteresis of $\theta_A = 120°$ and $\theta_R = 60°$ are depicted in Fig. 3.5. Their influence to the critical inclination angle is investigated next. One expects, that the

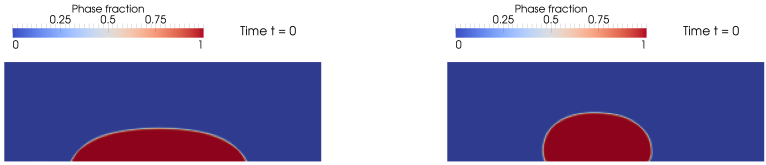

(a) $\theta = 60°$ (b) $\theta = 120°$

Figure 3.5: Initial drop shape for an initial contact angle of 60° (a) and 120° (b). The influence of the initial shape to the critical inclination angle is studied in Fig. 3.6.

critical inclination angle should not depend on the initial shape. In the case of an initial *flat* drop with a contact angle close to the receding contact angle has to increase the contact angle at the front until it overcomes the advancing contact angle. This would lead to a movement of the rear contact line while the contact line at the front would be pinned. Thus, the contact angle at the front increases until the advancing contact angle is reached and both contact angles are beyond the hysteresis.

For an initially *spherical* drop, it would be the other way round: As the contact angle at the front is already close to the advancing contact angle, the contact line would propagate, while the rear contact line remains pinned. The rear contact angle decreases until, at both ends, the hysteresis is exceeded.

This is confirmed in Fig. 3.6 where the critical inclination angle of two different initial configurations are compared for two different hysteresis values and two different surface tensions. It can be clearly seen, that one of the contact lines remains pinned, while the other one propagates until,

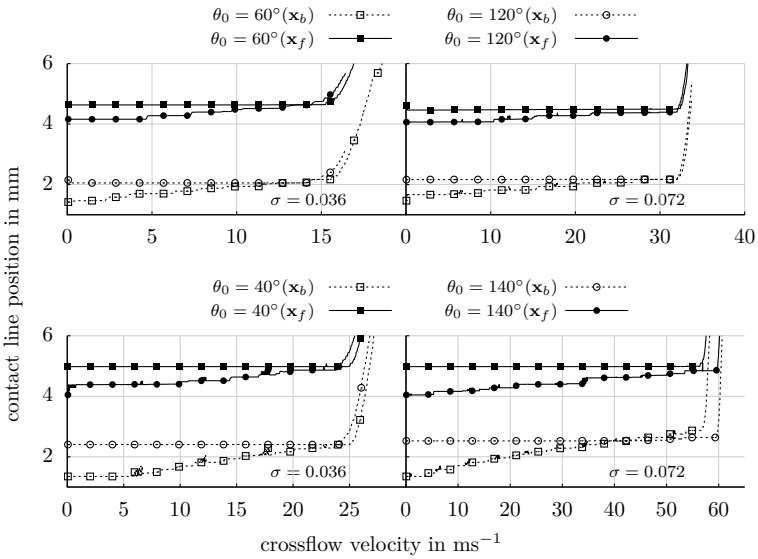

Figure 3.6: The plot shows the backmost and frontmost contact line position of a drop on horizontal surface which is gradually inclined. It compares different initial drop shapes (see Fig. 3.5). The initial shape has no significant influence on the critical inclination angle, as expected.

at both ends, the hysteresis is exceeded. For a hysteresis of $\theta_a = 120°$ and $\theta_r = 60°$ and $\sigma = 0.036$ this is the case at an inclination angle of 15°. For $\sigma = 0.072$ at about 32°. For the great hysteresis of $\theta_a = 140°$ and $\theta_r = 40°$, the same behavior can be seen at an inclination angle of 24° for $\sigma = 0.036$ and 57° for $\sigma = 0.072$. In the very last plot, a slight deviation between the two initial conditions can be seen, which are subjected to inertial effects, when the trailing edge *pushes* the drop.

Fig. 3.6 shows also some small *parasitic* movements of the contact line, which can be seen as small variations in the contact line position. These movements are associated to local stick-slip phenomena: If the contact

angle in a cell decreases below the hysteresis band, the switch of the numerical boundary condition allows a propagation of the contact line into the bulk of the drop. If the bulk of the drop does not move, the contact angle increases again, resulting in a new (larger) contact angle within the hysteresis band and consequently the contact line is pinned again. This can be seen as a deficit of the numerical method, but the stick-slip phenomena is also reported in literature [81]. Additionally it might also be associated to a shortcoming of the applied VOF method: As the interface is artificially thickened over some cells, the boundary condition might switch between the two states over the interface thickness.

3.2.3.4 Final overall two-dimensional tests

According to the prior studies, the set of configurations of Table 3.2 are simulated in a two-dimensional setup. For all simulations the resolution is set to 43 CPR with an angular inclination velocity of $5.625\,^\circ\,\mathrm{s}^{-1}$. The numerical results are compared to the analytical solution of Eq. (3.1) and shown in Fig 3.7. For small critical inclination angles, the agreement is rather good. At the very high critical inclination angles, the deviation gets larger. This might by due to the fact, that in most of these cases, the trailing edge advances before the contact line at the front moves. Thus, inertia effects can lead to an earlier propagation of the drop compared to the static analysis of Eq. (3.1). However, the overall agreement compared to a pure Neumann BC is significantly improved. Using the Neumann BC solely cannot fix a drop at its position. Thus, the drop would move at any inclination angle.

3.3 Conclusion

In this section two typical scenarios of drop-wall interactions were presented. First, the normal drop impact onto a horizontal dry surface at a low Weber number was analyzed. Depending on the material properties of the surface the drop spreading and receding shows different outcomes [73]. On very rough surfaces with a great hysteresis, no receding motion can be seen, The numerical simulation of this situation was presented. On the one hand, using the *conventional* dynamic contact angle boundary condition, pinning was not observed on smooth PVC. Using the newly developed boundary condition, pinning was correctly predicted - the con-

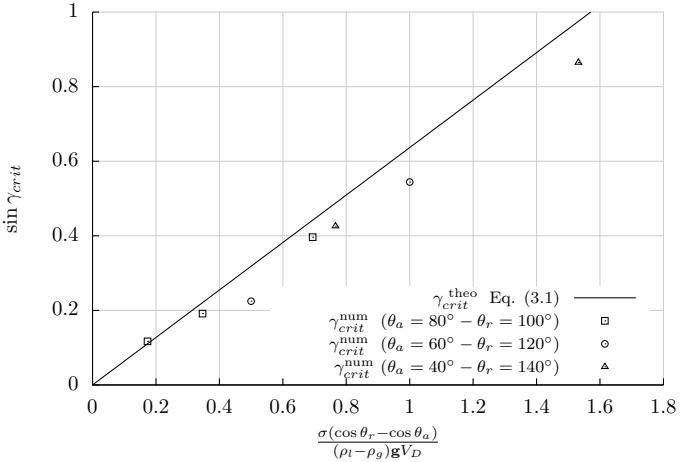

Figure 3.7: Numerical prediction of the critical inclination angle compared to the analytical prediction for different hysteresis values and surface tensions. The parameters can be found in Table 3.2.

tact line remained immobile after the maximum spread as reported in the experiments by Rioboo et al. [73].

For the situation of a drop on an inclined wall, the need for a pinning boundary condition was even more obvious. Using a pure dynamic contact angle boundary condition, a drop slid of the solid surface at nonphysically low inclination angles. With the pinning boundary condition a critical inclination angle at which a drop starts to slide was predicted in good agreement with analytical results given the hysteresis values of the fluid-solid combination.

These *simple* scenarios stress the necessity of an extended boundary condition for the phase fraction as proposed that takes surface roughness into account. The implemented boundary condition fulfills this requirement and is recommended for any simulation where pinning is expected.

4 Drop exposed to shear flow

Investigation of the deposition of drops on a wall in a gas cross-flow is a very current research topic. The bandwidth of applications reaches from coating operations and oil recovery [27] in the process industry, cleaning [60, 92] up to biological applications [48].

Several studies analyzed the droplet formation computationally [87], numerically [54, 85, 91] and experimentally [65]. Additionally, [50] analyzed droplet deposition on micro-grooved surfaces experimentally.

Hu [50] categorized the displacement process in four stages: 1) static state, where the crossflow has no influence on the droplet shape and position, 2) oscillating state, where the contact line still remains immobile, but the interface oscillates, 3) deformation stage, where the droplet deforms and does not deform back into a spherical shape and finally 4) the continuous motion where the drop is deposited from its initial position.

The numerical study of Shirani [85] focuses on the deformation of the drop and the flow patterns around it. The contact line remains stationary and does not account for the dynamic contact angle. Jioa [54] performed numerical calculations using the commercial tool FLUENT. They do not give information about the boundary conditions at the contact line, thus, it is assumed that they do not use dynamic contact angle models or account for hysteresis effects. Theodorakakos et al. [91]account for hysteresis effects in a VOF-framework by introducing an adhesion force governed from the uncompensated Young's law.

4.1 Experimental Method

Comparative experiments on drop shedding by an air crossflow have been performed to validate the effect of pinning of the proposed method. A schematic of the experiment is depicted in Fig. 4.1. The overall length of the facility is about 1.5 m and consists of the fan (1) followed by a diffuser (2) and several flow straighteners (3-7) before the flow enters the test

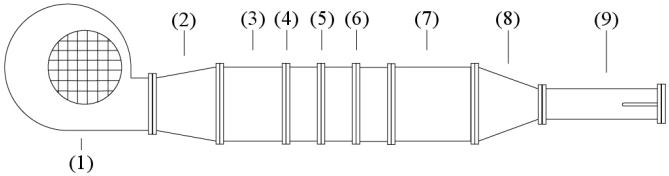

Figure 4.1: Schematic setup of the wind tunnel for experiments.

Table 4.1: Hysteresis values of the different substrates.

Substrate	θ_R	θ_A
Acrylic Glass	$25 \pm 5°$	$72 \pm 7°$
KIWI© Coating	$67 \pm 5°$	$87 \pm 3°$
Teflon Coating	$100 \pm 6°$	$107 \pm 2°$

section (9) through a nozzle (8). In the test section an acrylic glass plate is mounted on which the drop is placed. Water at ambient temperature with a volume of 50 µl is used.

The flow rate is increased gradually until the drop slides along the plate. The drop deformation and initial propagation was captured by a camera (Nikon D5100 with a zoom lens and a macro extension tube). Thus, the critical inflow velocity at which the drop starts to move can be identified.

From these images the static values of the advancing and receding contact angle are measured on three different substrates: pure acrylic glass, teflon coated acrylic glass and KIWI© coated acrylic glass. KIWI© is an impregnation spray used for textiles which increases the hydrophobicity of the coated surface. The hysteresis of the three substrates are summarized in Table 4.1. These values were also used in the numerical simulations.

4.2 Numerical Setup

The new boundary condition formulation has been applied to a simulation of a single drop exposed to a crossflow. A 3D calculation has been performed using a symmetry plane in the streamwise direction, cutting

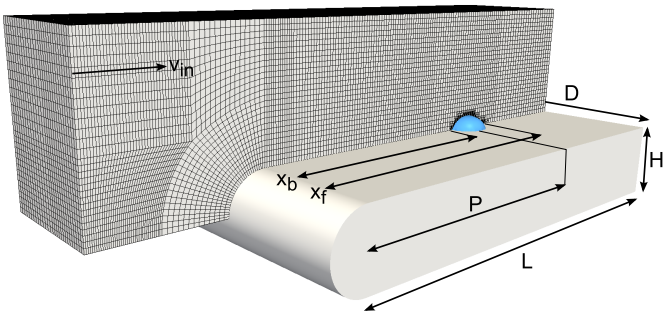

Figure 4.2: Illustration of the computational domain. The length L of the plate is 120 mm, its depth D values 80 mm with a height H of 12 mm. The drop is placed 40 mm behind the tip of the plate. x_b and x_f are the distance between the tip of the plate and the back and front of the drop respectively.

the drop in its center. The computational domain is illustrated in Fig. 4.2. The inflow velocity increases from 0 to $10\,\mathrm{m\,s^{-1}}$ in 3 s. To keep the number of computational cells, and consequently the computational time, reasonably low, dynamic mesh refinement in the area of the interface is used. The ratio of cells per drop radius around the interface is approximately 16 for the initial drop radius of 2.285 mm. The flow rate of the crossflow was prescribed as a boundary condition on the inflow patch on the left hand side. After the calculation, the time at which both contact lines (advancing and receding) move were identified as the critical flow velocity for incipient motion.

The numerical simulations do not use a turbulence model. A similar geometry as used in the present study has be analyzed in single-phase in the ERCOFTAC testcase T3L4 [42]. They report a separation bubble directly behind the curved tip of the plate. Reattachment is predicted at about $x/D = 2$, where x is the distance to the tip of the plate and D the diameter of the plate. The drop in the experiments and the simulations is at $x/D = 4.167$ and consequently far away from the separation bubble. Placing the drop in this bubble led to a propagation of the drop in upstream direction. A plot of the streamlines in a single phase simula-

tion showed similar results to the reported ones. The Reynolds number relative to the diameter of the plate at an inflow velocity of $10\,\mathrm{m\,s^{-1}}$ is $Re_D = 7930$. Savory [78] identifies the critical Reynolds number (turbulent drag) for a solid hemisphere on a substrate at about 5×10^4. Thus, neglecting turbulent effects is certainly a strong simplification but the characteristics as well as the comparison to the experiments are rather good.

Three different substrates are analyzed. The difference of the substrates affects the values of the contact angles bounding the hysteresis band (θ_a and θ_r). They are respected for in the boundary condition of the numerical simulations and need to be provided as an input. For each substrate, they were measured experimentally from the images at the point of incipient motion.

4.3 Results

To begin with, the critical crossflow velocity between the experiments and the numerical simulations are compared. In Fig. 4.3 the contact line position is plotted against the crossflow velocity for three substrates. For all of them, the predictions by the numerical simulations compares well to the experimental results. Slight deviations between simulation and experiment can be subjected to the experimental uncertainties that are not reproduced in the numerical simulations: In the experiments, the measured contact angles varied within 2° and 7°. In the numerical simulations, averaged values of the hysteresis were chosen. The effect of the new boundary condition can be clearly seen in the pinned state while the contact lines at both ends remain pinned. The receding contact line in this case is the upstream part of the drop. In all cases, this contact line moves first, resulting in an increase of the contact angle at the advancing front at the downstream part of the drop. Finally, at both ends of the drop, the hysteresis is exceeded and the drop starts to move. This point is identified in the numerical simulations by the sampled position of the interface at the solid surface. If this position changes for each following timestep at both ends of the drop, the critical velocity is identified. The critical inflow velocities for the experiments and the simulations are compared in Table 4.2. For all substrates, a pure dynamic contact angle boundary condition using a Neumann BC made the drop slide immediately after the inflow was started.

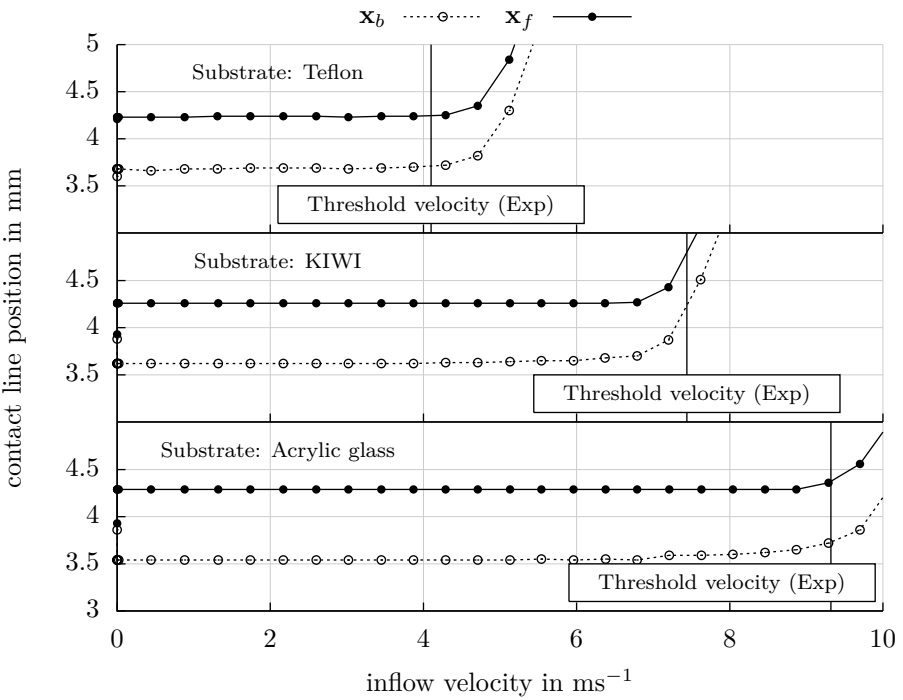

Figure 4.3: Comparison of the position of the frontal and rear contact points at various crossflow velocities and onset of the incipient motion on the three substrates. The corresponding critical velocity measured in the experiments is indicated by a vertical line.

Table 4.2: Critical inflow velocities in the experiments and simulations.

Substrate	v_{crit} Experimental	v_{crit} Numerical
Acrylic Glass	$4.3\,\mathrm{m\,s^{-1}}$	$4.73\,\mathrm{m\,s^{-1}}$
KIWI© Coating	$7.44\,\mathrm{m\,s^{-1}}$	$7.08\,\mathrm{m\,s^{-1}}$
Teflon Coating	$9.32\,\mathrm{m\,s^{-1}}$	$9.6\,\mathrm{m\,s^{-1}}$

Additionally, the deformation of the drop is qualitatively compared in the initial stage and just before the drop begins to propagate (Fig. 4.4). In the upper row, the initial state of the drop prescribed by the contact angle is comparable between the experiments and numerical calculations. Deviations, as seen for example for the KIWI coated substrate are subjected to the history of the drop placement during initialization. As the hysteresis for this substrate is rather great ($\theta_a = 126°$ and $\theta_r = 68°$), all initial setups in this range are *valid*.

The deformed drops just before the propagation qualitatively compare to the images taken in the experiments. Due to the slow critical inflow velocity the drop on the teflon coated substrate is small compared to the strong deformation of the acrylic glass with the great hysteresis. The qualitative comparison of the shape and the quantitative comparison of the critical inflow velocity show that the mechanisms in this configuration are correctly captured by the model.

4.4 Conclusion

This chapter presented a further scenario where contact line pinning is expected and is the key feature for a correct numerical prediction. A drop exposed to a crossflow starts to move at a critical inflow velocity that depends on the hysteresis parameters. A large hysteresis allows large deformation of the drop before the static advancing and receding contact angles are exceeded. Thus, the critical inflow velocity is high. On smooth surfaces, the drop slides already at low velocities as small deformations already introduce the slip at the contact line.

Both, experimentally and numerically, three different surfaces (acrylic glass, KIWI coated acrylic glass and teflon coated acrylic glass) were analyzed and a critical inflow velocity identified. The numerical extension for accounting for surface roughness predicted this critical inflow velocity in very good agreement to the experimental results. The *conventional* dynamic contact angle boundary conditions failed in this scenario. Any small inflow velocity was sufficient to move the drop down the surface, therefore no results with this approach were shown. Additionally, also the deformation of the drop just before the movement compares qualitatively with the experiments.

This scenario with a wide variety of real applications like rain drops

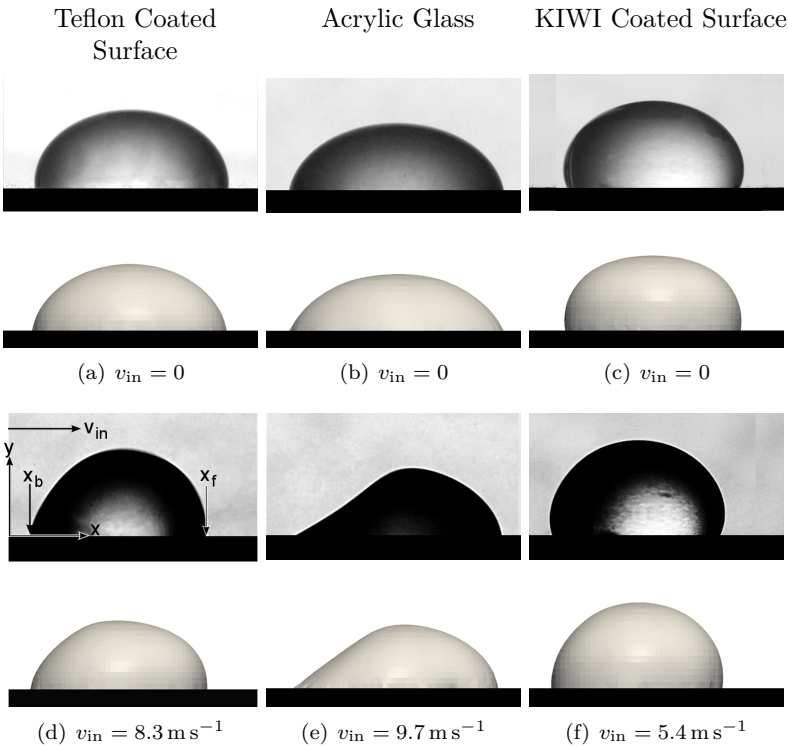

(a) $v_{\text{in}} = 0$ (b) $v_{\text{in}} = 0$ (c) $v_{\text{in}} = 0$

(d) $v_{\text{in}} = 8.3\,\text{m}\,\text{s}^{-1}$ (e) $v_{\text{in}} = 9.7\,\text{m}\,\text{s}^{-1}$ (f) $v_{\text{in}} = 5.4\,\text{m}\,\text{s}^{-1}$

Figure 4.4: Comparison of the drop deformation at the initial stage ($v_{\text{in}} = 0$) and just before the drop starts to move (incipient motion $v_{\text{in}} = v_{\text{crit}}$) for the three different substrates.

on windshields or air drying applications stress the necessity of the extension of the boundary condition as presented. It reproduces the complete contact angle hysteresis comprising pinning as well as a dynamic receding and advancing phase.

5 Wetting of Complex Structures

In the following section the numerical simulations of forced wetting of geometrically complex structures will be presented. After a general introduction into the topic in Sec. 5.1, the experiments conducted by Manukyan [61] will be described in Sec. 5.2. Afterwards the numerical studies are shown in Sec. 5.3. This comprises the description of the mesh generation and the analysis of the rise height and contact angles. Sec. 5.6 proposes an approach to model complex geometries by a contact angle boundary condition instead of fully resolving the geometry with the computational mesh. The chapter is summarized in Sec. 5.7.

5.1 Introduction

Wetting of complex surfaces such as chemically heterogeneous or topological complex geometries is a rather new field in research. The wetting behavior can be unexpected such as very high liquid rise, very low adhesion, frictionless motion and super-hydrophobic surfaces. Its controlled application is beneficial for the coating industries such as paper and adhesive tapes, magnetic tapes as well as printing and photographic tapes. In these applications it is necessary to produce thin films rapidly on large substrates.

There exist several coating techniques such as immersion coating (dip coating), spin coating, spray coating, roll-to-roll coating and many more. All of them were developed to apply a thin liquid film over a substrate (partially or completely). Typical challenges are unwanted air entrainment, controlled film thickness and the speed of the coating process. The following investigations are made into the field of dip coating, where the substrate is immersed or drawn out of a liquid pool. Depending on the withdrawal velocity, the substrate will be covered by a thin film or remains dry.

Landau et al. [57] and Deryagin et al. [25] gave an early and extensive analysis of dip-coating on flat surfaces. The literature in the field of

wetting of complex surfaces is limited. The experimental basis for the following numerical studies is given by Manukyan [61], which also provides an overview of some important experimental and theoretical studies [4, 22, 64].

The numerical studies in this field are not numerous. In the field of wetting of complex geometries, the Lattice-Boltzmann method is often applied as it does not need boundary conformal meshes [18, 63, 79]. Herminghaus et al. [43] gave a nice overview of advances in the field of complex surface geometries and investigates a drop on a single groove. He concludes, that the effects from larger scales like pinning and dynamic contact angles play a minor role in the small scaled applications and therefore explains the successful application of the *simple theoretical concepts of wetting* for the complex geometries.

5.2 Experimental Studies of pyramidal structures

Manukyan [61] analyzed various dip coating scenarios for substrates with an engraved array of pyramids (as illustrated in Fig. 5.13). The pyramids' peak-to-peak distance is varied by $\sim$0.5 mm, $\sim$1.0 mm and $\sim$2.0 mm. During the manufacturing process, the exact distances cannot be produced exactly and have therefore been measured using an electron microscope. The measured dimensions are given in Tab. 5.1. The dimensions of the pyramids where chosen to be larger, smaller and much smaller than the capillary length (L_c) of the fluids.

Additionally, Manukyan analyzed two different liquids and three dip-velocity variations. As liquids, PDMS (trimethylsiloxy terminated polydimethylsiloxane) with two different viscosities (10cSt and 100cSt) are used. Their properties are summarized in Tab. 5.2. The dip velocities are varied between $0.424\,\mathrm{mm\,s^{-1}}$, $0.636\,\mathrm{mm\,s^{-1}}$ and $0.848\,\mathrm{mm\,s^{-1}}$. Thus, the resulting Reynolds and capillary number are limited by $0.0125 < \mathrm{Re} < 0.0627$ and $0.004 > \mathrm{Ca} > 0.0002$.

The experimental setup is depicted in Fig. 5.2. The substrate is dipped into or withdrawn from the liquid pool by a step motor and recorded by a monochrome 8-bit high-speed CMOS camera with a pixel size of $10\,\mu\mathrm{m} \times 10\,\mu\mathrm{m}$. The recorded images are evaluated by MathWorks®Matlab Image Processing. Further details about the hard-

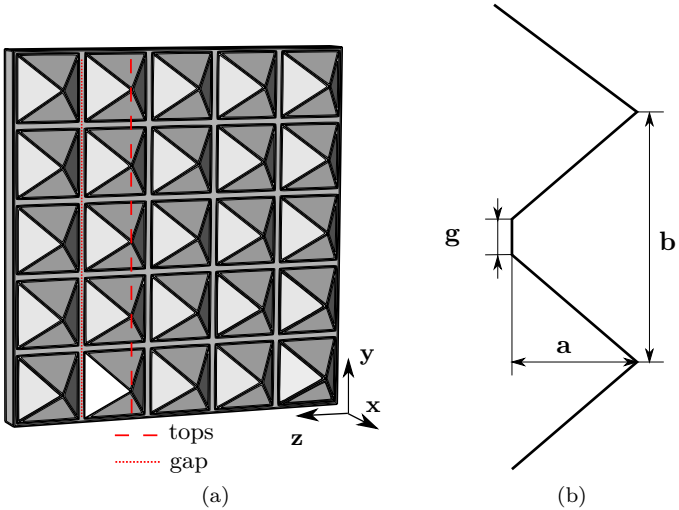

Figure 5.1: An overview of the pyramidal substrate (a) and the definition of the parameters (b).

and software can be taken from [61].

Sec. 5.3 analyzes the possibility of numerically simulating this complex geometry. It poses several challenges starting from the mesh generation (presented in Sec. 5.4.1.1), the boundary condition (discussed in Sec. 5.4.1.2) and the analysis of the numerical results compared to the experimental results (discussed in Sec. 5.4.1.3).

5.3 Numerical Setup

The numerical simulations are performed using the *interFoam* solver as described in Sec. 2. The computational domain comprises 10 pyramids, whereas two symmetries are exploited: One, along the vertical valleys and the second is cutting each pyramid in the middle through its peak (see Fig. 5.3). The dimensions of the pyramids correspond to those given in Tab. 5.1. The distance from the end of the computational domain to the wall is five times the pyramidal height.

pyramid type	a in mm	b in mm	g in mm
0.5 mm	0.382	0.696	0.023
1.0 mm	0.680	1.320	0.072
2.0 mm	1.604	2.448	0.240

Table 5.1: Dimensions of the pyramids corresponding to the definitions of Fig. 5.2(b)

Table 5.2: Fluid parameters

Fluid	ρ [kg m^{-3}]	σ [kg s^{-2}]	μ [kg m^{-1} s^{-1}]	L_c [mm]
PDMS 10cSt	935	20.1×10^{-3}	9.35×10^{-3}	1.48
PDMS 100cSt	970	20.9×10^{-3}	97×10^{-3}	1.48

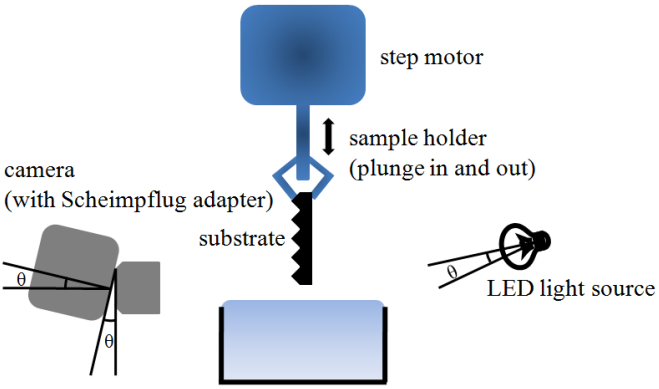

Figure 5.2: Experimental setup for dip coating experiments taken from [61].

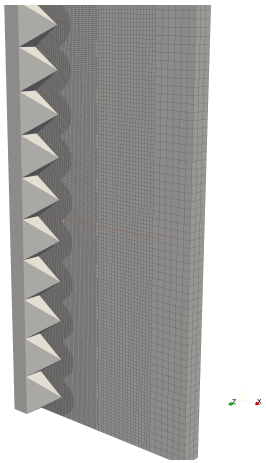

Figure 5.3: Overview of the computational domain with the refinement areas towards the structured surface. The computational domain exploits two symmetries, one along the peaks of the pyramids, the second along the vertical valley.

The cells below a height of 4 mm are initialized with a phase fraction of 1. Before further liquid is injected from the bottom to simulate the immersion of the probe into the water, the calculation runs for one second to let the fluid find an equilibrium state. Afterwards, a constant flow rate from the bottom is prescribed corresponding to the given dip velocity of the experiments. This is numerically easier than *moving* the probe into the liquid pool.

The simulation runs until 2-4 pyramids are covered with fluid. If not mentioned differently, the contact angle is set constant at 48.5° at the wall. In the post-processing step, two quantities are extracted for comparison between the different setups and to the experimental results. On the one hand, the rise height is extracted i) at the wall, ii) at the connecting line of the peaks of the pyramids and iii) 3 mm away from the wall. On the other hand, at the same three positions, the angle between the vertical line through this point and the interface are calculated. Mostly, quantities at the peak to peak line are used for comparison.

The first challenging step for the simulation of the complex geometries is the generation of a suitable mesh. The VOF-Method in the FVM

framework on an unstructured mesh as applied in the present study gives freedom in the mesh generation. However, the several kinks, corners and edges can distort the mesh an lead to unwanted numerical problems. In this study, two approaches of mesh generation are followed. The first one is the use of the tool `snappyHexMesh`, provided by the OpenFOAM toolbox. The second one is the tool `gmsh` [41] to produce a tetrahedral mesh and `polyDualMesh` provided by OpenFOAM to transform it into a polyhedral mesh. Both are presented in detail next.

5.3.1 Hex-dominated meshes with snappyHexMesh

`snappyHexMesh` is a tool that delivers a three dimensional body-conformal mesh with hex-dominated cells. The workflow of the tool is described by the example of meshing the pyramids, that are analyzed in the following.

The first step is to provide a triangulated surface geometry in Stereolithography (STL) format that the final mesh shall conform. Here, this is generated using Siemens NX8. Additionally, a background mesh is necessary, that represents the whole fluid domain. This can be easily produced using the blockMesh tool of OpenFOAM. The geometry has to intersect partially or completely the background mesh (Fig. 5.4(a)). Given this, `snappyHexMesh` produces a body conformal mesh in the following workflow:

1. **Refinement**: If desired, the cells of the background mesh intersected by the geometry are refined (by splitting). This can be repeated several times if necessary. Moreover, several layers of cells can be refined to have a continuous cell size around the geometry.
2. **Cell removal**: After the refinement process, all cells that have more than 50 % of their volume within the geometry are deleted. The result is a staggered mesh (Fig. 5.4(b)).
3. **Snapping**: Iteratively, every vertex of the castellated boundary is *snapped* (moved) onto the surface of the geometry such that the staggered mesh is transformed into a body-fitting mesh (Fig. 5.4(c)).

These steps are visualized for the pyramidal structures in Fig. 5.4.

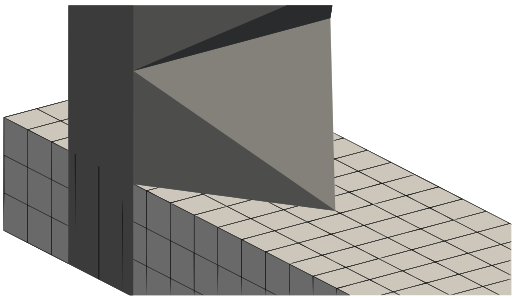

(a) Setup: STL representation of the pyramids in the back intersected by the background mesh.

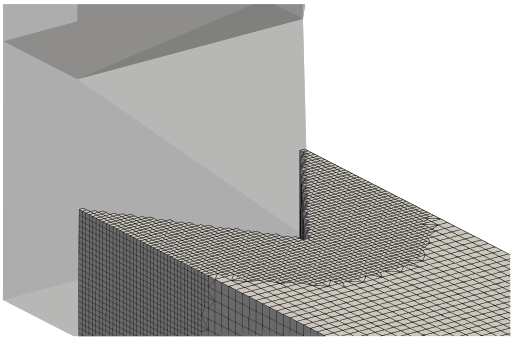

(b) Removal of cells in the geometry.

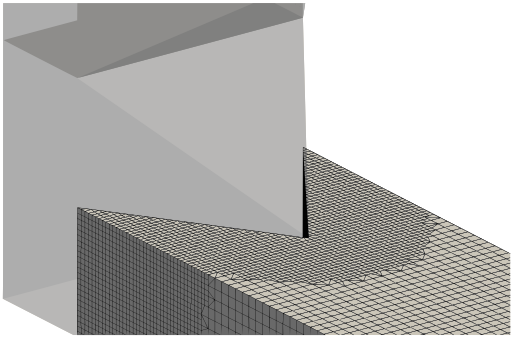

(c) Snapping

Figure 5.4: Visualization of the workflow of `snappyHexMesh` for the pyramidal structures.

5.3.2 General polyhedral mesh with gmsh and polyDualMesh

Another possibility to generate body conformal meshes, is the use of the software `gmsh` [41] and the OpenFOAM tool `polyDualMesh`. `gmsh` is used to setup the geometry and to generate a tetrahedral mesh of the volume. `polyDualMesh` transforms a tetrahedral mesh (generated using the Delauny-Triangulation) and produces a polyhedral mesh. The workflow will be briefly outlined:

- The geometry is set up in `gmsh` defining all points, edges, surfaces and volumes.
- The generated volume can be meshed by the use of the provided algorithms. Here, the *Frontal* 2D-Algorithm [72] is used for the surface meshing and the Delaunay-Algorithm [40] for the 3D meshing.
- The mesh can be transformed to OpenFOAM using the `gmshToFoam` application (Fig. 5.5(a)).
- The tetrahedral mesh can be transformed into a polyhedral mesh by combining a set of tetrahedrons to a polyhedron (Fig. 5.5(b)). The cells at the corner of the mesh have several cell-faces on the same patch. To avoid that, *combinePatchFaces* combines all faces of a cell that are on the same patch to a single face (Fig. 5.5(c)).

The results is a *honeycomb* mesh of polyhedral mesh cells. The steps are visualized in Fig. 5.5.

5.3.3 Comparison of the Meshes

Besides the numerical analysis of the presented meshes in Sec. 5.3.3, a general discussion of the methods is given. The advantages of polyhedral mesh cells against hexaedral cells is a better spatial stencil. As a hexaedral cell typically only has orthogonal faces. Quantities that have fluxes in diagonal direction through the cells are only approximated by those. Polyhedral cells have more smoothly oriented faces and therefore less potential of approximation errors. The drawback is the higher computational cost of these cells as the algorithms always performs a loop over all faces of cell. Thus, the more faces, the higher the computational effort.

The workflow of `snappyHexMesh` is very comfortable as the adaption of

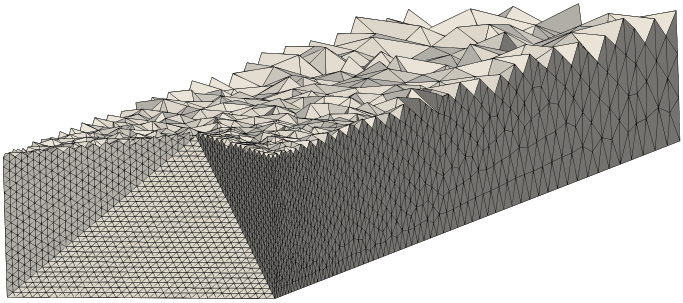

(a) The imported tetrahedral mesh from `gmsh` to OpenFOAM

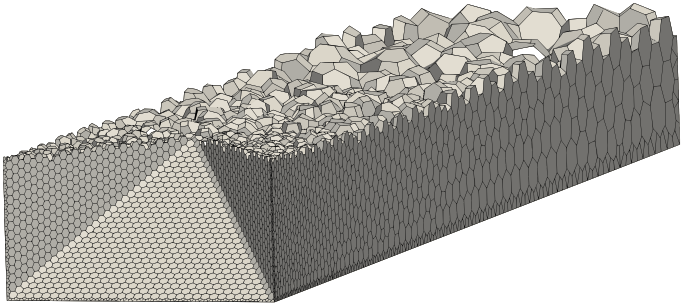

(b) Mesh after `polyDualMesh`

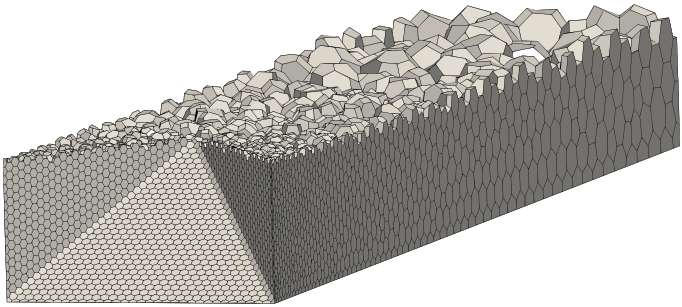

(c) Combined faces of a cell on the same patch

Figure 5.5: Visualization of the workflow of `gmsh` with `polyDualMesh` for the pyramidal structures.

the mesh to the geometry is done completely automatically by the tool, assuming that the STL-representation is provided. If `gmsh` is used, the geometry has to be built manually which can be time-consuming if the geometry is complex. If the geometry is provided by `gmsh`, the meshing and conversion can be automatized as well. Nevertheless, it is not always easy to get valid meshes immediately.

Additionally, it is difficult to preserve sharp edges in both attempts. As it can be seen in Fig. 5.5(a), the provided tetrahedral mesh has sharp edges at the pyramids. In Fig. 5.5(b), they are smoothed out by the construction of polyhedral cells. In general, it is possible to preserve the sharp edges for this mesh, but it led to a bad mesh quality due to some distorted cells at the sharp edge. Using `snappyHexMesh`, the edges are kept sharp, except for some cells. A visual comparison of the edges for the two mesh types is presented in Fig. 5.6

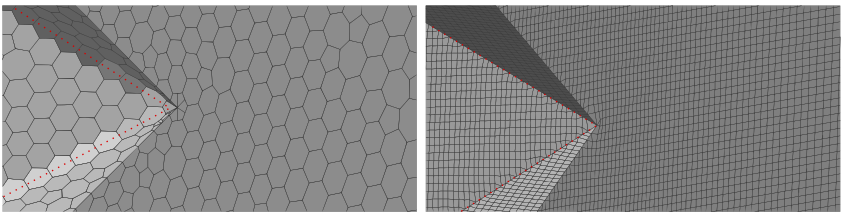

(a) *Round* edges for the polyhedral meshes (b) Sharp edges in the hex-dominated mesh

Figure 5.6: Smoothing of the sharp edges in the polyhedral (a) and hex-dominated (b) meshes.

In Appendix A.1, the two mesh types are compared for the capillary rise on a flat wall. The polyhedral mesh cells converge to the analytical rise height with mesh refinement and are more stable in the static state. The hex-dominated mesh does not converge to the analytic solution. Nevertheless, both calculations estimate the analytical rise height well. In this case, the flow is exclusively governed by the surface tension and the contact angle boundary condition. The following simulations of pyramidal structures are mostly governed by the geometry. Thus, the influence of the mesh type will be less important.

5.4 Results and Discussion

The presentation of the results of the numerical simulations of wetting of the pyramidal structures are organized such, that first, the comparison of different mesh types are presented. Next, the comparison of the static to a dynamic contact angle model is shown. Afterwards, the comparability of the numerical results to the experimental observations are given and the results of the parameter studied as in the experiments are presented afterwards.

5.4.1 Rise Height and Contact Angles

Before analyzing the specific influential parameters, the general evolution of the contact line (described by the rise height and the contact angle) is presented. Basically, the analysis can be split in two regions: One is along the vertical valleys at the wall, the other one is along the peaks.

In the valley, the liquid rises typically about one pyramid higher than along the peaks (see Fig. 5.7(a)). When the surface is immersed into the liquid pool, the liquid rises quickly along the valley between two pyramids until the next *crossing* with the horizontal valleys occurs (see Fig. 5.7(b)). There the liquid penetrates and wets the horizontal valleys. Simultaneously, the liquid rises further upwards and the procedure repeats again (see Fig. 5.7(c)).

Along the peak to peak line, the liquid rise behaves differently. At the peaks, the contact line remains pinned (see Fig. 5.7(a)). The contact angle, relative to a vertical line, increases while the rise height shrinks. When the peak is passed, the contact line propagates slowly to the (prewetted) valley (see Fig. 5.7(b)). Quickly the two regimes combine and the liquid rises up the next side of a pyramid until the next peak is reached where it pins again and the procedure starts again (see Fig. 5.7(c)). These stages are visualized in Fig. 5.7, where at three different timesteps the reconstructed interface is shown.

5.4.1.1 Comparison of the meshtypes

For the 2 mm pyramids at a dip velocity of $0.848\,\mathrm{mm\,s^{-1}}$, the two described mesh types are compared. The pyramids have no gap in between each other which will be discussed more detail later. The rise height

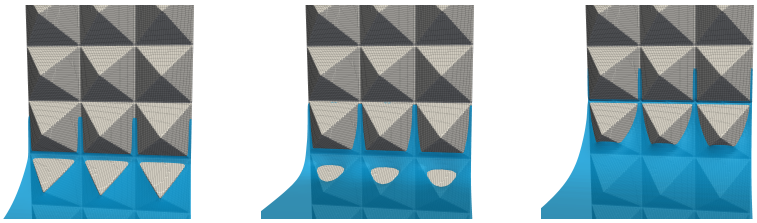

(a) Stage 1: The contact line remains pinned at the edges of the pyramid. The liquid in the valley rises.

(b) Stage 2: The upper side of the pyramid gets wetted, the liquid in the valley rises to the next *crossing*.

(c) Stage 3: The liquid fully wets the upper side of the pyramid and propagates on the lower side of the following pyramid. The liquid in the valley prewets the next horizontal valley and rises upwards.

Figure 5.7: Three selected stages while the liquid wets a pyramid.

and the contact angle at the peak-to-peak line are compared in Fig. 5.8. Comparing the results, the maximum contact angle is significantly smaller on the polyhedral cells than for the hex-dominated cells. Thus, also the rise height for the polyhedral cells is much smoother and smaller. The reason for this behavior is attributed to the edges at the pyramids and how they are resolved by the meshes as outlined Sec. 5.3.3. The edges are smoothed in the polyhedral mesh and are significantly sharper in the hex-dominated mesh. Therefore, also the pinning at the edges is stronger in the hex-dominated mesh. Thus, the predominance the polyhedral cells have for a smooth wall vanish as the sharp corners are not resolved correctly. In the following, the hex-dominated mesh will be applied in the numerical studies. Additionally, the mesh was refined, yielding the same evolution of the contact line and contact angles. The coarser mesh is therefore used during the further procedure.

5.4.1.2 Contact Angle Model

For the 2 mm pyramids at a dip velocity of $0.848\,\mathrm{mm\,s^{-1}}$ without a gap, two contact angle models are compared: A constant contact angle model at 48.5° and a dynamic (Kistler) model with a hysteresis of 30.9/48.5° without any additional treatment of the immobility of the contact line

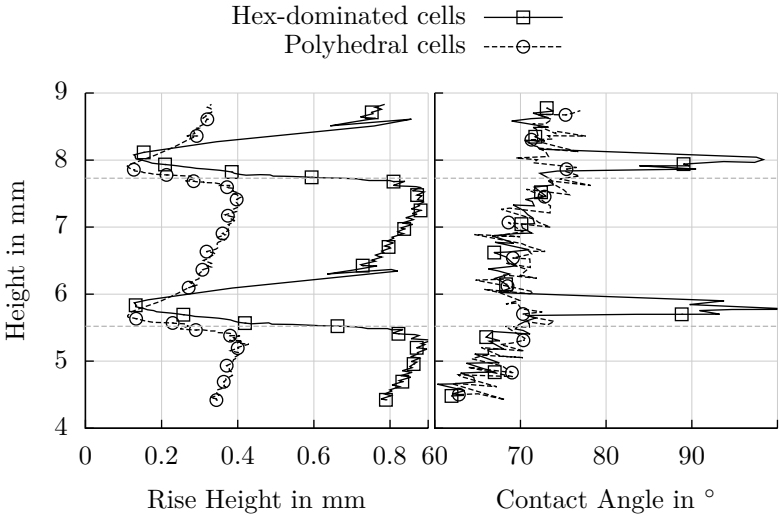

Figure 5.8: Comparison of a polyhedral and hex-dominated mesh for the rise height (left) and the contact angle (right) along the peak to peak line.

due to the hysteresis.

Fig. 5.9 shows the evolution of the rise height and the contact angle along the peak to peak line for the two models. Besides very minor differences for the contact angle at a height of about 7 mm, the results are identical. Pinning can be observed at the pyramid's peaks and can be seen, as the contact angle increases and the rise height shrinks. The effect of pinning in both calculations is introduced without any further treatment in the contact angle boundary condition. Pinning is naturally introduced by the geometrical changes of the boundary at the contact line (e.g. kinks). In this case, these geometrical changes are resolved by the computational domain, thus they do not need to be modeled. As the dynamic contact angle model shows no significant improvement, the following calculations use the constant contact angle model.

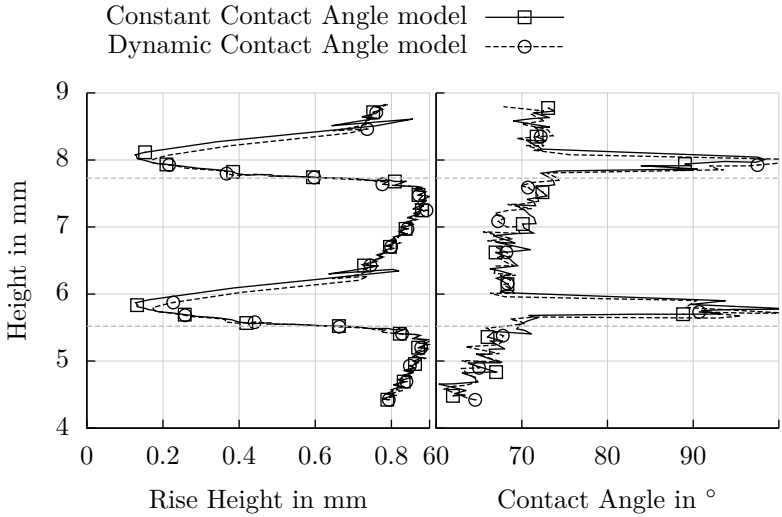

Figure 5.9: Comparison of two contact angle models (constant and dynamic) for the numerical results of the rise height (left) and the contact angle (right) along the peak to peak line. The contact angle model has no significant influence.

5.4.1.3 Comparison with the existing experimental data

The propagation of the contact line over time is especially important when comparing the experimental and numerical results. In general, the techniques for the extraction of the position of the contact line are very different. In the experimental study, a camera was used to take pictures of the liquid rise from a side view. A typical picture and the extracted quantities are depicted in Fig. 5.10. As the images represent a 2D side

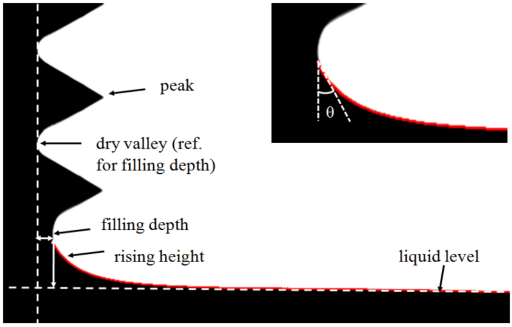

Figure 5.10: A typical picture taken in the experiments and the extracted quantities.

view, it is not possible to differentiate if a detected contact line is on a pyramid or in a valley. Moreover, the liquid rise in the valley can hide a dry valley behind it. Additionally, the resolution of the camera limits the accuracy of the extracted data.

In the numerical simulations, the quantities of interested can be extracted along a given line and are not hidden by any other liquid in the vicinity. Nevertheless, of course also the numerically extracted data have limited resolution and suffer from interpolation errors. The difference, especially concerning the covered two-dimensional view and *exact* extraction in the numerics has to be kept in mind when the results are compared.

A typical issue in this respect is, that the contact line is pinned along the edges of an upper side of a pyramid. While the contact line remains immobile there, the liquid rises in valleys around. In the side view, it appears that the contact line propagates.

A comparison of the rise height from the experiments and a numerical simulation for a pyramid of 2 mm base length is given in Fig. 5.11.

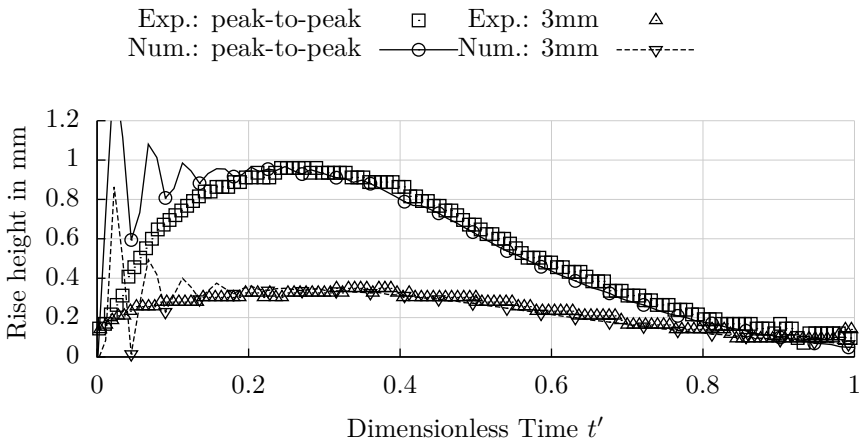

Figure 5.11: Comparison of the experimental against numerical results for the rise height at the peak line and 3 mm away from the wall.

Therein, the liquid rise at the peak to peak line and 3 mm away from the wall are plotted against the dimensionless time. The dimensionless time is calculated by the actual time divided by the total time that is needed to overcome a pyramid. The data from the experiments and the numerical simulation compare nicely from $t' \approx 0.2$. At $t' < 0.2$, the numerical results show a lot more dynamic and large rise variations. On the one hand, they can be attributed to the difference in the sampling technique outlined before. On the other hand, the rise height is too large to be exclusively associated to this shortcoming. The extremely dynamic movement at the beginning of the wetting-cycle is intensified by the constant contact angle model that does not compensate any dynamics by a change of the contact angle. As soon as the strong oscillations are vanished (at about $t' \approx 1.8$), the experimental and numerical results are in good agreement.

5.4.1.4 Parameter Studies

Some of the parameter variations given by Manukyan [61] were also numerically analyzed. This comprises a variation in the dip-velocity for the 2 mm pyramidal structures, a variation in the pyramidal size, a second,

more viscous fluid and an analysis of the influence of the reported gaps between the pyramids.

Dip Velocity For the 2 mm pyramidal structures, the dip-velocity has been set to $0.848\,\mathrm{mm\,s^{-1}}$, $0.636\,\mathrm{mm\,s^{-1}}$ and $0.424\,\mathrm{mm\,s^{-1}}$. The variation has no significant influence on the outcome of the rise height over the dimensionless time as also reported by Manukyan [61] (Fig. 5.12). The pyramidal geometry of the substrate dominates the evolution of the contact line. Dynamic effects like air entrainment due to high velocities are not expected and not reported by Manukyan.

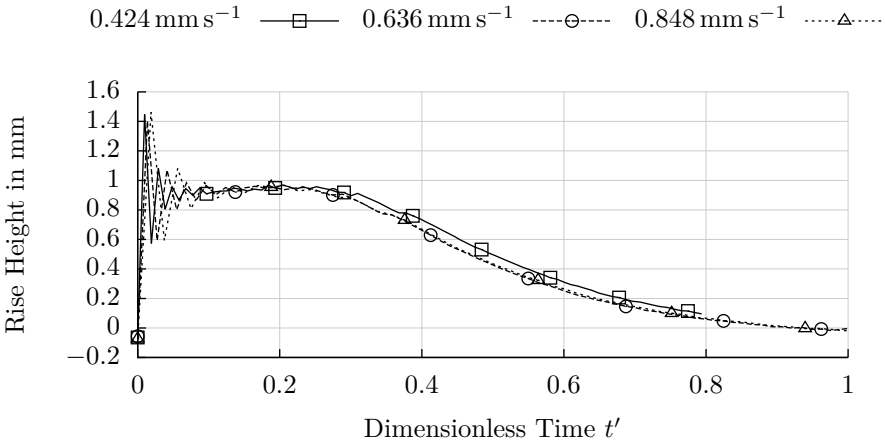

Figure 5.12: Comparison of the three different dip-velocities ($0.848\,\mathrm{mm\,s^{-1}}$, $0.636\,\mathrm{mm\,s^{-1}}$ and $0.424\,\mathrm{mm\,s^{-1}}$) for the 2 mm pyramidal structures. The dip-velocity has no influence on the evolution of the contact line.

The movement of the bulk of the fluid can be seen as a quasi-stationary, whereas the movement within the valleys as well as the sudden movement over the upper part of the pyramids is nonsteady but independent to the dip-velocity.

Pyramidal Size According to the experimental setup, the size of the pyramids have been varied as given in Tab. 5.1. Manukyan [61] reported that the wetting stage, where the contact line moves along the lower side of the pyramid to the peak is not present for the 1 mm and 0.5 mm structures. The reason for that is, that the liquid rise after the pinning at the peak of a pyramid is high enough to completely wet the area to the next peak. Thus, the wetting of the lower side of a pyramid for the two smaller geometries is completely driven by surface tension and the meniscus shape, whereas for the 2 mm pyramids, wetting of the area close to the peak of the lower side is affected by the motion of the substrate.

This effect is also numerically confirmed, and can bee seen, when the temporal evolution of the interface is plotted along the pyramids as done in Fig. 5.13. Each line corresponds to the reconstructed interface every 0.125 s. For the 2 mm pyramids, the interface at the end of the lower side of the pyramid is *pushed* to the peak by the immersion of the substrate (or the inflow from the bottom). The angle between interface at the contact line to a vertical line is close to 0° on the lower side of the pyramid. Thus, the rise height can be calculated to 2.04 mm. This is greater than the peak-to-peak distance for the 1 mm and 0.5 mm pyramids, but smaller than for the 2 mm pyramids, which explains this phenomenon.

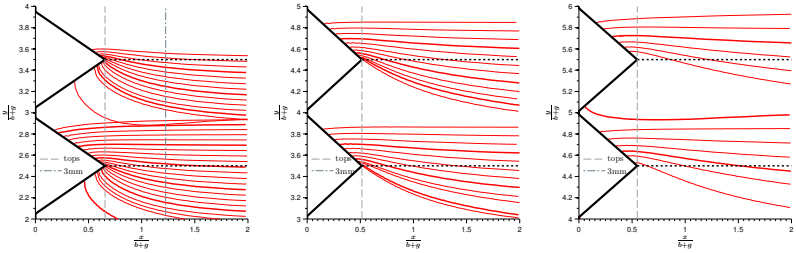

(a) 2mm (b) 1mm (c) 05mm

Figure 5.13: Temporal evolution ($\Delta t = 0.0125s$) of the Interface along the pyramids. Only for the 2 mm pyramids, the contact line remains at the lower side of the pyramid and is approaching the peak by the immersion of the substrate.

Fluid Properties Manukyan [61] varied the viscosity of the fluid as given in Tab. 5.2. This has also been numerically analyzed giving the same

general behavior except the strong oscillations for the PDMS 10cSt vanish for the more viscous PDMS 100cSt. Fig. 5.14 shows the rise height over the dimensionless time of the two fluids. Especially in right after the passing of the peak at $t\prime \approx 0$, the viscous fluid PDMS 100cSt does not oscillate and *overshoot*.

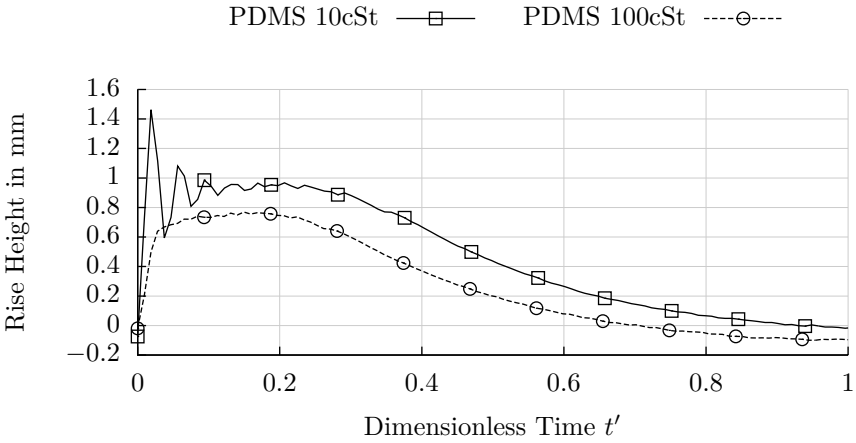

Figure 5.14: Comparison of two different liquids (PDMS 10cSt and PDMS 100cSt) with a dip-velocity of $0.848\,\mathrm{mm\,s^{-1}}$ in 2 mm pyramids. The general behavior is very similar, however the strong oscillations in the beginning do not appear for the viscous PDMS 100cSt.

Gap between the pyramids Manukyan [61] reported small gaps between each of the pyramids. These gaps were not intended, but could not be avoided in the manufacturing process. Their sizes are given in Tab. 5.1. For the 2 mm pyramids, simulations with both, with and without gap are performed. The difference in the numerical mesh can be seen in Fig. 5.15.

Herminghaus et al. [43] analyzed the wetting behavior of a fluid in an infinite wedge formed by two intersecting planes (Fig. 5.16). Although the analyzed dimensions of the substrate are much smaller than those of the experiments analyzed here, the results should be transferable to the present case as Herminghaus reported, that the contact angle θ and the

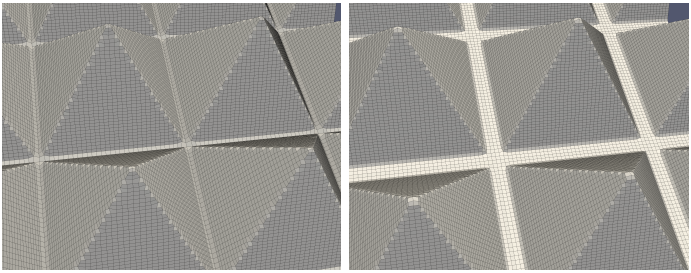

(a) without gap (b) with gap

Figure 5.15: The numerical mesh at the intersections of the valleys without a gap (a) and with the reported gap (b).

wedge angle ψ are the only relevant parameters governing the appearance of different droplet shapes in equilibrium. In the present case, the contact angle measures $\theta = 48.5°$ and the opening angle $\psi = 35°$. The definition of the slope angle is illustrated in Fig. 5.16. The ratio between the contact angle and the opening angle is the decisive factor for the formation of the interface. For the case of $\theta > \psi$, a spherical shape with a *contact point* of the interface in the valley is expected and the three angles are related as

$$\cos\beta \cos\psi = \cos\theta \tag{5.1}$$

and illustrated in Fig. 5.16(a).

For the case of $\theta < \psi$ a liquid filament in the groove is expected as illustrated in Fig. 5.16(b).

This would cause a theoretical infinite rise of the liquid for the present pyramidal structures. However, the wedges are intersected by the horizontal valleys posing an additional edge where pinning is expected. Accounting for the gaps results in the *normal* effective contact angle of 48.5° as the two wedge walls are far apart each other, such that the liquid interface in the gaps is not affected by those. Thus, one would expect a higher liquid rise for the case without the gaps. This is also confirmed by the numerical simulations as illustrated in Fig. 5.17.

Additionally, the liquid rise is not constant over the time, as the vertical valleys have intersections with the horizontal valleys. As the next valley is not in the *close vicinity* of the previous gap (see Fig. 5.15), pinning is

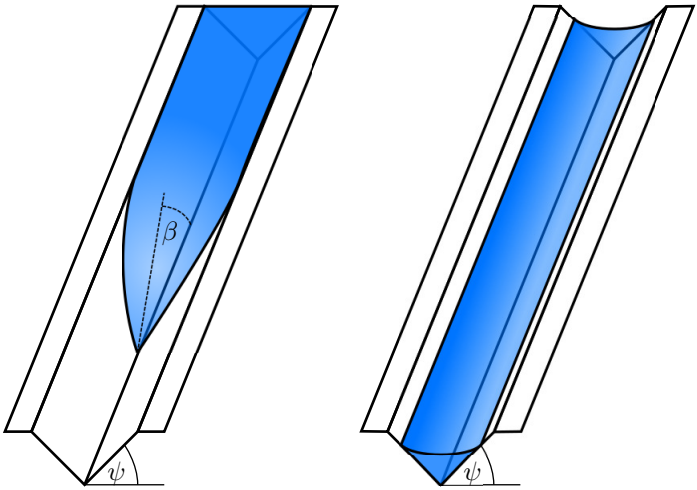

(a) Spherical shape for $\theta > \psi$ (b) Liquid filament for $\theta < \psi$

Figure 5.16: The slope of the liquid interface with slope angle β in a wedge is solely governed by the contact angle θ and the opening angle ψ

more dominant with the gaps. The sudden increase of the rise height in the valley for the case with gap is simultaneously to the *jump* of the contact line along the peaks. This shows, that the rise in the valley is strongly influenced by the motion of the bulk of the fluid. For the case without the gaps, the evolution of the rise height seems to be more independent of the *wetting cycle* along the peak-to-peak line, as also observed in the experiments.

As reported in Sec. 5.4.1.3, the comparability between the numerical and experimental results is in good agreement if the gaps are not considered in the numerical simulation. The exact shape of these gaps is not known, giving an additional uncertainty about their correct modeling.

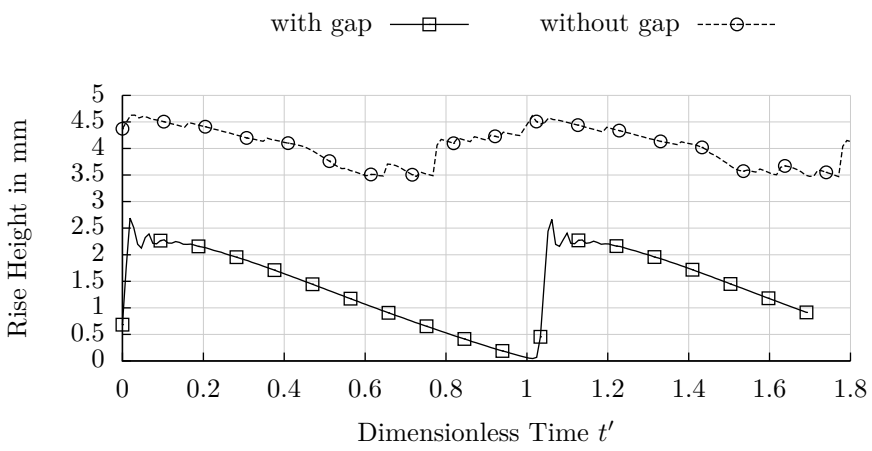

Figure 5.17: Comparison of the rise height in the vertical valleys for the 2 mm pyramids with and without a gap. The liquid rise is much higher without the gaps.

5.5 Summary for the Three Dimensional Resolved Simulations

The section presented a feasibility study of the numerical simulation of the experiments performed by Manukyan [61]. First, two possibilities of mesh generation were presented and compared. For purely surface tension flows, the polyhedral mesh gave better results. For the case of the pyramidal structures, the edges of the pyramids were significantly smoothed out resulting in an underestimation of the pinning at the edges.

As the flow is nearly exclusively governed by the geometry, the choice of the contact angle model is less important. Pinning occurs *naturally* at the edges and the dynamics are comparable for the dynamic and constant models.

The general comparability between the numerical simulations and the experiments is given, although the sampling technique differs. The pure side view of the experiments *hides* some effects that can be revealed in the numerical simulations. The dynamics after a pinned contact line at

the pyramid's peak are significantly stronger in the numerical simulations than in the experiments. The viscosity in the numerical simulations seems to be underestimated.

The variation of the dip velocity showed no influence to the evolution of the contact line as confirmed by the experiments. Comparing the rise height at the peak to peak line to the dimensionless time (made dimensionless by division with the total time of one cylce) gives identical results.

The variation of the pyramidal sizes shows, that for the smaller pyramids (1 mm and 0.5 mm) the contact line immediately jumps to the next pyramid after the pinning at the lower pyramid whereas for the 2 mm pyramids the contact line approaches the peak due to the liquid rise of the bulk. This can be associated to the meniscus slope. As the contact angle is close to zero, the rise height for this case is smaller than the peak to peak distance for the 2 mm pyramids but greater than for the 1 mm and 0.5 mm pyramids.

The gaps between the pyramids as reported by Manukyan have a strong influence on the outcome of the numerical simulations. The calculations with gap do not match the experiments as good as those without a gap. The valleys lead to a smaller *effective* contact angle and increase the liquid rise. Respecting the gaps increases the effect of pinning at the intersection of the horizontal and vertical valleys. The liquid rise in the valley is then more dependent of the rise at the peaks and the bulk.

This section shows that numerical study of complex pyramidal structures is feasible. It shows that the modeling of the contact angle is less important as the flow is governed by the geometry. Pinning is a matter of the edges (and in this case they a macroscopically visible) and no special treatment is necessary. Manukyan reported a *change of boundary condition*, when the contact line slid along the surface or pinned at the edges. From the author's point of view, this terminology should not be used as there is no change in the boundary condition, but rather in the orientation of the geometry. Manukyan concluded, that it is not possible to formulate a general contact angle boundary condition that is valid for all setups. However, the present thesis shows, that a single simple contact angle boundary condition can describe the presented cases. It is more a matter of the definition of the measured contact angles than the specific contact angle model. In the following chapter, an approach to model complex surface by a boundary condition instead of resolving it is given. It is also based on a constant contact angle model and compares to the

resolved geometries and analytical solutions.

5.6 Modeled Complex Surface

Complex surfaces in numerical simulations have the difficulty of the generation of a suitable mesh as outlined before. Nevertheless, the topology of a surface determines the behavior of the contact line and obviously cannot be neglected. To have both, a reasonable effort for mesh generation and the influence of the topology, the topic of this chapter is to model the geometrical influence of a *complex* surface on a flat wall. Additionally, the following analytical description of the liquid interface at a wall can be used for validation of a numerical method. For a given capillary length and contact angle, the rise height at the wall and the interface shape is known.

5.6.1 Fictitious Contact Angle of a meniscus at a given distance to the wall

The analytical solution of the rise height of a meniscus at a static flat wall is given by [3]

$$h(\theta) = \sqrt{2 \cdot (1 - \sin\theta)}. \tag{5.2}$$

This function can also be inverted to calculate the angle between a vertical line and the meniscus at a given height h. Additionally, Anderson et al. [3] described the shape of the meniscus as:

$$d(h) = \cosh^{-1}\left(\frac{2}{h}\right) - \sqrt{4 - h^2} - \cosh^{-1}\left(\sqrt{2}\right) + \sqrt{2} \tag{5.3}$$

with $d(h)$ the distance of the interface to the wall at the height h and is plotted in Fig. 5.18. The equation is set up such, that the interface at the wall has a height of $h_0 = \sqrt{2}$ where the contact angle is zero and $h = 0$ for $d \to \infty$. The physically meaningful part of the function is for $h < \sqrt{2}$. The variables were non-dimensionlized by the capillary length L_c.

Later it will be necessary to calculate the angle between a vertical line at a given distance d, which means a function $\theta(d)$. As Eq. (5.3) cannot be inverted it has been approximated by

$$d(h) \approx \frac{a}{(h + b) \cdot c} + d \tag{5.4}$$

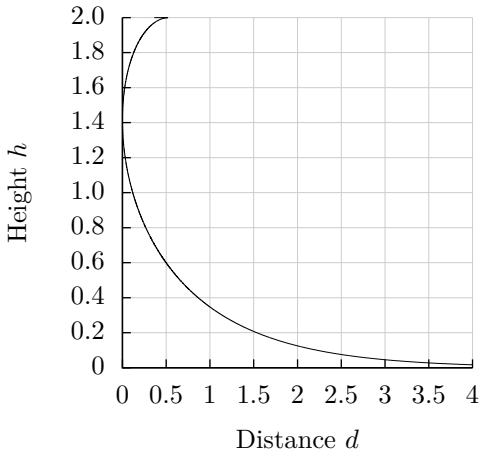

Figure 5.18: The rise height h of a fluid on a flat wall for a given contact angle θ_s.

with

$$\begin{aligned} a &= 1.5 \\ b &= 0.17 \\ c &= 1.9 \\ d &= -0.56. \end{aligned}$$

Now, by inverting Eq. (5.4), the height of the meniscus can be expressed dependent on the distance d and by inserting into Eq. (5.2), the angle at a given distance d can be calculated approximately by

$$\theta\left(h\left(d\right)\right) \approx \arcsin\left(1 - \frac{1}{2}\left(\frac{1.5}{(d+0.56)\cdot 1.9} - 0.17\right)^2\right). \tag{5.5}$$

The analytical and approximated meniscus shapes are plotted in Fig. 5.19. The approximated meniscus shape does not match the analytical solution very close to the wall where the contact angle is zero. As this case is also numerically very difficult, we neglect this shortcoming.

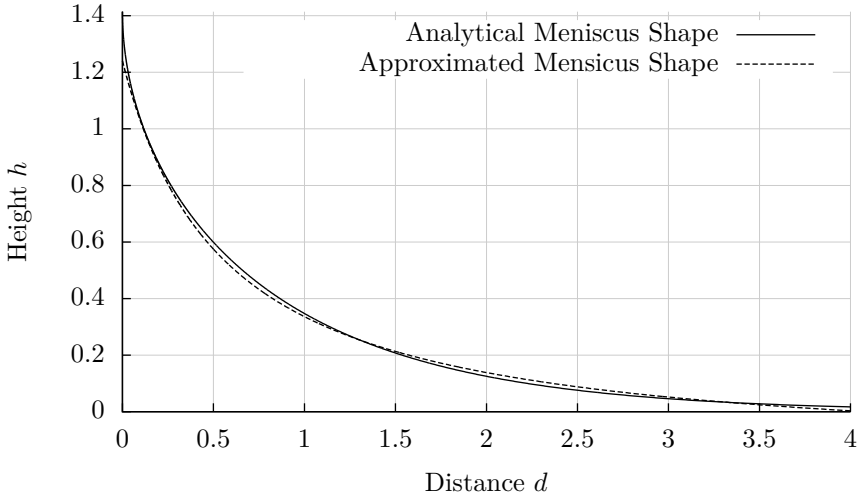

Figure 5.19: The analytical and approximated meniscus shapes.

5.6.2 Groove in a Plate

This chapter comprises a discussion of the evolution of the contact line while transcending a groove in a plate. The contact angle, the contact line movement and pinning will be analyzed. The findings will be compared to a numerical simulation with a resolved groove and the analytic derivation. Afterwards, the groove is modeled by a contact angle boundary condition without resolving the groove by the numerical mesh based on the Eq. (5.2)-(5.3).

The considered geometry and dimensions are given in Fig. 5.20: The depth δ of the groove is 2 mm and the angle of the chamfer is 45°. The vertical segment in the groove is 4 mm long. The probe is assumed to have infinite width.

Fluid is injected from the bottom with a constant velocity $v_{in} = 0.001 ms^{-1}$. Two contact angles are to be considered: First, the contact angle at the wall (θ_s) is assumed to be constant at 45°. Second, the contact angle to the vertical line along the plate (indicated with a red line

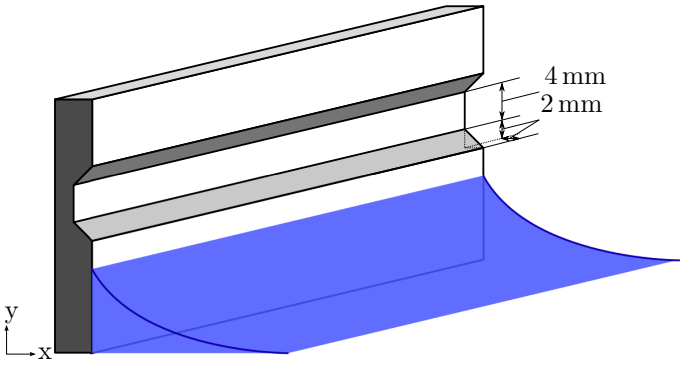

Figure 5.20: The considered geometry has a groove with a depth of 2 mm and the vertical segment in the groove is 4 mm.

in Fig. 5.21) at x_{fw} called θ_{fw}. x_0 is the position of a fictitious wall where the contact angle of the meniscus would be zero if it was extended beyond the wall.

The geometry is divided into 5 regions as depicted in Fig. 5.21 which will be discussed individually:

Region 1 While fluid is injected, the contact line moves along the surface at a constant contact angle $\theta_s = \theta_{\mathrm{fw}} = 45°$. The rise height is constant and can be calculated as $h\,(\theta = 45°)$ using Eq. (5.2). When the contact line approaches the kink to region 2, it will pin. The contact angle will increase until it reaches 90°, corresponding to the opening angle of the groove added to θ_s. The rise height will shrink to zero.

Region 2 In this region, the contact angle will remain constant at $\theta_{\mathrm{fw}} = 90°$. Consequently, the rise height will also remain zero.

Region 3 As soon, as the contact line approaches the kink between region 2 and region 3, the contact line will promptly rise. Thus, the contact angle at x_{fw} will also promptly decrease. The value of θ_{fw} can be determined by the presented equations: First, the distance from x_0 to the actual wall in the groove (x_{w}), where $\theta_s = 45°$ is calculated. Therefore,

$d\,(h\,(\theta = 45°))$ is calculated using the inverse of Eq. (5.2) and Eq. (5.3). Next, the depth of 2 mm is non-dimensionlized by the capillary length and added to the calculated distance of x_{w}. Now the distance of x_{fw} to x_0 is known and the contact angle at x_{fw} can be calculated using Eq. (5.5) giving $\theta_{\mathrm{fw}} = 79.25°$. Similarly, the rise height at x_{fw} can be calculated.

The contact line will move upwards until the kink to region 4 is reached. At this point, the meniscus at x_{fw} is 0.875 mm below this kink calculated by

$$(h\,(\theta = 45°) - h\,(\theta = 79.24°)) \cdot L_c = 0.875\mathrm{mm}. \tag{5.6}$$

Region 4 In this region, the contact line moves along the wall until the kink to region 5 is reached. During the movement, θ_{fw} will constantly decrease until it reaches approximately zero at the kink. The contact angle will then extend back to 45° before it enters region 5.

Region 5 The contact line will propagate constantly over the wall with a constant contact angle of $\theta_{\mathrm{fw}} = \theta_s = 45°$ and a constant rise height.

In short, the evolution of the contact angle is depicted in Fig. 5.21, where

$$\theta_s = 45° \tag{5.7}$$
$$\theta_2 = 90° \tag{5.8}$$
$$\theta_3 = 79.24° \tag{5.9}$$
$$\theta_{min} \approx 0° \tag{5.10}$$
$$\tag{5.11}$$

and the kink in region 3 is expected to be at $y_{\mathrm{m}} = 13.125\mathrm{mm}$.

5.6.2.1 Setup of the Numerical Simulations

In a first numerical simulation, the geometry with the groove is resolved. The fluid parameters correspond to PDMS10cSt as given before. A polyhedral mesh with a cell size of 1×10^{-4} m was created with only a single cell in z-direction, thus treated as a two dimensional case. The contact angle is set to 45° constant at the wall and the inflow velocity at the bottom is $1\,\mathrm{mm\,s^{-1}}$ in y-direction.

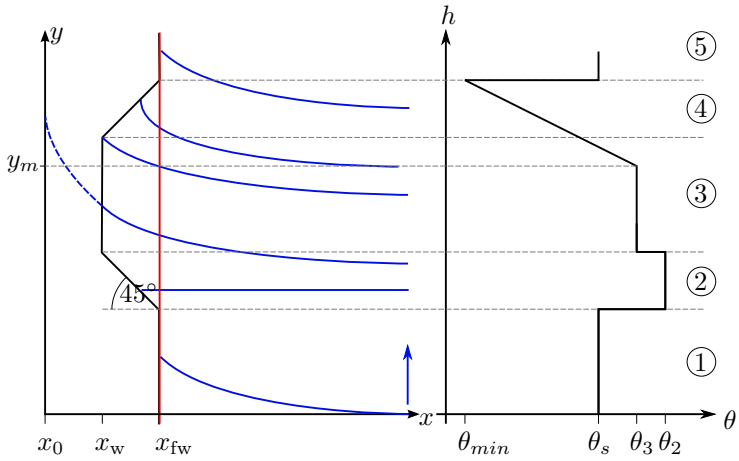

Figure 5.21: Dip coating scenario of a probe with a groove. On the right hand side, the angles between the interface and the vertical red line are given.

Additionally, a simple rectangular domain with a height of 22 mm and a width of 50 mm neglecting the groove is set up using the same mesh type and dimensions as in the case of the resolved groove. However, the contact angle is now prescribed as derived analytically. Thus, the influence of the change of the geometry over the height will be modeled by the change of contact angle at the boundary. Nevertheless, the boundary condition only prescribes a constant contact angle at each cell. No additional treatment for pinning or dynamic behavior are accounted for.

5.6.2.2 Results and Discussion for the Simulated Wetting of a Plate with a Groove

First, the contact angle at x_{fw} is extracted from the numerical simulations. For the case of the resolved groove, this is at $x_{\mathrm{fw}} = 2\mathrm{mm}$. For the modeled groove, this is along the wall, where the contact angle has been prescribed. Both results are plotted along the y-axis together with the analytically derived prediction of the previous chapter in Fig. 5.22.

The agreement is excellent. Both, the predicted contact angles as well as the height in region 3, where the decrease of the contact angle takes place, are correctly predicted on both cases. This also shows, that the

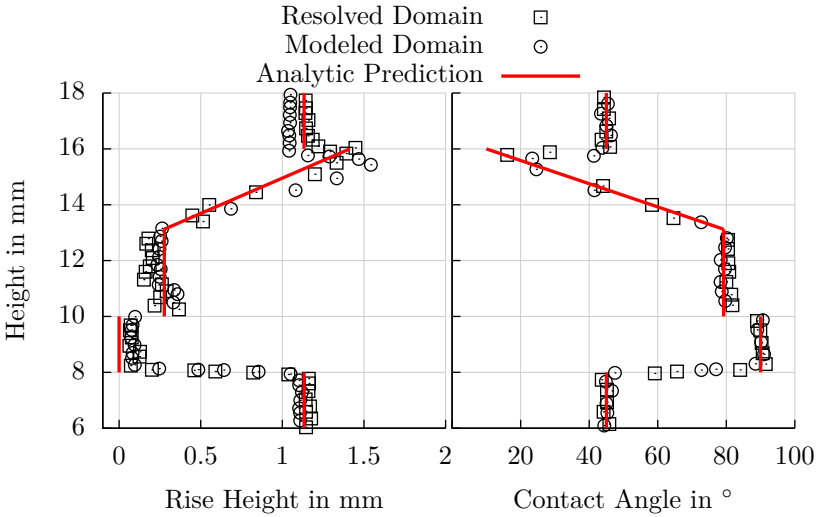

Figure 5.22: The rise height (left) and the contact angle (right) plotted over the height along a vertical line at the wall (indicated by the red line in Fig. 5.21) while overcoming the groove. The angle between the vertical line at x_{fw} as derived in the previous chapter indicated by the red line and the numerical results with a resolved groove and a modeled groove accounted for by the contact angle boundary condition. Similarly the rise heights are compared.

approximated equation for the contact angle as a function of the distance (Eq. (5.5)) gives reasonable results. Only the theoretical 0° at the kink between region 4 and 5 is not captured accurately. In the resolved case, the reason for that is, that the interface spreads slightly over the kink due to the interface thickness. Thus, extracting the contact angle of the reconstructed interface in this region cannot be as exact as along the wall. In the modeled case, a minimum contact angle was set to 15° as a 0° contact angle is difficult to realize numerically.

Additionally, the rise height of the two cases are investigated in Fig. 5.22. The analytically derived behavior is reproduced by both models. The scatter in each of the numerical data is associated to the interpolation technique as the range of scatter is within one computational cell. The comparison between the two approaches is rather good. The mini-

mum rise height of 0 in region 2 is not exactly captured by both models, but is associated to the sampling technique as the visualization shows a perfect horizontal surface in this region (see Fig. 5.23). Differences occur in the temporal evolution of the contact line height, especially after the contact line suddenly increases as it is the case for the transition from region 3 to region 4. The contact line slightly oscillates after the kink which is not completely captured by the modeled groove. For illustration, some snapshots of the two simulations with a reconstructed interface are presented in Fig. 5.23. The snapshots show the two reconstructed interfaces (blue is the modeled groove case, green the resolved). The domain of the modeled groove ends at the red line, whereas the groove can be seen in the resolved case. The pinning occurring at the kinks is *automatically* appearing in both cases as the kink pose an increase of the contact angle. This shows again, that the nature of pinning can be associated to a change in the contact angle, either macroscopically visible as in this case or microscopically as surface roughness.

5.6.3 Modeled Single Pyramid

The same method of a modeled obstacle shall by used for modeling the influence of the pyramids introduced before. In a first step, a single valley of a 2D *pyramid* will be analyzed (see Fig. 5.24). The depth a of the valley is $a = 1.604\text{mm}$ and the distance from peak to peak is $b = 2.208\text{mm}$. The static contact angle θ_s is 48.2° and the inflow velocity is $1\,\text{mm}\,\text{s}^{-1}$. The contact angles along the vertical line at $x_{\text{fw}} = 1.604\text{mm}$ are considered first. In Region 1, where to contact line is below the first kink, the contact angle is the static contact angle $\theta_s = 48.2°$. At the kink, the contact angle increases by the opening angle of the kink which is 55.46°. Thus the resulting contact angle at the kink is 103.66°. Then, the contact line propagates to the valley and the contact angle decreases at x_{fw}. The same equations derived in Sec. 5.6.1 can be used, assuming the meniscus behaves similarly for contact angles greater than 90°. Moreover, one has to have in mind, that the height is now negative, as the equilibrium interface in the far field is higher than the meniscus at the wall. The same has to be respected, when the contact angle is calculated as they now range from 90° to 180°. The contact angle is calculated to $\theta_{\text{fw}} = 95.43°$ when the contact line is close to the valley.

The next region is difficult to capture in the numerical simulations as the contact line snaps over the ascending wall to the upper kink imme-

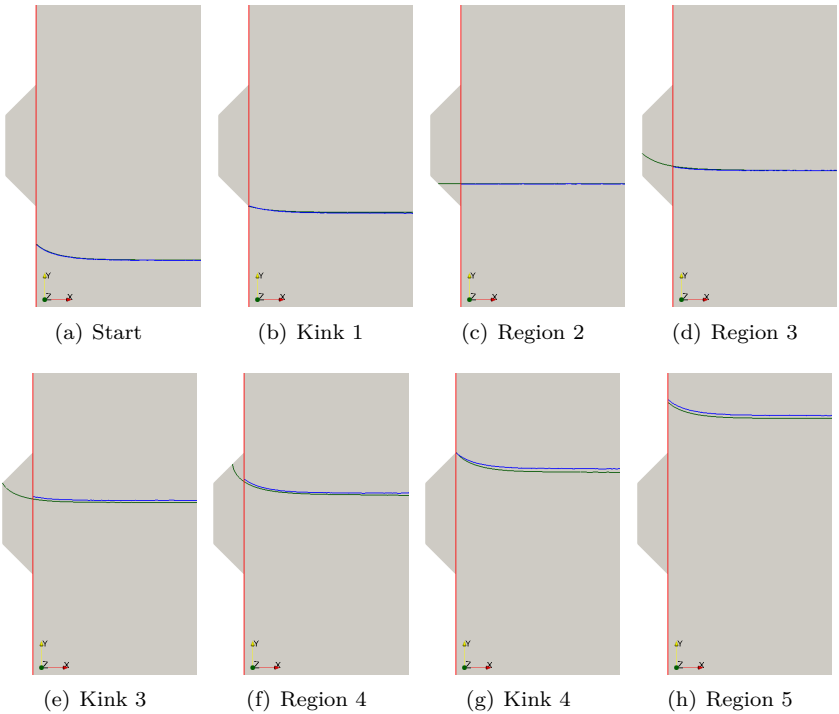

(a) Start (b) Kink 1 (c) Region 2 (d) Region 3

(e) Kink 3 (f) Region 4 (g) Kink 4 (h) Region 5

Figure 5.23: Comparison of the interfaces for the resolved and modeled domain in the different regions and at the kinks. Differences in region 4 (f) and 5 (h) as well as at kink 4 (g) are associated to the dynamics involved due to the sudden change of the contact angle in the resolved domain.

diately, while the meniscus in the far field remains nearly unchanged. Nevertheless, close to the kink, the contact angle will be close to zero and analytically even negative ($-7.26°$). Afterwards, the contact line will remain pinned at the upper kink while the contact angle increases to the static contact angle of 48.2°. Additionally, a difficulty for modeling this geometry is, that for the region at the height of the valley, two contact angles may be found: One, while the contact line is at the lower side and the meniscus at x_{fw} is above the valley, and a second one, when the contact line propagates at the upper wall with an *effective* negative contact

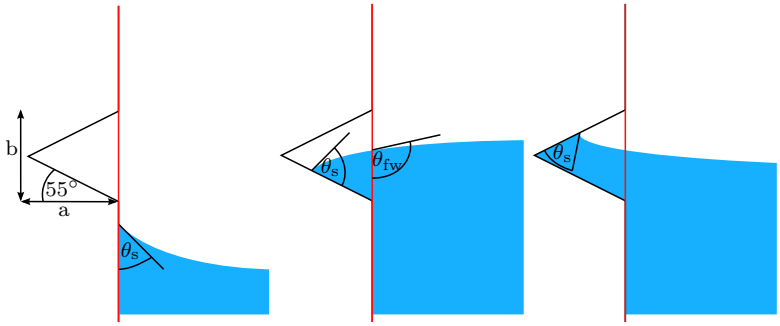

(a) Region 1 (b) Region 2 (c) Region 3

Figure 5.24:

angle and thus, the meniscus falls lower than the meniscus was before.

The described behavior could be verified by a numerical simulation with a single resolved valley (see Fig. 5.25). In order to model the the valley only by the contact angle on a flat wall, the contact angle was chosen such, that the part where the meniscus *jumps* back while overcoming the sharp bend in the valley is neglected. Instead, the contact angle directly changes after the contact line approaches the valley at a height just above 9 mm. The next cell has already a contact angle of about 50°. The minimum contact angle at a height of about 10 mm was set to 20°. The prescribed contact angles over the height are plotted in Fig. 5.25 The extracted contact angles at x_{fw} correspond to the analytical prediction. Thus, the assumptions taken for the contact angles greater than 90° seem to hold.

Comparing the evolution of the rise height while overcoming the valley shows, that although some simplifications where applied, the rise heights agree nicely (Fig. 5.25). Only the mentioned difference, when the contact line snaps to the upper wall is visible at $y \approx 9$mm when in the modeled case, the contact line begins to rise earlier.

5.6.4 Modeled Array of Pyramids

As in the experimental and numerical work shown in Sec. 5.3, an array of pyramids is analyzed next. Again, a two dimensional simplified geometry with four valleys in the same lengths as before are considered. The

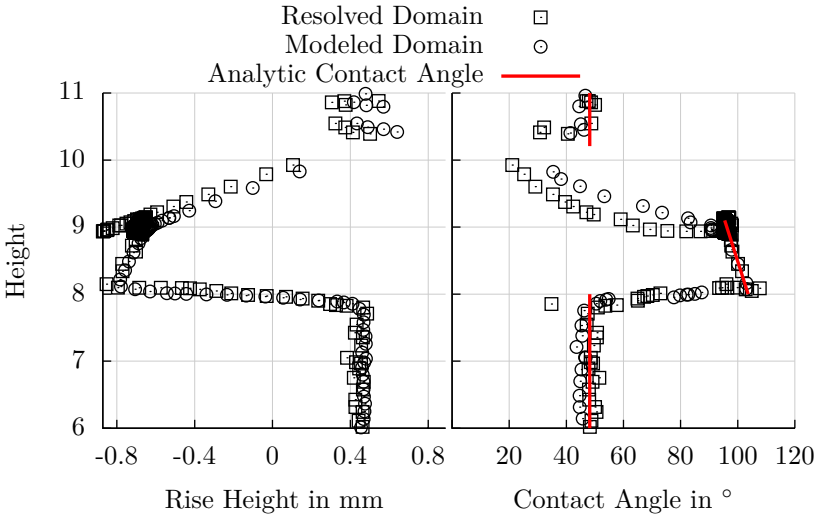

Figure 5.25: The evolution of the rise height (left) and th contact angle (right) while overcoming a valley of a pyramid. The numerical results of the resolved valley correspond to the analytical prediction. Additionally, the results of the modeled case agree nicely to the analytic and resolved cases.

theoretical contact angle along the vertical line at the peaks is basically a sequence of the presented values in Sec. 5.6.3. The rise height and contact angle are compared for the modeled and resolved case in Fig. 5.26. Both, the contact angle as well as the rise height compare nicely for the two setups. The only differences (as in the case for a single valley) are the maximum and minumum contact angles when the contact line suddenly overcomes a kink. Nevertheless, the rise height compares nicely.

5.6.5 Comparison of the Two Dimensional Structures to the Three Dimensional

In this section, the comparability between the simplified two dimensional pyramids to the full three dimensional pyramids of Sec. 5.3 is shown. Therefore, the results of the rise height and the contact angle at the peak to peak lines of the two setups are compared for the 2 mm structures.

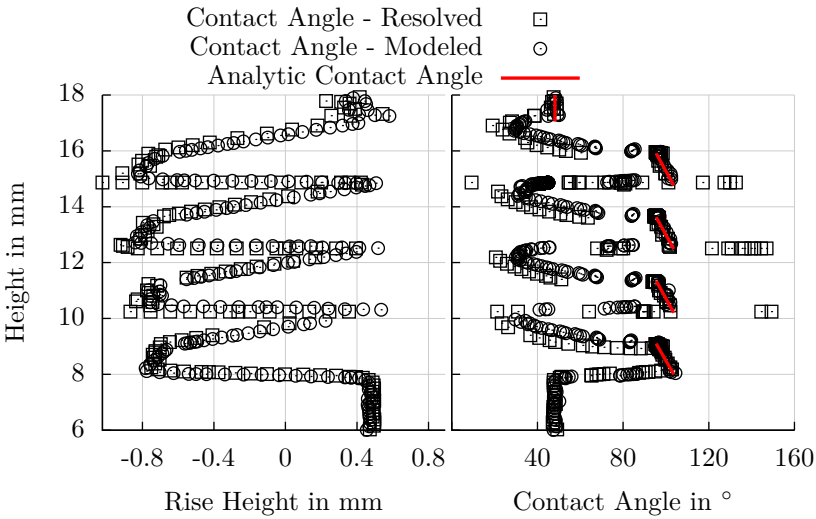

Figure 5.26: The evolution of the rise height (left) and the contact angle (right) of a sequence of valleys. In red, the analytical estimate as described in Sec. 5.6.3 and the squares are the numerical results from a resolved geometry at the vertical line along the peaks.

Fig. 5.27 shows the rise height and contact angle over the height. Regarding the rise height over the height, the general characteristic is well captured by the simplified setup. The occurring differences are associated to the lack of the pre-wetted valleys. Especially for the contact angle, this becomes obvious. After the peak, the contact line combines with the liquid in the valley above the peak. Thus, the contact angle shrinks immediately, but does not experience the strong variation while approaching the valley as in the two-dimensional case. Consequently, the propagation of the contact line is *smoother* in the three-dimensional case which can be seen in the evolution of the rise height.

The simplified two-dimensional setup can be applied to get a rough first estimate about the contact line propagation, but of course is not capable of accounting for the liquid rise in the valleys betweent two pyramids. But comparing the effort to generate a body conformal mesh for the complex geometry and for the post-processing, even a modeled two dimensional setup gives a good estimate about the rise height of the liquid along the

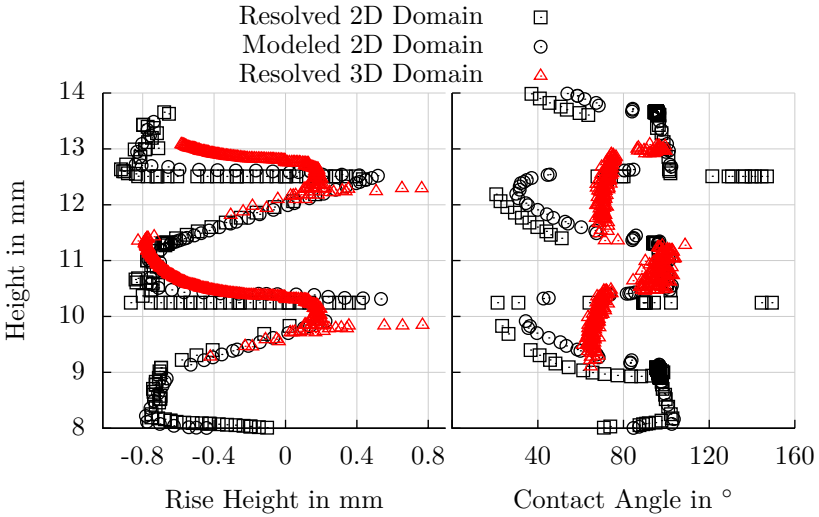

Figure 5.27: The evolution of the rise height and the contact angle in the two and three dimensional setups.

peaks.

5.7 Summary and Conclusion

This chapter gave an overview of the numerical simulations of wetting of complex surfaces. For the fully resolved three dimensional features, the issue of creating a valid, good quality computational mesh is explained. Despite the very good results of the polyhedral mesh cells in the case of a liquid rise on a flat wall, the hex-dominated mesh was used for the numerical studies due to the better resolution of the sharp edges of the pyramids.

The experimental observations were reproduced in the numerical simulations with good agreement. The specific contact angle model was of minor importance for the wetting behavior. A dynamic contact angle model showed similar results to those using a constant contact angle model. In the present case, the flow is nearly exclusively governed by the geometry and the inflow. The observed effects of pinning and slipping is not

a matter of the boundary condition but the edges in the geometry. The experimental findings in the experiments about the influence of the pyramidal size could be numerically reproduced. For small pyramids (1 mm and 0.5 mm) the contact line jumps from peak to peak with only short periods of slippage along the upper side of the pyramids. In the case of 2 mm, the liquid rise is not high enough to wet the complete lower side of the pyramids and thus is also driven by the inflow from below while wetting this face.

The gap in between each pyramid as reported by Manukyan has shown to be a decisive factor for the numerical simulations. In those simulations, were the gaps were respected for as reported, the agreement to the experimental observations is worse than without the gap. The given setup of opening angle of the pyramids and the contact angle would give an theoretical infinite rise of the liquid in the valleys following the derivation of Herminghaus [43]. However, the intersections with the horizontal valleys slow this process down. As the gaps were not intended in the experimental setup and only reported from measurements after the probes were manufactured, their exact shape is not known and therefore difficult to reproduce. For an exact quantification of their influence a more precise and focused study should be performed.

Additionally, an attempt for modeling complex surface has been made. A good quality mesh can be a difficult task for complex geometries. Therefore, for three different two dimensional geometries (a groove in a plate, a single pyramid and an array of pyramids) the contact angle at a given distance to the wall has been analytically calculated. This contact angle has been imposed onto a flat wall as a boundary condition. The results for the evolution of the contact line and the contact angle between for the case of numerical simulations with resolved and modeled geometries and analytical data is excellent. The results have also been compared to the three dimensional setup reported before. It can give a good first estimate of the contact line evolution respecting the effort spent for the setup compared to the three dimensional geometry. Of course it lacks several three dimensional phenomena like the pre-wetting due to the liquid rise in the valleys but can be used to get a first insight.

6 Conclusion

This thesis deals with various applications of wetting scenarios at low Weber numbers. The focus of the work is set on the contact line dynamics, including the (dynamic) contact angle, the contact line propagation as well as its immobility. These effects are first analyzed in geometrically simple cases, where the flow is mainly governed by surface tension. These scenarios are drop wetting and drop on an inclined surface. Next, the complexity of the system is increased by analyzing a drop exposed to shear flow. Finally, the geometrical complexity is extended to wetting of patterned surface by reference to dip coating.

Depending on material properties of the substrate and the liquid, a (constant) advancing and receding contact angle can be determined experimentally, which bound the hysteresis. Within these values, the contact line remains immobile. It is well known from every day life thinking of a drop on a window which does not slide down although gravity *pulls* it downwards.

In the numerical simulations, a given contact angle is realized as a boundary condition for the phase fraction setting its gradient (and consequently the direction of the normal vector of the interface) into a given direction. This direction can either be a constant value or calculated dynamically. This method was implemented and verified for various scenarios previously [6]. If the Weber number gets low, the effect of pinning arises. Numerically, these effects cannot be captured by the described boundary condition. Therefore, an extended (dynamic) contact angle boundary condition has been implemented which is capable of pinning a contact line in the hysteresis and allowing it to propagate if the hysteresis values are exceeded.

In the first scenario of drop wetting, Rioboo et al. [73] reported an immobile contact line at the maximum spread for certain fluid/solid parameters. The numerical simulation of such a case is possible using the new boundary condition. With a pure gradient boundary condition, the contact line is not immobile within the hysteresis and the observed pinning

after the maximum spread cannot be reproduced numerically.

The critical inclination angle of a solid substrate at which a drop starts to slide can also be predicted correctly with the new boundary condition. If the pure gradient boundary condition is applied, the drop starts to move even on horizontal surfaces.

The same is true for a drop exposed to shear flow which has been assessed experimentally and numerically. The code is able to predict a critical inflow velocity at which a drop starts to move on different substrates (with different hysteresis values). Again, without the extension of the boundary condition, the drop slides immediately after the inflow is activated. The numerical results agreed very well with the experimental data.

In the next scenario, the focus was set on the geometrical complexity of the substrate. Therefore, the experimental data of dip coating of complex surfaces provided by Manukyan [61] set the basis of the numerical investigations. First, dip coating scenarios has been simplified and numerically analyzed for a flat, static wall comparing the numerical results to analytic data. It reveals, that polyhedral mesh cells significantly improve the results for pure surface tension driven calculations.

Next, two tools to mesh complex geometries are compared. The generation of body fitted meshes using polyhedral mesh cells with gmsh and polyDualMesh is compared to hex-dominated mesh generated with snappyHexMesh. For the case of the complex surfaces, where the flow is exclusively governed by the geometry, the mesh type is of minor importance but the correct reproduction of sharp corners is essential. The generation of meshes with hex-dominnated cells using snappyHexMesh generated sharper edges and was therefore chosen for the numerical simulations. Moreover, in these cases, the contact angle model is negligible. Both pinning and its dynamic behavior are prescribed by the geometry. Thus, for the parameter studies as done experimentally, a constant contact angle model as well as a hex-dominated mesh were used due to the less computational costs as well as the ease of mesh generation.

The simulations of the complex geometries reproduced the experimental findings well. The effect of different parameters like pyramidal size, dip velocity and liquid properties compared to the experiments. However, the reported gap in between the pyramids was one of the main reasons for disagreement between the numerical and expermiantal findings. Its size and thus the distance in between the inlined sides of the pyramids is

a main factor for the liquid rise and the prewetting of the valleys. When set up as reported from the measurements of the manufactured probes, the liquid rise was underestimated. When neglected and calculated with the pyramids abreast to each other, the comparison to the experiments is improved.

In the last part, the possibility of simplifying the geometrical complex surfaces is addressed. This is done by accounting for geometrical changes of the substrate only by a change of the boundary condition at a flat wall. In this spirit, a groove in a wall has been successfully modeled only by a contact angle boundary condition showing very good agreement between the resolved and modeled case as well as to analytical results. This technique has also been applied to the modeling of the pyramidal features as introduced before also with good agreement.

To sum up, the work can be split up into to branches. The first one is the simulation of contact line phenomena at low Weber numbers on flat, real surfaces. The effect of pinning cannot be neglected and has to be accounted for to get reasonable results. As the numerical meshes are perfectly smooth, the real roughness of a surface is lost, leading to deficits in the numerical handling. In the second branch, geometrical complex surfaces have been analyzed where the flow is nearly completely controlled by the macroscopic *obstacles*. In these cases, the pinning at the kinks and the change of the apparent contact angle are subjected to the geometry and a specific model is not necessary. If the contact line has to overcome a (macroscopic) kink, this can be only achieved by increasing the contact angle while the contact line is immobile - which is exactly the reason of pinning on the microscopic scales introduced by surface roughness.

A Appendix

A.1 Capillary Rise for Polyhedral and Hexaedral Meshes

The two mesh-types, hexaedral and polyhedral, are compared against each other for the case of a static flat wall with a constant static contact angle. The rise height h of the meniscus for a given contact angle θ_s can be derived from the Young-Laplace equation [3] and expressed as

$$h = \sqrt{2\,(1 - \sin\theta)}, \tag{A.1}$$

illustrated in Fig. A.1. The quantities in this equation are nondimensionlized using the Capillary length.

A.1.1 Numerical Setup

The computational domain measures a height of 8 mm and a width of 10 mm. The cases were performed on both, two- and three-dimensional setup. In the three-dimensional case, the depth is 2 mm. The static contact angle θ_s is modeled with a constant contact angle model boundary condition and a value of 42.8°. As fluid, PDMS10cSt was chosen (Tab. 5.2). The theoretical rise height h calculated by Eq. (A.1) is 1.48 mm.

The edge length of the finest cells at the wall are refined in four steps from 9.3×10^{-5} m to 3.4×10^{-5} m on the hexaedral mesh and from 10.0×10^{-5} m to 4×10^{-5} m on the polyhedral mesh. The corresponding number of control volumes is presented in Tab. A.1.

Figure A.2 shows the rise height of the free surface for different mesh resolutions. The parameters of each of the four cases are summarized in Table A.1.

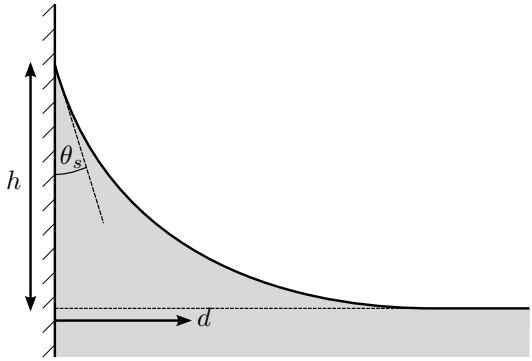

Figure A.1: The rise height h of a fluid on a flat wall for a given contact angle θ_s.

Table A.1: Numerical parameters for the case of the calculation of the rise height on different meshes.

Mesh type	Cell edge length	No. CV
Hex	9.3×10^{-5} m	63 300
Hex	6.9×10^{-5} m	150 000
Hex	4.6×10^{-5} m	506 300
Hex	3.4×10^{-5} m	1 200 100
Poly	10.0×10^{-5} m	23 900
Poly	7.0×10^{-5} m	63 900
Poly	5.0×10^{-5} m	164 700
Poly	4.0×10^{-5} m	331 000

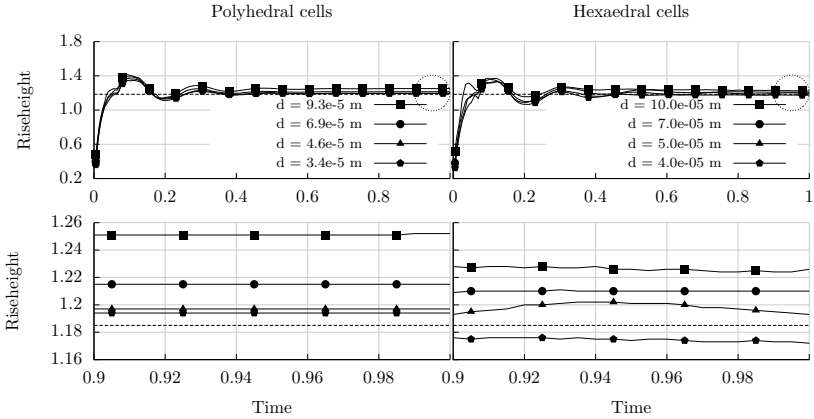

Figure A.2: The rise height of the contact line for a given contact angle compared on a hexaedral and polyhedral mesh on different mesh resolutions. The theoretical rise height calculated by Eq. (A.1) is drawn with a dashed line.

A.1.2 Results for the Rise Height on a Flat Wall

The results of the numerical calculation of the rise height is given in Fig. A.2. It shows the height of the reconstructed interface over the time at the flat wall. The the non-convergent rise height for the hexaedral as reported by Afkhami et al. [1] is confirmed. Using polyhedral cells and the same constant contact angle boundary condition delivers a solution converging to the analytical result without any further contact angle modeling. Moreover, the contact line position is more stable for the polyhedral mesh. The computational time is for each refinement level in a similar range.

Bibliography

[1] S. Afkhami, S. Zaleski, and M. Bussmann. A mesh-dependent model for applying dynamic contact angles to VOF simulations. *J. Comput. Phys.*, 228:5370–5389, 2009.

[2] M. P. Allen and D. J. Tildesley. *Computer Simulation of Liquids.* Oxford University Press, Oxford, 1989.

[3] M. L. Anderson, A. P. Bassom, and N. Fowkes. Exact solution of the laplace-young equation. *Proc. R. Soc. A*, 462:3645–3656, 2006.

[4] H. Bankreira and O. Cohu. Direct forward gravure coating on unsupported web. *Chem. Eng. Sci.*, 53(6):1223–1231, 1997.

[5] K. J. Bathe. *Finite Element Procedures.* Prentice Hall, 1996.

[6] E. Berberovic. *Investigation of Free-surface Flow Associated with Drop Impact: Numerical Simulations and Theoretical Modeling.* PhD thesis, Technische Universität Darmstadt, 2010.

[7] E. Berberović, N. P. v. Hinsberg, S. Jakirlić, I. Roisman, and C. Tropea. Drop impact onto a liquid layer of finite thickness: Dynamics of the cavity evolution. *Phys. Rev. E*, 79:036306, 2009.

[8] M. Bertagnolli, M. Marchese, and G. Jacucci. Modeling of particles impacting on a rigid substrate under plasma spraying conditions. *J. Therm. Spray. Techn.*, 4(1):41–49, 1995.

[9] T. D. Blake. The physics of moving wetting lines. *J. Colloid Interf. Sci.*, 299:1–13, 2006.

[10] D. Bonn, J. Eggers, J. Indekeu, J. Meunier, and E. Rolley. Wetting and spreading. *Rev. Mod. Phys.*, 81(2):739 – 805, 2009.

[11] A. Boudaoud. Non-Newtonian thin films with normal stresses: dynamics and spreading. *Eur. Phys. J. E*, 22:107, 2007.

[12] J. U. Brackbill, D. B. Kothe, and C. Zemach. A continuum method for modeling surface tension. *J. Comput. Phys.*, 100(2):335–354, 1992.

[13] F. Brochard-Wyart and P. G. de Gennes. Dynamics of partial wetting. *Adv. Colloid Interface Sci.*, 39:1–11, 1992.

[14] H. Bruus. Theoretical microfluidics. lecture note, 2006.

[15] A. B. D. Cassie and S. Baxter. Wettability of porous surfaces. *Trans. Faraday Soc.*, 40:546–551, 1944.

[16] S. Chen and G. D. Doolean. Lattice Boltzmann method for fluid flows. *Annu. Rev. Fluid Mech.*, 30:329–364, 1998.

[17] D. S. Clague, B. D. Kandhai, R. Zhang, and P. M. A. Sloot. Hydraulic permeability of (un)bounded fibrous media using the lattice boltzmann method. *Phys. Rev. E*, 61:616–625, Jan 2000.

[18] K. Connington and T. Lee. Lattice boltzmann simulations of forced wetting transitions of drops on superhydrophobic surfaces. *J. Comput. Phys.*, 250:601–615, 2013.

[19] R. G. Cox. The dynamics of the spreading of liquids on a solid surface. part 1. viscous flow. *J. Fluid Mech.*, 168:169–194, 1986.

[20] R. G. Cox. The dynamics of the spreading of liquids on a solid surface. Part 1. Viscous flow. *J. Fluid Mech.*, 168:169 – 194, 1986.

[21] S. M. Dámian. *An Extended Mixture Model for the Simultaneous Treatment of Short and Long Scale Interfaces*. PhD thesis, Universidad Nacional del Litoral, Santa Fe, Argentina, 2013.

[22] A. A. Darhuber, S. M. Troian, J. M. Davis, and S. M. Miller. Selective dip-coating of chemically micropatterned surfaces. *J. Appl. Phys.*, 88(9):5119–5126, 2000.

[23] P. G. de Gennes. Wetting: statics and dynamics. *Rev. Mod. Phys.*, 57(3):827–863, 1985.

[24] M. J. de Ruijter, J. D. Coninck, and G. Oshanin. Droplet spreading: Partial wetting regime revisited. *Langmuir*, 15:2209, 1999.

[25] B. M. Deryagin and S. M. Levi. *Film Coating Theory*. New York Focal Press, 1964.

[26] S. S. Deshpande, L. Anumolu, and M. F. Trujillo. Evaluating the performance of the two-phase flow solver interfoam. *Comput. Sci. Disc.*, 5(014016), 2012.

[27] P. Dimitrakopoulos and J. J. L. Higdon. Displacement of fluid droplets from solid surfaces in low-reynolds-number shear flows. *J. Fluid. Mech.*, 336:351–378, 1997.

[28] H. Ding and P. D. M. Spelt. Onset of motion of a 3d droplet on a wall in shear flow at moderate reynolds numbers. *J. Fluid Mech.*, 599:341–362, 2008.

[29] J.-B. Dupont and D. Legendre. Numerical simulation of static and sliding drop with contact angle hysteresis. *J. Comput. Phys.*, 229(7):2453–2478, Apr. 2010.

[30] C. Duquennoy, O. Lebaigue, and J. Magnaudet. A numerical model of gas-liquid-solid contact line. *Fluid Mec. A*, 62:89–98, 2001.

[31] E. B. Dussan and S. H. Davis. On the motion of a fluid-fluid interface along a solid surface. *J. Fluid Mech.*, 65(01):71–95, 1974.

[32] E. B. Dussan V. The moving contact line: the slip boundary condition. *J. Fluid Mech.*, 77(4):665–684, 1976.

[33] E. B. Dussan V. and R. T.-P. Chow. On the ability of drops or bubbles to stick to non-horizontal surfaces of solids. *J. Fluid Mech.*, 137:1–29, 1983.

[34] M. H. Eres, L. W. Schwartz, and R. V. Roy. Fingering phenomena for driven coating films. *Phys. Fluids*, 12:1278, 2000.

[35] C. W. Extrand. Contact angles and hysteresis on surfaces with chemically heterogeneous islands. *Langmuir*, 19(9):3793–3796, 2003.

[36] J. H. Ferziger and M. Peric. *Computational Methods for Fluid Dynamics*. Springer, Berlin, 2002.

[37] J. Fukai, Z. Zhao, D. Poulikakos, C. M. Megaridis, and O. Miyatake. Modeling of the deformation of a liquid droplet impinging upon a flat surface. *Phys. Fluids*, A 5:2588–2599, 1993.

[38] L. Gao and T. J. McCarthy. How Wenzel and Cassie were wrong. *Langmuir*, 23(7):3762–3765, 2007.

[39] P. Gaskell and A. Lau. Curvature-compensated convective transport: Smart, a new boundedness-preserving transport algorithm. *Int. J. Num. Meth. Fluids*, 8:617–641, 1988.

[40] P.-L. George and P. Frey. *Mesh generation.* Hermes, Lyon, 2000.

[41] C. Geuzaine and J.-F. Remacle. Gmsh: a three-dimensional finite element mesh generator with built-in pre- and post-processing facilities. *Int. J. Numer. Meth. Eng.*, 79(11):1309–1331, 2009.

[42] I. Hadzic and K. Hanjalic. Separation-induced transition to turbulence: Second-moment closure modelling. *Flow, Turbul. and Combust.*, 63:153–173, 1999.

[43] S. Herminghaus, M. Brinkmann, and R. Seemann. Wetting and dewetting of complex surface geometries. *Annu. Rev. Mater. Res.*, 38:101–121, 2008.

[44] H. Hervet and P.-G. de Gennes. The dynamics of wetting: Precursor films in the wetting of "dry" solids. *C. R. Acad. Sci., Ser. II: Mec., Phys., Chim., Sci.*, 299:499, 1984.

[45] C. W. Hirt and B. D. Nichols. Volume of fluid (vof) method for the dynamics of free boundaries. *J. Comput. Phys.*, 39:201–225, 1981.

[46] L. M. Hocking. A moving fluid interface on a rough surface. *J. Fluid Mech.*, 76:209, 1976.

[47] L. M. Hocking. A moving fluid interface. part 2. the removal of the force singularity by a slip flow. *J. Fluid Mech.*, 79(2):209–229, 1977.

[48] S. R. Hodges and O. E. Jensen. Spreading and peeling dynamics in a model of cell adhesion. *J. Fluid. Mech.*, 460:381–409, 2002.

[49] R. L. Hoffman. A study of the advancing interface, part i: Interface shape in liquid-gas systems. *J. Colloid Interf. Sci.*, 50:228–241, 1975.

[50] H. Hu, S. Huang, and L. Chen. Displacement of liquid droplets on micro-grooved surfaces with air flow. *Exp. Therm. Fluid Sci.*, 49:86–93, 2013.

[51] C. Huh and L. E. Scriven. Hydrodynamic model of steady movement of a solid/liquid/fluid contact line. *J. Colloid Interf. Sci.*, 35:85–101, 1970.

[52] R. Issa. Solution of the implicitly discretised fluid flow equations by operator-splitting. *J. Comput. Phys.*, 62(1):40 – 65, 1986.

[53] H. Jasak. *Error analysis and estimation in the Finite Volume method with applications to fluid flows.* PhD thesis, Imperial College, University of London, 1996.

[54] K. Jiao, B. Zhou, and P. Quan. Liquid water transport in parallel serpentine channels with manifolds on cathode side of a pem fuel cell stack. *J. Power Sources*, 154:124–137, 2006.

[55] S. F. Kistler. Hydrodynamics of wetting. In J. C. Berg, editor, *Wettability*, pages 311–429. Marcel Dekker, New York, 1993.

[56] D. B. Kothe. Perspective on eulerian finite volume methods for incompressible interfacial flows. In *Kuhlmann and H Rath*, pages 267–331. Springer, 1999.

[57] L. Landau and B. Levich. *Acta Pysicochim URSS*, 17:4 – 54, 1942.

[58] B. P. Leonard. Simple high-accuracy resolution program for convective modeling of discontinuities. *Int. J. Num. Meth. Fluids*, 8:1291–1318, 1988.

[59] R. Lipowsky, P. Lenz, and P. D. Swain. Wetting and dewetting of structured and imprinted surfaces. *Colloids Surf.*, 161:3–22, 2000.

[60] M. Mahe, M. Vignes-Adler, and P. M. J. Adler. Adhesion of droplets on a solid wall and detachment by a shear flow. *J. Colloid Interf. Sci.*, 126:329–336, 1988.

[61] S. Manukyan. *Fundamental Investigation of Forced Wetting on Structured Surfaces.* PhD thesis, TU Darmstadt, Darmstadt, 2013.

[62] H. Marschall. *Towards the Numerical Simulation of Multi-Scale Two-Phase Flows.* PhD thesis, Technische Universität München, Lehrstuhl für Technische Chemie, 2011.

[63] N. S. Martys and H. Chen. Simulation of multicomponent fluids in complex three-dimensional geometries by the lattice boltzmann method. *Phys. Rev. E: Stat. Phys., Plasmas, Fluids*, 53(1):743–750, 1996.

[64] M. Mastrangeli, W. Ruythooren, C. Van Hoof, and J.-P. Celis. Conformal dip-coating of patterned surfaces for capillary die-to-substrate self-assembly. *J. Micromech. Microeng.*, 19(045015), 2009.

[65] A. J. B. Milne and A. Amirfazli. Drop shedding by shear flow for hydrophilic to superhydrophobic surfaces. *Langmuir*, 25:14155–14164, 2009.

[66] H. K. Moffat. Viscous and resistive eddies near a sharp corner. *J. Fluid Mech.*, 18:1 – 18, 1964.

[67] S. Muzaferija, M. Peric, P. Sames, and T. Schelin. A two-fluid navier-stokes solver to simulate water entry. *Twenty-Second Symposium on Naval Hydrodynamics*, 1998.

[68] S. Osher and R. Fedkiw. *Level Set Methods and Dynamic Implicit Surfaces*. Springer, New York, 2003.

[69] S. Patankar. *Numerical Heat Transfer and Fluid Flow*. Series in computational methods in mechanics and thermal sciences. Taylor & Francis, 1980.

[70] P. G. Petrov and J. G. Petrov. A combined melcular-hydrodynamic approach to wetting kinetics. *Langmuir*, 8:1762–1767, 1992.

[71] E. Pierce, F. J. Carmona, and A. Amirfazli. Understanding of sliding and contact angle results in tilted plate experiments. *Colloid Surface A*, 323:73–82, 2007.

[72] S. Rebay. Efficient unstructured mesh generation by means of delaunay triangulation and Bowyer-Watson algorithm. *J. Comput. Phys.*, 106:25–138, 1993.

[73] R. Rioboo, M. Marengo, and C. Tropea. Time evolution of liquid drop impact onto solid dry surfaces. *Exp. Fluids*, 33:112–124, 2002.

[74] I. V. Roisman, L. Opfer, C. Tropea, and M. Raessi. Drop impact onto a dry surface: Role of the dynamic contact angle. *Colloid Surface A*, 322(1-3):183 – 191, 2008.

[75] H. Rusche. *Computational Fluid Dynamics of Dispersed Two-Phase Flows at High Phase Fractions*. PhD thesis, Imperial College, University of London, 2002.

[76] Y. Saad. Iterative methods for sparse linear systems. *Society for Industrial and Applied Mathematics*, Second Edition, 2003.

[77] A. A. Saha and S. K. Mitra. Effect of dynamic contact angle in a volume of fluid (vof) model for a microfluidic capillary flow. *J. Colloid Interf. Sci.*, 339:461–480, 2009.

[78] E. Savory and N. Toy. Hemisphere and hemisphere-cylinders in turbulent boundary layers. *J. Wind Eng. Ind. Aerod.*, 32:345, 1986.

[79] M. Sbragaglia, R. Benzi, L. Biferale, S. Succi, and F. Toschi. Surface roughness-hydrophobicity coupling in microchannel and nanochannel flows. *Phys. Rev. E: Stat. Phys., Plasmas, Fluids*, 97(204503), 2006.

[80] P. Seppecher. Moving contact lines in the cahn-hilliard theory. *Int. J. Eng. Sci.*, 34:977, 1996.

[81] M. E. R. Shanahan and K. Sefiane. Kinetics of Triple Line Motion during Evaporation. In K. L. Mittal, editor, *Contact Angle, Wettability and Adhesion*, pages 19–31. Koninklijke Bril, Leiden, 2009.

[82] Y. D. Shikhmurzaev. Moving contact lines in liquid/liquid/solid systems. *J. Multiphase Flow*, 19(4):589–610, 1993.

[83] Y. D. Shikhmurzaev. Moving contact lines in liquid/liquid/solid systems. *J. Fluid Mech.*, 334:211–249, 1997.

[84] Y. D. Shikhmurzaev. *Capillary Flows with Forming Interfaces.* Chapman and Hall, CRC, Birmingham, 2007.

[85] E. Shirani and S. Masoomi. Deformation of a droplet in a channel flow. *J. Fuel Cell Sci. Tech.*, 5(4):041008, 2008.

[86] P. D. M. Spelt. A level-set approach for simulations of flows with multiple moving contact lines with hysteresis. *Journal of Computational Physics*, 207:389–404, 2005.

[87] K. Sugiyama and M. Sbragaglia. Linear shear flow past a hemispherical droplet adhering to a solid surface. *J. Eng. Math.*, 04:3, 2007.

[88] Y. Sui, H. Ding, and P. D. M. Spelt. Numerical simulations of flows with moving contact lines. *Annu. Rev. Fluid Mech.*, 46:46–119, 2014.

[89] M. Sussman, P. Smereka, and P. Osher. A level set approach for computing solutions to incompressible two-phase flow. *J. Comput. Phys.*, 114(1):146 – 159, 1994.

[90] L. H. Tanner. The spreading of silicone oil drop on horizontal surfaces. *J. Phys. D*, 12:1473–1484, 1979.

[91] A. Theodorakakos, T. Ous, M. Gavaises, J. M. Nouri, N. Nikolopoulos, and H. Yanagihara. Dynamics of water droplets detached from porous surfaces of relevance to pem fuel cells. *J. Colloid Interf. Sci.*, 300:673–687, 2006.

[92] V. Thoreau, B. Malki, G. Berthome, L. Boulange-Petermann, and J. C. Joud. Physico-chemical and dynamic study of oil-drop removal from bare and coated stainless-steel surfaces. *J. Adhes. Sci. Technol.*, 20:1819–1831, 2006.

[93] O. Ubbink and R. I. Issa. A method for capturing sharp fluid interfaces on arbitrary meshes. *J. Comp. Phys.*, 153(1):26–50, 1999.

[94] O. V. Voinov. Hydrodynamics of wetting. *Fluid Dyn.*, 11(5):714, 1976.

[95] L. Wang, H. Huang, and X.-Y. Lu. Scheme for contact angle and its hysteresis in a multiphase lattice boltzmann method. *Phys. Rev.*, E 87:013301, 2013.

[96] P. C. Wayner. Spreading of a liquid film with a finite contact angle by the evaporation/condensation process. *Langmuir*, 9:294, 1993.

[97] D. E. Weidner and L. W. Schwartz. Contact-line motion of shear-thinning liquids. *Phys. Fluids*, 6:3535, 1994.

[98] H. Weller. A new approach to VOF-based interface capturing methods for incompressible and compressible flow. Technical report, OpenCFD, 2006.

[99] R. N. Wenzel. Wettability of porous surfaces. *Ind. Eng. Chem.*, 28:988–994, 1936.

[100] K. Yokoi, D. Vadillo, J. Hinch, and I. Hutchings. Numerical studies of the influence of the dynamic contact angle on a droplet impacting on a dry surface. *Phys. Fluids*, 21:072102, 2009.

List of Figures

1.1 Displacement of a small area of the interface. Redrawn from [14]. 4
1.2 Illustration of Young's equation for the contact angle in equilibrium state. 6
1.3 Navier-slip model with *slip length* λ 9
1.4 Contact angles on different scales (redrawn from [10]) . . 10
1.5 Experiment to determine the advancing and receding contact angle 12
1.6 The apparent contact angle of a solid, liquid and gas system can differ due to surface roughness. The dashed line represent a macroscopic horizontal surface against which the apparent contact angles are measured. The *real* surface is not resolved. 13
1.7 The contact angle hysteresis: The contact angle θ changes dynamically depending on the capillary number in advancing and receding phase. The hysteresis, where the contact line is immobile, is bounded by the advancing and receding contact angle θ_a and θ_r. 14
1.8 Sketch of a possible relation of the drop volume and its radius for the experiment given in Fig. 1.5 to describe the hysteresis behavior. 15

2.1 Polyhedral Control Volume 21
2.2 Combined UD and CD schemes 25
2.3 Correction of the non-orthogonal contribution 27
2.4 Sketch of the velocity vectors at the liquid interface and the propagation velocity of the contact line. 39
2.5 Right-hand-side of Eq. (2.64). The correct contact line velocity is only predicted near $\theta \approx \pi/2$. 39

3.1 Results of the numerical simulation of a drop impact onto smooth PVC. As in the experimental results, using the pinning boundary condition, the drop diameter remains constant after the maximum spread. The pure dynamic contact angle boundary condition does not show any pinning of the contact line. 46

3.2 Results of the numerical simulation of drop wetting on smooth PVC using the pinning BC and the *conventional* dynamic contact angle BC. The upper plot shows the contact angle and the drop diameter. The hysteresis band is indicated with the solid horizontal line. The lower plot shows the contact line velocity being zero, while the contact angle is within the hysteresis if the pinning BC is applied. The contact line velocity for the case of the conventional dyn. contact angle BC is non-zero all the time. Additionally, the contact angle does not tend to the receding contact angle. 48

3.3 Simulation of a 2D drop on solid substrate which is inclined over time on different mesh resolutions. The plot shows the position of the contact line of the front ($\mathbf{x}_f$) and back ($\mathbf{x}_b$) against the inclination angle of the substrate. The rotation velocity is $5.625\,^\circ\,\mathrm{s}^{-1}$, $\theta_A = 100^\circ$, $\theta_R = 80^\circ$ and $\sigma = 0.036$. 51

3.4 Simulation of a drop in a plate which is inclined with different angular velocities. The plot shows the position of the front ($\mathbf{x}_f$) and rear ($\mathbf{x}_b$) contact line against the inclination angle. The angular velocity does not influence the point of incipient motion. 52

3.5 Initial drop shape for an initial contact angle of 60° (a) and 120° (b). The influence of the initial shape to the critical inclination angle is studied in Fig. 3.6. 53

3.6 The plot shows the backmost and frontmost contact line position of a drop on horizontal surface which is gradually inclined. It compares different initial drop shapes (see Fig. 3.5). The initial shape has no significant influence on the critical inclination angle, as expected. 54

3.7 Numerical prediction of the critical inclination angle compared to the analytical prediction for different hysteresis values and surface tensions. The parameters can be found in Table 3.2. 56

4.1 Schematic setup of the wind tunnel for experiments. . . . 58
4.2 Illustration of the computational domain. The length L of the plate is 120 mm, its depth D values 80 mm with a height H of 12 mm. The drop is placed 40 mm behind the tip of the plate. x_b and x_f are the distance between the tip of the plate and the back and front of the drop respectively. 59
4.3 Comparison of the position of the frontal and rear contact points at various crossflow velocities and onset of the incipient motion on the three substrates. The corresponding critical velocity measured in the experiments is indicated by a vertical line. 61
4.4 Comparison of the drop deformation at the initial stage ($v_{in} = 0$) and just before the drop starts to move (incipient motion $v_{in} = v_{crit}$) for the three different substrates. . . . 63

5.1 An overview of the pyramidal substrate (a) and the definition of the parameters (b). 67
5.2 Experimental setup for dip coating experiments taken from [61]. 68
5.3 Overview of the computational domain with the refinement areas towards the structured surface. The computational domain exploits two symmetries, one along the peaks of the pyramids, the second along the vertical valley. 69
5.4 Visualization of the workflow of `snappyHexMesh` for the pyramidal structures. 71
5.5 Visualization of the workflow of `gmsh` with `polyDualMesh` for the pyramidal structures. 73
5.6 Smoothing of the sharp edges in the polyhedral (a) and hex-dominated (b) meshes. 74
5.7 Three selected stages while the liquid wets a pyramid. . . 76
5.8 Comparison of a polyhedral and hex-dominated mesh for the rise height (left) and the contact angle (right) along the peak to peak line. 77
5.9 Comparison of two contact angle models (constant and dynamic) for the numerical results of the rise height (left) and the contact angle (right) along the peak to peak line. The contact angle model has no significant influence. 78
5.10 A typical picture taken in the experiments and the extracted quantities. 79

5.11 Comparison of the experimental against numerical results for the rise height at the peak line and 3 mm away from the wall. 80

5.12 Comparison of the three different dip-velocities ($0.848\,\mathrm{mm\,s^{-1}}$, $0.636\,\mathrm{mm\,s^{-1}}$ and $0.424\,\mathrm{mm\,s^{-1}}$) for the 2 mm pyramidal structures. The dip-velocity has no influence on the evolution of the contact line. 81

5.13 Temporal evolution ($\Delta t = 0.0125s$) of the Interface along the pyramids. Only for the 2 mm pyramids, the contact line remains at the lower side of the pyramid and is approaching the peak by the immersion of the substrate. 82

5.14 Comparison of two different liquids (PDMS 10cSt and PDMS 100cSt) with a dip-velocity of $0.848\,\mathrm{mm\,s^{-1}}$ in 2 mm pyramids. The general behavior is very similar, however the strong oscillations in the beginning do not appear for the viscous PDMS 100cSt. 83

5.15 The numerical mesh at the intersections of the valleys without a gap (a) and with the reported gap (b). 84

5.16 The slope of the liquid interface with slope angle β in a wedge is solely governed by the contact angle θ and the opening angle ψ 85

5.17 Comparison of the rise height in the vertical valleys for the 2 mm pyramids with and without a gap. The liquid rise is much higher without the gaps. 86

5.18 The rise height h of a fluid on a flat wall for a given contact angle θ_s. 89

5.19 The analytical and approximated meniscus shapes. 90

5.20 The considered geometry has a groove with a depth of 2 mm and the vertical segment in the groove is 4 mm. 91

5.21 Dip coating scenario of a probe with a groove. On the right hand side, the angles between the interface and the vertical red line are given. 93

5.22 The rise height (left) and the contact angle (right) plotted over the height along a vertical line at the wall (indicated by the red line in Fig. 5.21) while overcoming the groove. The angle between the vertical line at x_{fw} as derived in the previous chapter indicated by the red line and the numerical results with a resolved groove and a modeled groove accounted for by the contact angle boundary condition. Similarly the rise heights are compared. 94
5.23 Comparison of the interfaces for the resolved and modeled domain in the different regions and at the kinks. Differences in region 4 (f) and 5 (h) as well as at kink 4 (g) are associated to the dynamics involved due to the sudden change of the contact angle in the resolved domain. 96
5.24 97
5.25 The evolution of the rise height (left) and th contact angle (right) while overcoming a valley of a pyramid. The numerical results of the resolved valley correspond to the analytical prediction. Additionally, the results of the modeled case agree nicely to the analytic and resolved cases. . 98
5.26 The evolution of the rise height (left) and the contact angle (right) of a sequence of valleys. In red, the analytical estimate as described in Sec. 5.6.3 and the squares are the numerical results from a resolved geometry at the vertical line along the peaks. 99
5.27 The evolution of the rise height and the contact angle in the two and three dimensional setups. 100

A.1 The rise height h of a fluid on a flat wall for a given contact angle θ_s. 108
A.2 The rise height of the contact line for a given contact angle compared on a hexaedral and polyhedral mesh on different mesh resolutions. The theoretical rise height calculated by Eq. (A.1) is drawn with a dashed line. 109

List of Tables

3.1 Experimental setup taken from [73]. 44
3.2 Overview of the numerical setup and the theoretical critical inclination angle given by Eq. (3.1). 49

4.1 Hysteresis values of the different substrates. 58
4.2 Critical inflow velocities in the experiments and simulations. 61

5.1 Dimensions of the pyramids corresponding to the definitions of Fig. 5.2(b) 68
5.2 Fluid parameters 68

A.1 Numerical parameters for the case of the calculation of the rise height on different meshes. 108